APPLICATION OF THE FUNDAMENTALS OF HEAT AND MASS TRANSFER TO THE INVESTIGATION OF WAX DEPOSITION IN SUBSEA PIPELINES

by

Zhenyu Huang

A dissertation submitted in partial fulfillment
of the requirements for the degree of
Doctor of Philosophy
(Chemical Engineering)
in the University of Michigan
2011

Doctoral Committee:

Professor H. Scott Fogler, Chair
Professor Robert M. Ziff
Professor Massoud Kaviany
Assistant Professor Charles W. Monroe

2011

Dedication

This dissertation is dedicated to my parents, Zhike Zhang and Yaopei Huang as well as my wife, Wenyan Ji for their unconditional love and support.

本博士论文特此献给我的父母黄耀培，张志科，我的妻子纪文燕。若是没有他们无时无刻无条件的关爱，就不可能有这篇博士论文的诞生。

Acknowledgements

As the English poet John Donne says, no man is in island. The completion of my doctoral study would not have been possible without the sacrifice, help and guidance from numerous individuals, to many of whom my gratitude cannot be commensurate by the mere several pages of this acknowledgement. As one of the limited people who will read this thesis over and over again, I believe that documenting their names reminds me how much love I have been given by the community and I should always contribute my love and dedication in return.

My first acknowledgement goes to Professor Fogler as my doctoral advisor. He has given me the essentials of what a graduate student should be. He taught me that original research is not possible without critical thinking, that if I do not want my grand-children to pick up my degree I must combine fundamental research with approaches of practicality, that scholarly writing comes from hard work and that being proactive is the prerequisite for excellence. Professor Fogler is very nice to work with. I have the luxury to enjoy myself in a great magnitude freedom to develop my research projects while he consistently provides critical and insightful suggestions and concerns. In my last year of doctoral study, he encouraged me to shoulder a lot of group responsibilities. He gave me the opportunities to not only look at my own research projects but also that of the others in the group and to see how we can better utilize our resources in developing these projects. He has given me his trust in my inputs over a variety of issues including funding

options and future directions for research. Ademas, tengo que acentual que su talentos en las lenguas multiples han siempre sido un gran inspiracion para mis aprendizaje de espanol. Escribo este parrafo para expresar mi gratitud.

I am very thankful to Professors Massoud Kaviany, Charles Monroe and Robert Ziff as the members of my theses committee for their guidance and support. They have provided inputs that are very helpful not only for my research, but also for how the fruit of my research can be better presented. Professor Ziff was the Professor who interviewed me when I was applying for the University of Michigan for graduate school and I am very thankful that I was eventually given this opportunity. Professor Monroe's love in the details of the equations reminds me that slightly different mathematical approaches can represent drastically different physics and I should always have thorough understandings about the mathematical description that I am apply in my model.

I would like to thank Professors Omolola Eniola-Adefeso, Mark Burns, Joerg Lahann and again Scott Fogler for the opportunities that they have given me to serve the department as a graduate student instructor. Throughout my second years of teaching I have not only further consolidate my understandings of the fundamentals of chemical engineering, but I also have learned how to efficiently and scholarly express the knowledge that I have processed to others and always think in terms of their perspectives.

The department staff has been very friendly and supportive for my doctoral studies. Laura Bracken has been "the indispensible secretary" (quote from Professor Fogler) in minimizing the enormous amount of paper works for stationery supplies, expense reimbursements and many others. In addition, Susan Hamlin, Claire O'Connor, Leslie

Cypert, Shelley Fellers, Jane Wiesner, Linda Casto, Pamela Bogdanski and Christine Moellering have been very helpful in handling my countless requests.

The Fogler research group has provided me an atmosphere of excellence throughout my graduate study where everyone is expected to understand each other's research and to provide critical reviews and suggestions. Therefore, I am able to probe into a variety of subjects for petroleum related research including asphaltene precipitation/deposition acidization and scale deposition. Many previous students have provided me significant support during my graduate school. Tabish Maqbool has taught me the importance of taking the responsibilities and the leadership of the group as I was becoming the senior student. Michael Senra has been not only a helpful senior student, but also the indispensible mentor in language, writing, teaching and research. Had it not been his impact on me I would not have completed graduate school in a timely manner. The current graduate students have continued this tradition of excellence: Michael Hopefner has always applies high academic standards on his research and helps provide insightful reviews and suggestions to other group members. Nasim Balou is one of the most intelligent graduate students I have ever met. Oluwasegun Adegoke and Yingda Lu, the two junior students on wax deposition have gradually started to pick up the baton to become future leaders of the research group. Ravi Kapoor and Sheng Zheng are the two undergraduate students that worked under my guidance in the development of several CFD projects and I am impressed by their intelligence, work ethics and proactivity. Other students, including Liz Gorrepati, Shanpeng Han, Arjames Balgoa, Pattanapong Wongthahan, Dr. Sasanka Raha, Ekarit Paracharoensawad, Perapat Srikiratiwong and Satinee Yindee.

I would like to acknowledge the financial support from the affiliates companies of my research program. For the past 5 years I have benefited greatly from the discussions within the world leading flow assurance research scientists from the affiliates companies. Among those are Probjot Singh, Rama Venkatesan and Hyun Su Lee, who had been outstanding PhD students in our group and still remain as role models for our graduate students. In addition, I would like to acknowledge Rainer Hoffmann and Lene Amundsen from Statoil ASA. for giving me the opportunity to carry out one of the most expensive multiphase wax deposition experiments that could not have been done elsewhere. Rainer is one of the most down-to-earth research scientists I have seen and I greatly appreciate his critical thinking in our collaborations.

As an international student, being not fluent in English and not familiar with the American culture has frequently led me to awkward responses and the inability to participate in conversations of native speakers when I started my graduate school in Ann Arbor. I am very grateful that I have found a group of friends in Ann Arbor that have been very patient and instructive in our conversations and have encouraged my participation in a variety of their activities. These friends include Professor and Mrs Fogler, David and Nikki Ingram, Jim and Amy Bucher, Tom Westrich and Meghan Cuddihy, Liz and Bean Getsoian, Joe and Megan Mayne, Daniel and Michelle Lilly, Phillip Christopher and Ramsey Zeitoun, Neil Schweitzer and Amanda Hickman, Siris Laursen, Sean Langelier, Liz Stewart, Ines Pons, Nick Stuckert and other countless names. They have provided great influence on my learning of the English language and the American culture.

The Chinese community has given me significant support during my doctoral study. I have shared my perspectives on the economic and social developments in China with many of my Chinese friends in Michigan including not only my college classmates who have spent the same 5 years in various graduate schools in the United States: Huang Wu (and his wife Wenzhao Yang), Xingyu Gu, Dichuan Li, but also countless friends in Ann Arbor: Weixian Shi, Fang Wang, Xue Chen, Yu Chen, Hongliang Xin, Shi Yu, Jing Liu, Yingda Lu, Sheng Zheng and Yuan Chen, Jianwen Zhang, QingQing Guan, Shao Sun and many others. Same as our parents, we bear the mission to build a better the future of our motherland and we will go back to China to contribute our knowledge and experience whenever we are needed.

My thesis cannot be made possible had it not been the support from numerous family members. I am very grateful to Auntie Carol for the care and love that she has given me since I was a baby. Her two children Sara and Harry are virtually my little brother and sister and they are part of the reason of what I am today. In addition, the five years in Ann Arbor would have been quite different had it not been shared with Hao Yu. He is like my little brother as he always looks up to me and shares with me his experiences and thoughts. My cousin Rachal Huo Jingling has been the “indispensible” cousin who is always there to listen to my thoughts and share hers with me.

My parents-in-law could not have been more supportive to my marriage with my wife, Grace Wenyan Ji as they have set a perfect example for Grace and me as a devoted couple. My father has constantly given me the unconditional love and care and he believes that I am the most significant achievement in his career. My mother has been the most important inspiration for my life. Despite the countless ordeals she met in her life

she has never let any of those to have any negative impact on me. It is the encouragement and comfort that we give to each other that help us go through the adversities and we have become the most important part of each other's lives. As a typical Chinese "tiger mum", she used most of her salary for my afterschool classes and sports practices while she lived an almost frugal life for herself. She taught me to always apply high standards on myself and be tolerant on others, to be constantly aware of my own shortcomings and take initiatives to overcome them. It is her persistent dedication to my education that has shaped what I am today as a person and I cannot imagine what my life would be had she not been my mother:

父母亲爱心，柔善像碧月，常在心里面何日报。

亲恩应该报，应该识取孝道，唯独我离别，无法慰亲旁，轻弹曲韵梦中送。

I feel very fortunate that I met my wife Grace, who shares a lot of similarities to my mother. Her unconditional commitment to our marriage and the support to me and my family without any hesitation are the foundations for this thesis. She has also become my soul mate as she is never afraid to challenge my perspectives. She has been my love and my best friend as she will always be.

Table of Contents

List of Figures

List of Tables

List of Symbols

Geometry

d: diameter, m
H: the height of the phase (oil or water) in stratified channel flow, m
W: the width of the channel,m
L: length of the pipe, m
r: radial coordinates (cylindrical coordinates), m
r_d effective radius of the pipe due to deposition, m
r_i: radius of the inner pipe, m
x: horizontal coordinates (rectangular coordinates), m
y: vertical coordinates (rectangular coordinates), m
z: axial (cylindrical coordinates) coordinates or radius, m

Transport and Thermal Dynamic Properties

A: area, m^2
C: concentration of wax in oil, kg/m^3
C_1,C_2: coefficients for the eddy diffusivity given by Vandriest[25], C_1 = and C_2 =
C_p: specific heat, J/kg/K
D_{wo}: diffusivity of wax in oil, m^2/s
E: activation Energy for the viscosity equation, J/mol
F_w: wax fraction of the deposit
F: weight fraction of solid phase or liquid phase in crude oil or in cakes
G: growth rate of precipitated wax particles, $kg/m^3/s$
K: ratio of weight percent of light components in the cake to that in the crude oil, obtained using normalized carbon number distribution
N_C: lowest carbon number of precipitated wax
N_p: number density of the precipitated particles, m^{-3}
Q: flow rate, m^3/s
R: ideal gas constant, 8.314 J/K/mol
T: temperature, °C or K
U: averaged velocity, m/s
V: velocity, m/s
V_m: molecular volume of wax, cm^3/mol

a: ratio of weight percent of light components in the cake to that in the crude oil
b: ratio of mass of centrifuged cake to the mass of crude oil sample
h: heat transfer coefficient, $W/m^2/K$
k: thermal conductivity, W/m/K

k_r: precipitation rate constant of wax in oil, s^{-1}
k_d: mass transfer coefficient from bulk to the individual nucleus, m/s
m: mass, g
t: time, s
w: weight fraction
y^+: dimensionless distance from the wall

κ: coefficient for the eddy diffusivity given by Vandriest[25]
μ: viscosity, Pa·s
ρ: density, m^3/kg
δ: deposit thickness, mm
α: thermal diffusivity, m^2/s
ε: eddy diffusivity (momentum, heat or mass), m^2/s
ν: kinematic viscosity, m^2/s
λ: de-dimensionalized axial coordinate
η: de-dimensionalized radial coordinate

Dimensionless numbers

Re: the Reynolds number
Nu: the Nusselt Number
Pr: the Prandtl number
Sc: the Schmidt number
Sh: the Sherwood number
Gz: the Graetz number

Abbreviations

cloud: properties at the cloud point
eq: properties at thermodynamic equilibrium
interface: properties at the oil-deposit interface
bulk: properties of the bulk
heat: properties about heat transfer
momentum: properties about momentum transfer
mass: properties about mass transfer
eff: effective diffusivity of wax in the deposit
T: properties in turbulent flow conditions
coolant: properties of the coolant
inlet: properties at the inlet
wall: properties at the wall
deposit: properties of the deposit
p: properties of the precipitated wax particles
rmsd: root mean square deviation
measured: measured value
normalized: normalized value
crude: crude oil
cake: centrifuged cake

oil: properties of the oil
water: properties of the bulk water
L: liquid phase
S: solid phase

Chapter 1

Introduction

1.A Overview of Wax Deposition

The transportation of oil from the reservoir to the processing facilities has been a vital part in the production of the petroleum industry. As the on-shore reservoirs become depleted over time, the focus of production has shifted towards off-shore reservoirs, which have imposed a variety of flow assurance issues related to the transportation of the crude oil. Among those issues, wax deposition in the subsea oil pipelines has become of the most significant economic problem for petroleum production.[1-7]

At typical reservoir temperatures (70ºC – 150ºC) and pressures (>2000 psi), wax molecules are dissolved in the crude oil. As the crude oil flows through a subsea pipeline resting on the ocean floor at 4C, the temperature of oil decreases below its cloud-point temperature (or wax appearance temperature, WAT) because of the heat loss to the surroundings. The waxes in the oil form deposits on the cold pipe wall, which has become a major problem for flow assurance. The deposit can even grow to a point where the pipeline becomes plugged, causing production to be stopped in order to replace the plugged portion of the pipeline. In one case, the wax deposition was so severe and frequent that an off-shore platform in the North Sea had to be abandoned at a cost of

about $100,000,000.[8] The development and application of the remediation techniques for wax deposition have become a vital part of the flow assurance practice and research.

Remediation techniques for wax deposition have become a vital part in flow assurance research. Significant production cost can be attributed to these techniques include pigging, pipeline insulation, heating and fused chemical reactions. One of the most conventional mechanical remediation methods used is pigging where an inspection gauge or a ‘‘pig’’ is sent in the pipeline to scrape off the wax. Using pigging as an example, insufficient pigging frequency can result in a deposit that grows so thick that the pig has been known to get stuck, which stops the flow of petroleum fluids. However, too high of a pigging frequency can lead to additional costs of tens of millions of dollars due to deferred production.[9] Another technique takes the advantage of fused chemical reactions that uses an exothermic reaction with controlled heat emission.[10] Under these circumstances, predictive modeling of wax deposition has become an indispensable approach, not only to understand the fundamental physics of wax deposition during crude oil transportation in pipelines but also to design effective remediation strategies.

1.B A review of wax deposition modeling

Three major aspects are involved in wax deposition modeling: hydrodynamics, heat/mass transfer and deposition mechanism. Due to the fact that water and gas frequently accompany oil in subsea pipelines, wax deposition must eventually be analyzed in multiphase flow conditions.[11] However, most of the existing wax deposition studies are limited in the scope of single-phase flow, where reliable correlations on hydrodynamics and heat/mass transfer are well developed.[12,13] As early as the 1990’s, various mechanisms for wax deposition were proposed including molecular diffusion,

shear dispersion, and Brownian diffusion. Among these mechanisms, molecular diffusion has been shown to be the dominant process in wax deposition and can be summarized in the following four major steps.[14]

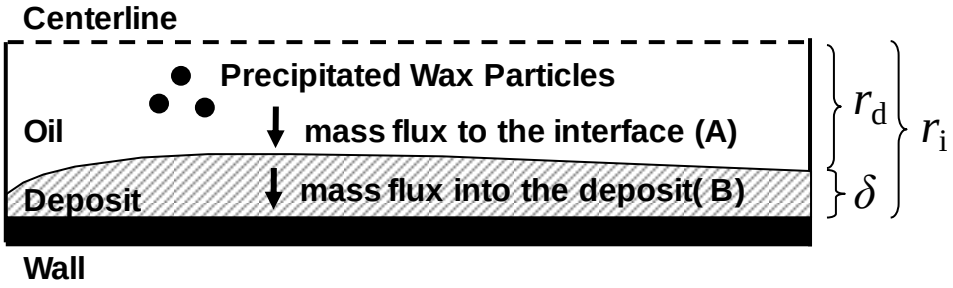

Figure 1-1 A sketch of molecular diffusion as the mechanism for wax deposition

(1) Formation of an incipient deposit layer on the cold pipe wall surface.

(2) Radial mass flux of paraffin molecules from the bulk fluid toward the oil-deposit interface (shown as A).

(3) Radial flux of paraffin molecules from the interface into the deposit layer (B). The difference between the mass flux from the bulk to the oil-deposit interface (A) and the mass flux from the interface into the deposit (B) represents the growth rate of the deposit thickness.

(4) Precipitation of paraffin molecules inside the deposit, which leads to the increase of solid wax fraction of the deposit.

A number of mathematical models have used molecular diffusion to predict wax deposition in oil pipelines. Early models attempted to predict the growth of the deposit thickness using the radial mass flux of the wax molecules from the bulk oil to the oil-deposit interface (flux A).1[-7,11] Unfortunately, these early models have not considered the diffusion from the interface into the deposit (flux B). Therefore, they have to assume the

wax content inside the gel to be constant (no internal concentration gradient within the deposit). However, it is now known that the wax content in the deposit not only varies in the radial direction within the deposit, it also increases as the deposit thickens.[1415] This increase in wax content over time is called aging and causes an increase in the thermal conductivity of the deposit layer and a decrease in the molecular diffusivity of wax in the deposit. These issues were not accounted for in the models referenced above.

Singh and Fogler developed the first model to successfully study the effects of aging in wax deposition, which precisely predicted not only the growth of thickness but also the increase of wax fraction in the deposit.[14] The wax fraction is an indicator of gel strength, an important parameter for designing remediation methods such as pigging. However, the heat and mass transfer correlations used in this model can over-predict the deposition rate for turbulent flow conditions because they assume that the temperature and concentration fields are independent, a situation only valid in laminar flow. This laminar flow model correctly neglects the precipitation of wax molecules in the oil phase. However, wax precipitation in the oil is an important issue in turbulent flow where the cooling rate of the oil is relatively slow.

A refinement of this model used the ‘‘solubility method’’ in the boundary layer, which assumed that precipitation depends solely on the solubility of wax in the oil.[17] However, this solubility approach can under predict the thickness of the deposit because it does not account for the supersaturated wax molecules that do not have sufficient time to precipitate during their residence in the pipe. The solubility approach represents a lower bound on the deposit thickness, whereas the use of independent heat and mass transfer correlations represents the upper bound of wax buildup. The approach developed

by Lee[16] accounted for the precipitation kinetics in the boundary layer, leading to predictions between those by Singh's method of independent heat and mass transfer (reference) and Venkatesan's solubility method.[17,18]

1.C Research Objectives and Thesis Overview

The research in these study focuses on the development of a rigorous understanding of wax deposition using the fundamentals of heat and mass transfer theories, as illustrated in the subsequent chapters. Chapter 2 includes the verification of a deposition model that accounts for the kinetics of wax precipitation in the oil to various deposition experiments. Chapter 3 highlights the importance of the solubility curve as the most influential input to wax deposition modeling and describes how the accuracy from a previous method to measure the solubility curve can be improved by accounting for the appropriate mass balances. Chapter 4 focuses on the application of the deposition model to a variety of experiments using a real crude oil at various operating conditions. The impacts of the operating conditions on wax deposition will be studied. Chapters 5 and 6 is devoted to the study of wax deposition in oil/water multiphase flow where the oil/water stratified flow is focused as one of the most frequent conditions where significant wax deposition can occur. In these two chapters a 2D deposition model is first introduced to demonstrate the effect of the presence of water on wax deposition. Furthermore, wax deposition experiments of the flow-loop are highlighted, which reveals gelation as a different deposition mechanism in comparison to diffusion at low oil flow rates.

Chapter 2

Numerical Heat and Mass Transfer Analysis of Wax Deposition under Pipe-Flow Conditions

2.A Introduction

Remediation techniques for wax deposition have become a vital part in the flow assurance research. One of the most conventional mechanical remediation methods used is pigging where an inspection gauge is sent in the pipeline to scrape off the wax.[19] However, if the wax deposit builds up rather rapidly and hardens, the gauge can become stuck in the pipe, an event which occurred in a Gulf of Mexico pipeline.[20] Additionally, a fused chemical reaction technique that uses an exothermic reaction with controlled heat emission has been proposed to remove the wax deposit.[21,22] In order to successfully exploit those aforementioned techniques, it is crucial to know the deposit thickness profile and the wax fraction of the deposit. Therefore, wax deposition modeling is of crucial importance to establish fundamental understanding of the issue and help design effective remediation techniques.

In this research, we have investigated the coupling of heat and mass transfer phenomenon under turbulent flow conditions using the finite difference method (FDM) in wax deposition modeling. The impact of the precipitation of wax molecules in the oil is discussed. In addition, by comparing the results of the model with both lab-scale and

pilot-scale wax deposition experiments, we will show that the wax deposition model can successfully predict both the growth of the deposit thickness and the aging of the deposit in various flow conditions. Finally, model is used to study wax deposition in field-scale pipeline systems.

2.B Model Development

A novel model called the Michigan Wax Predictor (MWP) was developed in this research. The model first evaluates the transport characteristics in a pipe flow system then applies molecular diffusion as the deposition mechanism for wax deposition prediction, which will be discussed in the subsequent sections.

2.C Heat and Mass Transfer

We will introduce the two conventional approaches before we elaborate the kinetic method in this study: the Independent Heat and Mass Transfer method[14] (IHMT) and the Solubility method. [18]

2.C.1 Independent Heat and Mass Transfer Method (IHMT) as the Upper Bound:

This approach is first used by Singh and Fogler for wax deposition modeling in laminar flow, where the transport correlation by Seider and Tate is used as shown in Equation (2.1).[13]

$$\begin{cases} \mathrm{Nu} = 1.24\left(\dfrac{d}{L}\mathrm{Re}\,\mathrm{Pr}\right)^{(1/3)} \\ \mathrm{Sh} = 1.24\left(\dfrac{d}{L}\mathrm{Re}\,\mathrm{Sc}\right)^{(1/3)} \end{cases} \tag{2.1}$$

In the above correlations, heat and mass transfer are independent from each other. This approach is valid only when the precipitation of wax molecules in the oil phase is negligible. However, work has shown that this assumption is invalid in turbulent flow where there is significant precipitation of wax molecules. This invalidity comes about because when heat and mass transfer are independent of one another, mass transfer is independent of temperature. However, if bulk precipitation, a process that is dependent on temperature, occurs, then mass transfer will be affected by the precipitating molecules. Therefore, bulk phase precipitation would not be accounted for if the heat and mass transfer effects are decoupled. As a result, the amount of wax molecules dissolved in the oil available for wax deposition is over-estimated in the IHMT model, which leads to the over-prediction of the growth of deposit thickness and represents the upper bound in the model.

2.C.2 Solubility Method as the Lower Bound

In order to account for the precipitation of wax molecules in the oil phase, Venkatesan and Fogler proposed a lower bound called the "Solubility method".[18] This method calculates the radial mass transfer rate from the bulk oil to the oil-deposit interface assuming a dependency between heat and mass transfer.[17] In their study, the Dittus-Boelter heat transfer correlation is used for turbulent flow[23], while the mass transfer is dependent on heat transfer based on the solubility of wax, $C_{\mathrm{ws}}(T)$, as shown in Equation (2.2).

$$\begin{cases} \mathrm{Nu} = 0.023\,\mathrm{Re}^{0.83}\,\mathrm{Pr}^{0.33} \\ \mathrm{Sh} = \mathrm{Nu}\left(\dfrac{dC(\mathrm{eq})}{dT}\right)\Big|_{\mathrm{interrface}} \dfrac{T_{\mathrm{bulk}} - T_{\mathrm{interface}}}{C_{\mathrm{bulk}}(\mathrm{eq}) - C_{\mathrm{interface}}(\mathrm{eq})} \end{cases} \tag{2.2}$$

The solubility method used to calculate the radial mass transfer (i.e. the Sherwood number) assumes that the concentration of wax in the oil follows thermodynamic equilibrium with the precipitated solid wax particles. This assumption indicates that all supersaturated wax molecule will precipitate instantaneously in the oil. However, not all of the supersaturated wax molecules have sufficient time to precipitate during their residence in the pipe (flow-loop experiments can have residence times on the order of seconds) and some of them can be transported to the oil-deposit interface for deposition. Therefore, this lower-bound model tends to under-estimate the radial transport of wax molecules and hence under-predicts the growth of wax deposit thickness.

A comparison of the concentration profiles of wax in the oil using these two aforementioned methods is shown in Figure 2-1. It can be seen that in reality, the concentration profile in the oil phase can be bounded by the IHMT model as the upper end and the solubility model as the lower end, depending on the kinetics of precipitation.

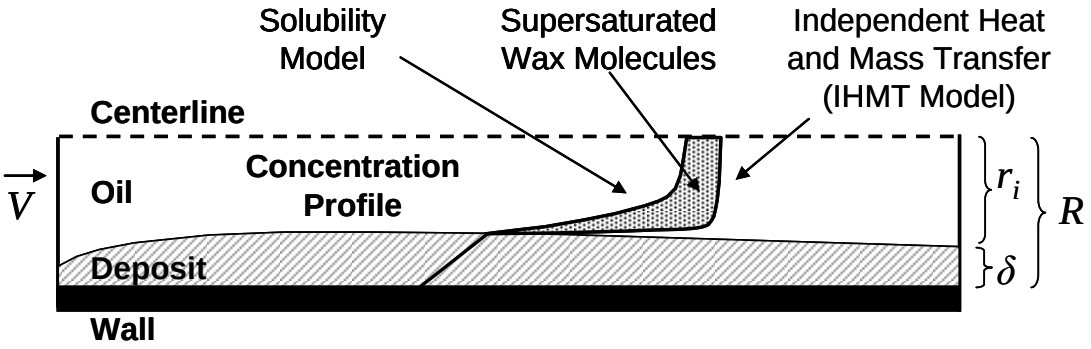

Figure 2-1: A comparison of the radial concentration profiles of wax between the IHMT model[14] and the Solubility model.[18]

2.C.3 Kinetic Method

In order to quantify the effect of precipitation kinetics on wax deposition in this study, a deposition model (the MWP) is developed using numerical methods to solve transport

equations instead of using empirical correlations. The MWP first evaluates the heat and mass transfer by solving the following equations.

(Heat Transfer)

$$V_z \frac{\partial T}{\partial z} = \frac{1}{r}\frac{\partial}{\partial r}\left[r\left(\varepsilon_{\text{heat}} + \alpha\right)\frac{\partial T}{\partial r}\right] \tag{2.3}$$

(Mass Transfer)

$$V_z \frac{\partial C}{\partial z} = \frac{1}{r}\frac{\partial}{\partial r}\left[r\left(\varepsilon_{\text{mass}} + D_{\text{wo}}\right)\frac{\partial C}{\partial r}\right] - k_r\left(C - C(\text{eq})\right) \tag{2.4}$$

where for laminar flow, $\varepsilon_{\text{heat}} = \varepsilon_{\text{mass}} = 0$. For turbulent flow, the correlations for the momentum thermal and mass diffusivities are used, as shown in Equations (2.5).[24]

$$\frac{\varepsilon_{\text{heat}}}{\alpha} \equiv \frac{\text{Pr}}{\text{Pr}_T}\frac{\varepsilon_{\text{momentum}}}{\nu} \quad , \quad \frac{\varepsilon_{\text{mass}}}{D_{\text{wo}}} \equiv \frac{\text{Sc}}{\text{Sc}_T}\frac{\varepsilon_{\text{momentum}}}{\nu} \tag{2.5}$$

The eddy momentum diffusivity ε is obtained by the correlation of Van Driest, as shown in Equation (2.6).[25]

$$\frac{\varepsilon_{\text{momentum}}}{\nu} = \left(C_1 y^+\right)^2 \left(1 - e^{-y^+/C_2}\right)^2 \left|\frac{dV_z^+}{dy^+}\right| \tag{2.6}$$

The velocity profile from turbulent flow is given by the von Kármán correlation, as given by Equation [26]

It should be noted that the von Kármán correlation for the velocity profile is based on isothermal flow conditions, for non-isothermal flows the change in the viscosity might results in discrepancy in the velocity profile. This discrepancy is not as significant in field operating conditions where the insulation of the pipelines help to prevent drastic changes in the temperature in both radial and axial direction ($h_{\text{external}} / h_{\text{internal}} \sim 10^{-4}$). For lab-scale

deposition experiments the external heat transfer coefficient is greatly elevated by removing the pipe-insulations and applying a coolant though the annulus of the pipe to establish forced convection. To investigate the impact of the change in the viscosity in non-isothermal conditions, a CFD simulation based on the geometry of a 5-m lab-scale flow loop has been carried out where the changes in the viscosity in the radial and axial directions are accounted for. The detail of the CFD simulation can be seen in Chapter 7.B and the viscosity of the oil can be seen in Figure 4-3. It was found that the velocity profile showed a negligible difference (<5%) between the CFD calculations and that from the von Kármán correlation. This small difference is due to the fact that most of the deposition experiments in this Chapter are carried out in a temperature range high enough for the oils to remain as Newtonian fluids and the decrease in the temperature is not sufficient to trigger significant increase in the viscosity.

In the heat transfer equation shown in Equation (2.3), the heat of crystallization has been neglected based on the study of Singh, et al.[14] In addition, the Brinkman number $\mathrm{Br} = \frac{\mu U^2}{k\left(T_{\text{inlet}} - T_{\text{wall}}\right)}$ is around 10^{-4} in this study, indicating that the viscous heating can be neglected as well.

The boundary conditions for Equations (2.3) and (2.4) are shown in Equations (2.7) and (2.8):

$$\begin{cases} T = T_{\text{inlet}},\ at\ z = 0 \\ \dfrac{\partial T}{\partial r} = 0,\ at\ r = 0 \\ h_{\text{coolant}}\left(T_{\text{coolant}} - T_{\text{wall}}\right) = k_{\text{deposit}}\dfrac{\partial T}{\partial r},\ at\ r = R \end{cases} \tag{2.7}$$

$$\begin{cases} C = C_{\text{inlet}}\left(\text{eq}\right),\ at\ z = 0 \\ \dfrac{\partial C}{\partial r} = 0,\ at\ r = 0 \\ C = C\left(\text{eq}\right),\ at\ r_{\text{d}} \le r \le r_{\text{i}} \end{cases} \tag{2.8}$$

The thermal boundary condition assumes continuous heat flux at the wall with constant external heat transfer coefficient, h_{coolant}, which accounts for the thermal resistance of the insulation material and the coolant. The boundary condition for mass transfer assumes that the wax concentration follows liquid/solid equilibrium in the deposit. The above equations are solved by a backward implicit scheme.[27]

2.C.4 The Precipitation Rate Constant

It should be noted that if there is no precipitation of wax molecules in the oil ($k_{\text{r}} = 0$), the heat and mass transfer equations (Equations (2.3) and (2.4)) are not related and the model reduces to the upper bound of independent heat and mass transfer (IHMT). As k_{r} increases, the wax concentration approaches to the thermodynamic equilibrium concentration, $C_{\text{ws}}\left(T\right)$, which is the lower bound Solubility model.

The specific precipitation rate parameter k_{r} (or equivalently the growth rate of wax nucleus in supersaturated solution) is zero if the temperature of oil is greater than the wax appearance temperature. When the oil temperature is lower than the wax appearance temperature, we can estimate the growth rate of precipitated wax particles, G (kg/m^3/s), assuming that diffusion is the rate determining step for particle growth by Equation (2.9):[28]

$$G = \underbrace{k_{\text{d}} A_{\text{p}} N_{\text{p}}}_{k_{\text{r}}}\left(C - C\left(\text{eq}\right)\right) \tag{2.9}$$

where k_d is the mass transfer coefficient from the bulk to the individual nucleus surface, A_p is the surface area of a nucleus and ρ_n is the number density of the nuclei. The mass transfer coefficient k_d can be calculated from the Equations (2.10) and (2.11).[29,30]

$$k_d = \frac{\mathrm{Sh}_p D_{wo}}{d_p} \tag{2.10}$$

$$\mathrm{Sh}_p = 2 + 0.6\,\mathrm{Re}_p^{0.5}\,\mathrm{Sc}_p^{1/3} \cong 2 \tag{2.11}$$

Combining Equations (2.9), (2.10) and (2.11) it is seen that the specific precipitation rate parameter k_r is a function of temperature because of the dependency of diffusivity on temperature, as shown in Equation (2.12).

$$k_r = \frac{\mathrm{Sh}_p A_p N_p}{d_p} D_{wo}(T) \tag{2.12}$$

The correlation for diffusivity given by Hayduk and Minhas[31] and the Arrhenius Equation for the viscosity is used to express k_r as a function of temperature:

$$D_{wo} = 13.3\times10^{-12} \times \frac{T^{1.47}\mu^{\gamma}}{V_M^{0.71}},\ \gamma = \frac{10.2}{V_M} - 0.791 \tag{2.13}$$

$$\mu = \mu_{cloud} \exp\left[\frac{E}{R}\left(\frac{1}{T} - \frac{1}{T_{cloud}}\right)\right] \tag{2.14}$$

Putting Equations (2.13) and (2.14) into Equation (2.12) and taking a ratio between k_r at any temperature and k_r at the cloud point gives Equation (2.15).

$$\frac{k_r}{k_{r,\,cloud}} = \left(\frac{T}{T_{cloud}}\right)^{1.47} \exp\left[\frac{\gamma E}{R}\left(\frac{1}{T} - \frac{1}{T_{cloud}}\right)\right] \tag{2.15}$$

where the precipitation rate parameter at the cloud point temperature, $k_{\text{r, cloud}}$, is the only adjustable parameter in this model. Although the parameter is adjustable, its value is found to be bounded in a range estimated from first principles. We used the $k_{\text{r, cloud}}$ in this study to back calculate the range of the number density, ρ_{n} in Equation (2.12). The result falls between full precipitation based on equilibrium assumption (maximum number density with critical nucleus size) as the upper bound and microscopic observation in the deposit (minimum number density with fully grown wax crystals) as the lower bound. The details of this calculation are given by Lee.[16]

2.D Deposition Mechanism

Because molecular diffusion is the deposition mechanism, the diffusive mass flux into the deposit contributes to the increase of the wax fraction in the deposit as shown in Equation (2.16).[14]

$$\pi\rho_{\text{gel}}\left(R^2 - r_i^2\right)\frac{d\bar{F}_{\text{w}}}{dt} = -2\pi r_i\left(-D_{\text{eff}}\left.\frac{dC}{dr}\right|_{\text{from interface to deposit}}\right) \tag{2.16}$$

The difference between the mass flux from the bulk oil to the oil-deposit interface and the mass flux from the interface to the deposit corresponds to the growth of the deposit thickness, as shown in Equation (2.17).[14]

$$2\pi r_i\rho_{\text{gel}}\bar{F}_{\text{w}}\frac{d\delta}{dt} = 2\pi r_i\left(-D_{\text{wo}}\left.\frac{dC}{dr}\right|_{\text{from oil to interface}}\right) - 2\pi r_i\left(-D_{\text{eff}}\left.\frac{dC}{dr}\right|_{\text{from interface to deposit}}\right) \tag{2.1}$$

where D_{wo} is the diffusivity of wax in oil calculated by the correlation of Hayduk and Minhas,[31] D_{wo} is the effective diffusivity of wax in the deposit calculated by the correlation of Cussler et al.[32]

2.E Results and Discussion

Before we substantiate the application of the computational wax deposition model in field scale pipelines, the accuracy of the theoretical model is first verified in lab-scale laminar flow experiments[14] and also in pilot-scale turbulent flow-loop experiments.[33] The oil properties and the operating conditions of these two experiments are summarized in Table 2-1.

Table 2-1 Summary of the oil properties and operating conditions in the lab-scale and the pilot-scale experiments

	Singh and Fogler[14]	Hernandez[33]
Cloud point, °C	13.9	34.4
Wax content wt%	0.67	3.55
Length of the pipe, m	2.44	50
Oil inlet temperature, °C	22.2	29.44
Coolant inlet temperature, °C	7.2	12.78
Oil flow rate, m3/s	6.3×10-5	3.31×10-3
Reynolds number	799	25138

.

2.F Lab-scale Laminar Flow-loop Experiments

A lab-scale flow-loop experimental result will be compared to the computational wax deposition model that includes precipitation kinetics.[14] A mixture of 3:1 volume ratio of mineral oil (Blandol) and Kerosene is blended with 0.67 wt% of food grade wax with carbon numbers ranging form C_{23}-C_{38}.

Figure 2-2 compares the deposit thickness measured in the experiment and that predicted by the MWP while

Figure 2-3 shows a comparison of the wax fractions at the end of the experiment. It is seen that the modely accurately predicts both the deposit thickness and wax fraction for the flow-loop experiment. The precipitation rate constant at the cloud point temperature, $k_{r,\,cloud}$, in this case was 0 s^{-1}, indicating that no wax molecules precipitated in the oil. . In this case, the model resembles the IHMT approach. This agreement explains the success of the model of Singh and Fogler, where independent heat and mass transfer correlations are used in laminar flow.

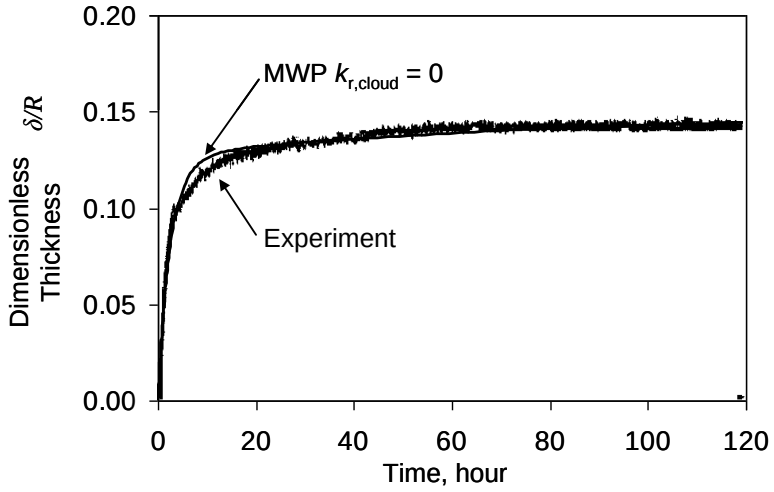

Figure 2-2 Comparison between experimental deposit thickness and prediction my MWP with $k_{r,\,cloud} = 0$ s^{-1} for the lab-scale laminar flow-loop.

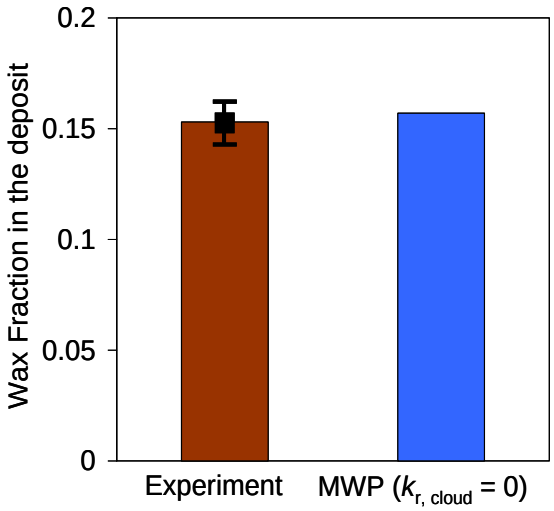

Figure 2-3 Comparison between the wax fraction from the sample after the deposition experiment and the prediction by the MWP for the lab-scale laminar flow-loop.

2.G Pilot-scale Flow-loop Experiments

Because large-scale flow-loop experiments provide the transition from lab scale experiments to field scale pipeline systems, we now apply the MWP to a pilot-scale turbulent flow-loop experiments by Hernandez.[33] Unlike the model wax-oil used in lab-scale tests discussed in the previous sections, a crude oil (Shell oil Company's Garden Banks Oil) is used in this case.

Similar to field scale pipelines, the bulk temperature of oil in the large-scale flow-loop changes with respect to the axial location. Figure 2-4 shows the comparison between the bulk temperature of oil measured as a function of axial distance at t=0 and that calculated by the MWP. The excellent match indicates a satisfactory evaluation of the heat transfer of the experiment, which is vital for predicting the growth of the deposit and the wax fraction in the wax deposit.

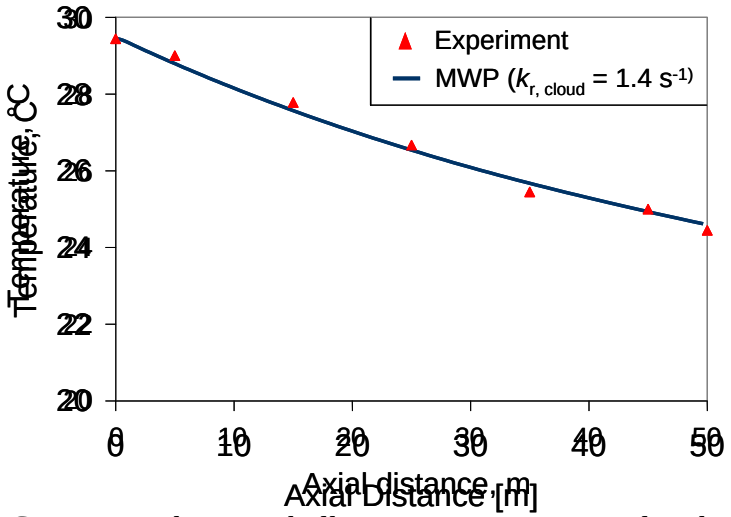

Figure 2-4 Comparison between bulk temperatures measured in the pipe and the prediction by MWP for the pilot-scale turbulent flow-loop at t=0 before deposition occurs.

Figure 2-5 compares the deposit thickness obtained by the MWP while Figure 2-6 shows comparison of the wax fractions at the end of the experiment. It is seen that the upper bound IHMT approach ($k_{r, cloud}$ = 0) over-predicts of the deposit thickness due to its over-estimate of the amount of wax molecules that is transported onto the wall for deposition. Meanwhile, under-prediction is observed for a high value of $k_{r, cloud}$ at $10^3 s^{-1}$, which approximates the lower bound solubility model. In this case, the supersaturated wax molecules are assumed to precipitate nearly instantaneously so that few of them are left for deposition. Excellent agreement between the model and the experiment for the deposit thickness and for the wax fraction can be seen when $k_{r, cloud}$ = 1.4 s^{-1}. This value will be used for further field-scale predictions.

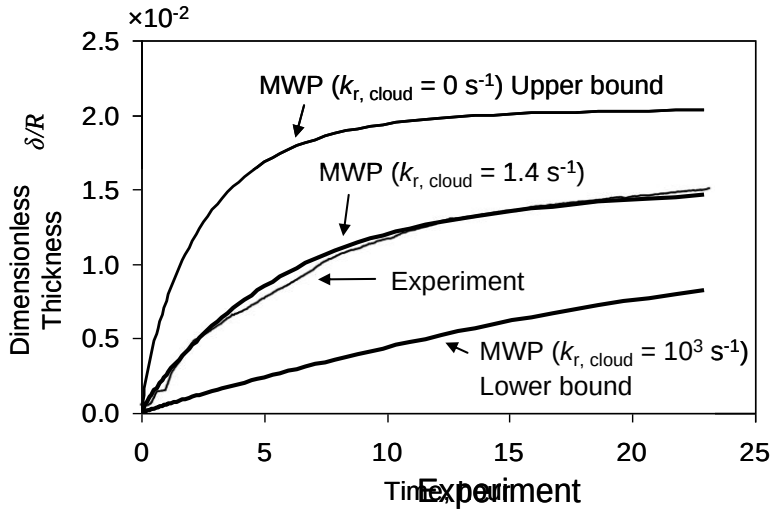

Figure 2-5 Comparison between experimental deposit thickness in the pipe and the predictions by MWP ($k_{r, cloud}$ = 0, 1.4 s^{-1} and 10^3 s^{-1}) for the pilot-scale turbulent flow-loop.

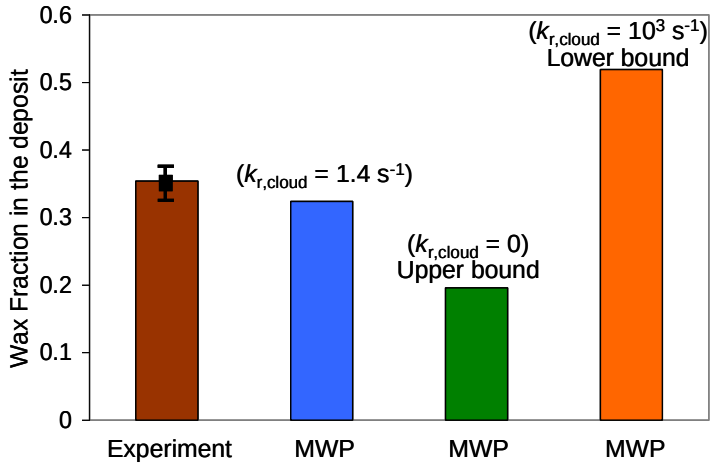

Figure 2-6 Comparison between the wax fraction from the sample after the deposition experiment and the predictions by the MWP ($k_{r, cloud}$ = 0, 1.4 s^{-1} and 10^3 s^{-1}) for the pilot-scale turbulent flow-loop.

2.H Field-scale Predictions

After verifying the MWP in both lab-scale and pilot-scale flow-loop experiments, the model is used to predict wax deposition in field-scale pipelines. In the previous flow-loop experiments, the radial thermal resistance was designed to be much smaller than for the field condition in order to minimize the experimental time, (i.e. several days at most).

However, in field conditions, the existence of insulating materials helps increase the thermal resistance and decrease the radial heat loss of the oil. Table 2-2 summarizes the input parameters for the calculation. For this section, the properties of the Garden Banks condensate[33] and the model oil[14] that were used to simulate field-scale wax deposition.

Table 2-2 Conditions for the base case of a field scale pipeline system

Operating parameters	Value
Inner Diameter of the pipe, (cm)	50
Length of the pipe, (km)	70
Flow Rate of oil, (bpd)	30,000
Flow Rate of oil, (m3/s)	5.52×10^{-2}
Inlet temperature of oil, °C	70
Ocean floor temperature, °C	4
External Heat Transfer Coefficient ($W/m^2/K$)	3

2.H.1 Predictions Using the Garden Banks Condensate as the base case

Figure 2-7 shows the axial profile of the predicted deposit thickness after 180 days using the Garden Banks condensate as the base case. It is seen that the deposit profile can be divided into three sections: (1) no deposition, (2) increasing deposition and (3) decreasing deposition. No deposit is found in the first section (0-33 km) where the inner wall temperature is higher than the cloud point temperature, shown in Figure 2-8. As the fluid enters the second section where the inner wall temperature drops below the cloud point (>33 km), wax molecules start to precipitate at the wall, causing wax deposition to occur. The driving force for deposition can be represented by the difference between the concentrations of wax molecules in the bulk and at the interface, ($C_{bulk} - C_{Interface}$), shown in Figure 2-9. It is seen that in the second section of the pipe (33-68 km), significant

precipitation of wax occurs near the wall due to a decrease in the wall temperature along the channel (Figure 2-8). This precipitation results in a decrease of $C_{interface}$, leading to the increase of ($C_{bulk} - C_{interface}$), the driving force for wax deposition. This increase in the driving force explains the increase in the deposit thickness along the channel during this section in Figure 2-7. As the fluid enters the third section, the precipitation of wax in the bulk becomes significant and thereby reduces C_{bulk}. This decrease in C_{bulk} reduces the driving force for wax deposition, causing the deposit thickness to decrease along the channel.

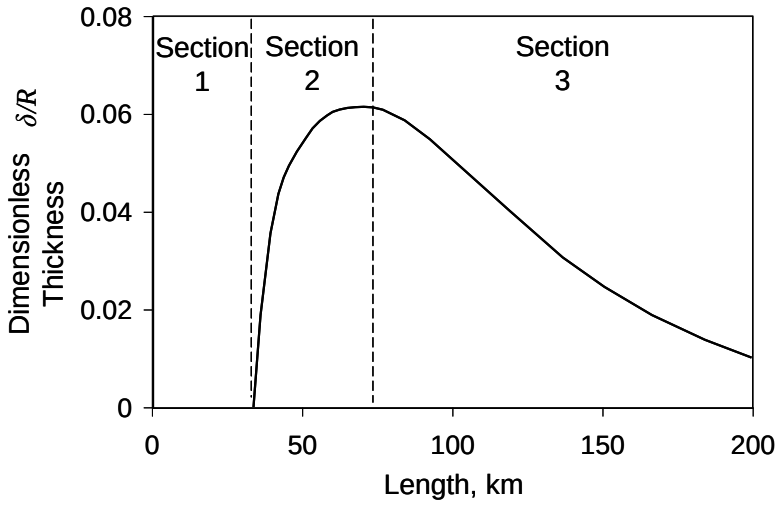

Figure 2-7: Deposit profile along the pipe for the base case after 180 days.

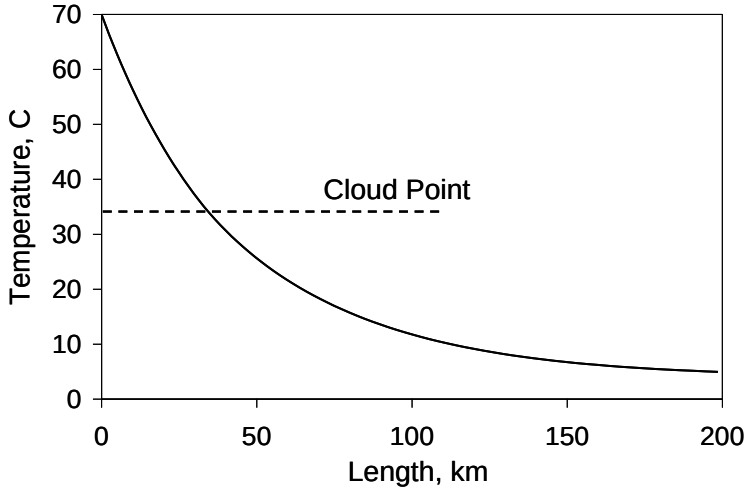

Figure 2-8: Inner wall temperature profile along the pipe as the base case after 180 days

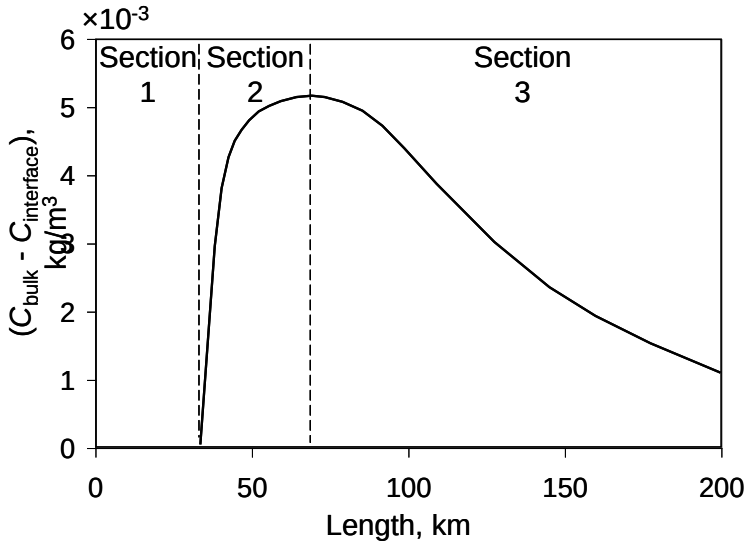

Figure 2-9: Driving force between concentration at the bulk and at the interface.

Figure 2-10 shows the axial profile of the predicted wax fraction in the deposit. Similar to the thickness profile, the wax fraction has a maximum in the pipe where the radial driving force for mass transfer is the greatest. The strength of the deposit strongly depends on its wax fraction. Therefore both the deposit thickness and wax fraction profile are important variables in planning remediation techniques the wax deposition.[15]

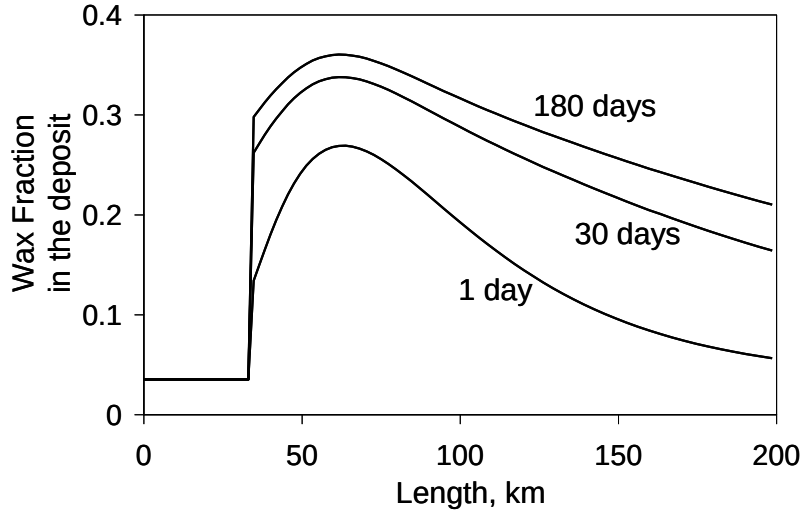

Figure 2-10: Wax fraction in the deposit along the pipe for the base case.

2.H.2 Comparisons of different precipitation kinetics

The previous field-scale prediction applied the kinetic method with a precipitation rate constant at the cloud point temperature, $k_{r,\,cloud}$ of 1.4 s^{-1}, This value is obtained from matching the model with the pilot-scale experiment. In order to compare the field-scale prediction using the kinetic method withthe IHMT model and the solubility model, simulations were carried out under the same operating conditions with the same crude oil with difference precipitation rate constants.

Figure 2-11 shows the comparison of the simulations for the three models. . The predicted deposit profiles using three different precipitation rate constants represent trends similar to the pilot scale predictions (Figure 2-5). One notes that using the independent heat and mass transfer method ($k_{r,\,cloud}$ = 0), the deposit thickness obtain a maximum at the outlet. This maximum is due to the assumption that no wax precipitation

occurs in the bulk even when the temperature at the outlet is near the ocean-floor temperature (Figure 2-8). This unrealistic assumption causes a significant over-estimation of the driving force for wax deposition and drastically over-predicts the growth of the deposit. On the other hand, assuming nearly instantaneous precipitation, the solubility model ($k_{r,\,cloud}$ = 10^3) significantly under-predicts the deposition thickness, causing a potential hazard for field remediation operations.

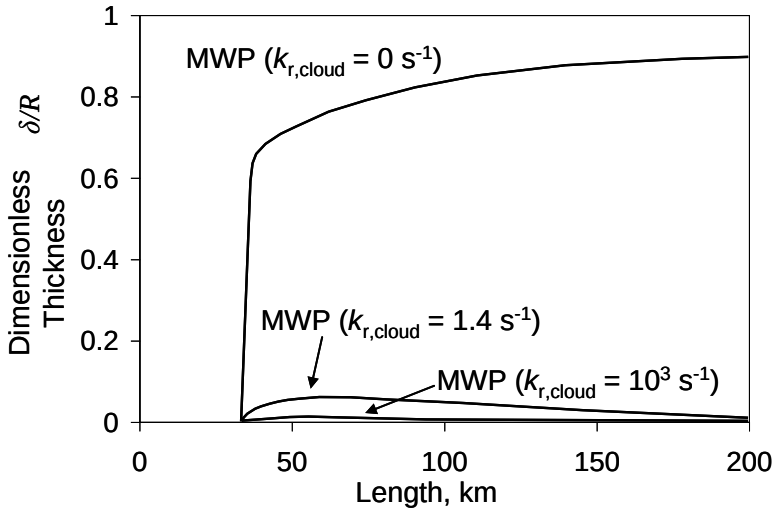

Figure 2-11: Comparison of field-scale predictions between different precipitation rate constants after 180 days.

2.H.3 The Effect of solubility curve in field-scale predictions

The solubility of waxes plays a very important role in wax deposition in field scale pipelines where the temperature of oil changes significantly along the pipe.[34] In this research, the effect of solubility on the wax deposition in field-scale pipelines is investigated by conducting wax deposition simulations for three oils: South Pelto crude oil,[35] (5 wt% wax, T_{cloud} = 49 °C), Garden Banks condensates[33] (3 wt% wax, T_{cloud} = 34.4 °C) and the model oil used by Singh and Fogler[14] (0.67 wt% wax, T_{cloud} = 13.9 °C).

The properties of these three oils were previously provided in Table 1. Figure 2-12 shows that the solubility curves of three oils. Two major elements in the solubility curve significantly affect wax deposition: the cloud point temperature and the gradient of the solubility curve. The cloud point of the oil det ermines the onset location of deposition in a subsea pipeline. The gradient of the solubility curve is a strong indicator of how much wax will precipitates on the wall when the temperature decreases along the pipe and thus greatly affects the amount of deposition.

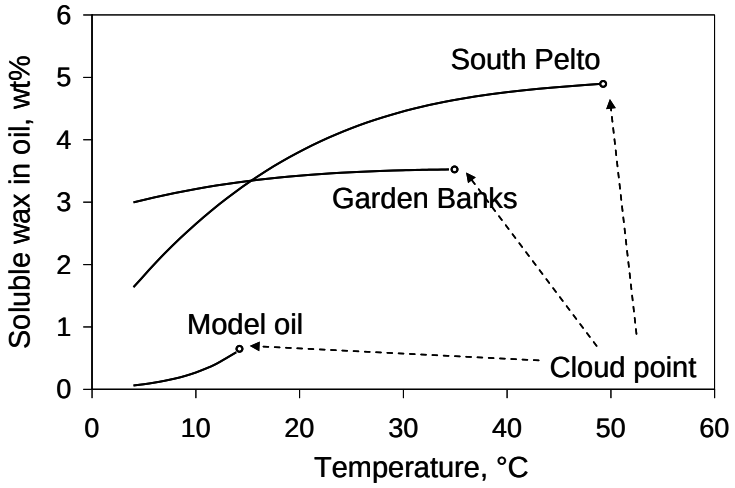

Figure 2-12 Solubility as a function of temperature of South Pelto Crude oil,[35] Garden Bank condensates[33] and a model oil.[14]

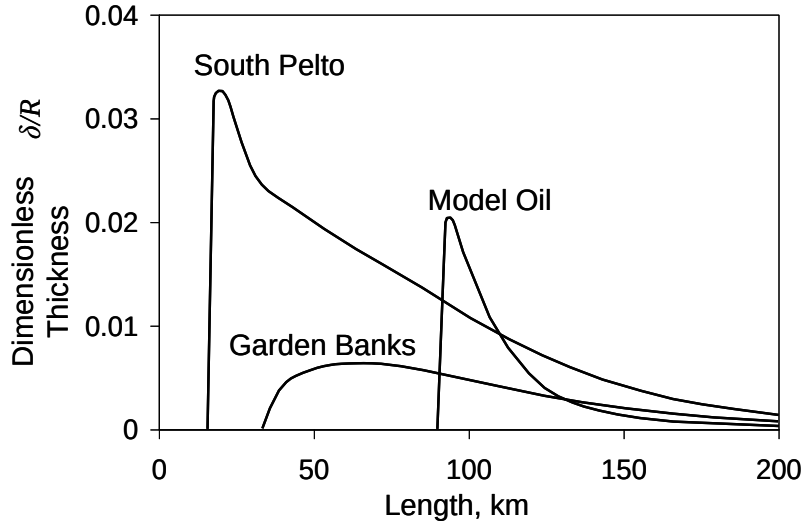

Figure 2-13 Axial thickness profiles for various oils. The input parameters used for these simulations are summarized in Table 2-2.

Figure 2-13 shows the axial profiles for the predicted deposit thickness for the three different oils after 180 days of continuous operation. The South Pelto oil has the highest cloud point and the greatest gradient in the solubility curve. Therefore its deposition occurs shortly after the inlet with a highest maximum of deposit. The model oil has the lowest clod point and its onset of deposition is furthest from the inlet. In addition, the Garden Bank condensate has the least gradient of solubility curve leading to a smallest maximum deposit in the pipe.

Meanwhile, one notes the difference in the deposition characteristics between a model oil system and a real oil system: in the case of model oil system significant deposition occurs over a relatively short short range (90 km – 140 km) of the pipe while significant deposition can be found in much longer portion of the pipe for the real oils (17 km – 200 km for South Pelto and 35 km- 200 km for Garden Banks). This difference is closely related to the difference in their compositions of normal paraffins, shown in Figure 2-14.

The model oil system has a narrower carbon number distribution of wax compared to the other real oils. Therefore when the temperature decreases along the pipe flow, precipitation in the model oil primary occurs over a certain section of the pipe within a small temperature range. On the other hand, the two other real oils have a broader carbon number distribution, causing significant precipitation to occur over a wide range of temperature, therefore deposition is seen in a large portion of the pipe.

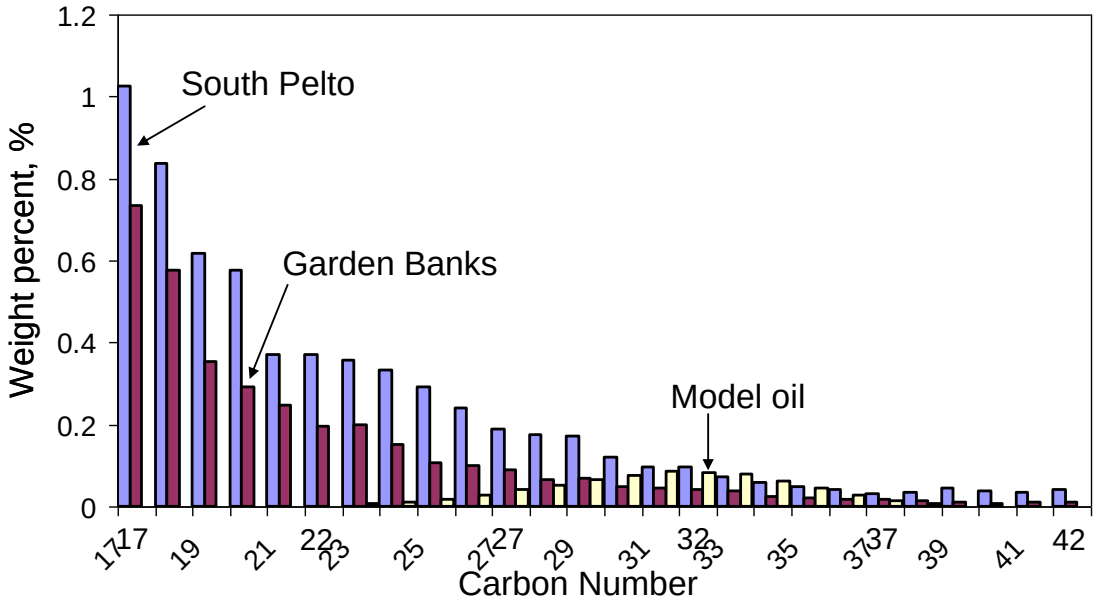

Figure 2-14 Comparison of the carbon number distribution of n-paraffin among the South Pelto oil[35], the Garden Banks[33] condensate and the model oil.[14]

2.I Conclusions

In this research, a general wax deposition prediction model was developed using fundamental heat and mass transfer analysis. The numerical solution of the coupled heat and mass transport equations revealed that the radial transport of wax molecules can be significantly reduced by the precipitation of wax molecules in the oil. The analysis showed that the computational model can be bounded by the Independent Heat and Mass Transfer model as the upper bound and the Solubility model as the lower bound, while

the wax deposition model using a finite value of specific precipitation parameter can successfully predict the thickness and aging of wax component in the deposit under various flow conditions.

The model was applied to wax deposition predictions at field-scale pipelines where the difference among the three aforementioned model is observed similar to lab-scale experiments. Furthermore, deposition occurs in a much shorter section of the pipe for the model oil than for the two real oils. This difference is due to the intrinsic difference in the carbon number distribution of the paraffins in the oil and its effect on the could point and the solubility curve.

Chapter 3

A Method to Determine the Wax Solubility Curve in Crude Oil from Centrifugation and High Temperature Gas Chromatography Measurements

3.A Introduction

In the previous chapter, we have discussed the development of the deposition model (the Michigan Wax Predictor, the MWP) based on fundamentals of heat and mass transfer theories. Before the application of the model to extensive wax deposition experiments, it is very important to confirm the validity of the input parameters to the model.

Among those input parameters, the solubility curve is of the greatest importance due to the fact that molecular diffusion has been shown to be the major mechanism for wax deposition.[14] In this case, the solubility curve represent the connection where heat transfer has cast great influence on mass transfer. In the Michigan Wax Predictor, the concentrations of wax in oil at the inlet and in the deposit are in solid-liquid thermodynamic equilibrium, which is shown previously in Equations (2.8) as the boundary conditions for Equation (2.4).

$$\begin{cases} C = C_{\text{inlet}}\left(\text{eq}\right),\ at\ z = 0\ \text{(inlet)} \\ \dfrac{\partial C}{\partial r} = 0,\ at\ r = 0\ \left(\text{centerline}\right) \\ C = C\left(\text{eq}\right),\ at\ r_{\text{d}} \le r \le r_{\text{i}}\ \left(\text{deposit}\right) \end{cases} \tag{2.8}$$

$$V_{\text{z}} \frac{\partial C}{\partial z} = \frac{1}{r}\frac{\partial}{\partial r}\left\lfloor r\left(\varepsilon_{\text{mass}} + D_{\text{wo}}\right)\frac{\partial C}{\partial r}\right\rfloor - k_{\text{r}}\left(C - C\left(\text{eq}\right)\right) \tag{2.4}$$

As we will see in detail during subsequent chapters, $\left\lfloor C_{\text{inlet}}\ (\text{eq}) - C_{\text{interface},\ r=r_{\text{i}}}\ (\text{eq})\right\rfloor$ represents the "mass driving force" for wax deposition and the solubility curve can have significant impact on wax deposition by affecting the mass driving force. In this chapter, we will find that although the solubility curve is vital to deposition modeling, this parameter is often quite difficult to measure accurately.

A number of techniques have been developed to determine the amount of precipitated wax in crude oil at different temperatures, including Differential Scanning Calorimetry (DSC), Fourier Transform Infrared Spectroscopy (FTIR), Nuclear Magnetic Resonance (NMR), High Temperature Gas Chromatography (HTGC), filtration and centrifugation, which can be categorized as direct methods and indirect methods.[36-46] Direct methods, such filtration and centrifugation, obtain the amount of precipitated wax by separating solid wax from the cooled crude oil. Indirect methods rely on measuring the change of another property that occurs because of wax precipitation.

A widely used indirect method to determine the wax precipitation curve is differential scanning calorimetry (DSC), which measures the heat released from wax precipitation.[37,43,46] By assuming a constant enthalpy of crystallization, the heat released by the crude during cooling is proportional to the amount of precipitated wax. The amount of precipitated wax at different temperatures can be determined by dividing the accumulated heat released by the enthalpy of crystallization. DSC is widely used because

of its simplicity and fast response. However, because the composition of precipitated wax changes as a function of temperature, the enthalpy of crystallization is temperature dependent.[46] In addition, the enthalpy of crystallization of the wax can vary widely depending on the composition of the crude oil. Hansen and Rønningsen showed that the enthalpies of crystallization for fourteen different crude oils from the North Sea ranged from 100 J/g to 297 J/g.[46] Although DSC provides a range for both the wax content and the wax precipitation curve; it cannot give an exact wax precipitation curve without knowing the enthalpy of crystallization.

Fourier Transform Infrared Spectroscopy (FTIR) is another method used to determine the wax precipitation curve by measuring the increase in the infrared absorbance of the crude oil sample caused by wax precipitation.[45] The increase in the integrated absorbance from 735 to 715 cm^{-1}, which corresponds to the CH_2 rocking band of *n*-alkanes, is assumed to be linearly related to the increase of weight percent of precipitated solid wax. However, for different *n*-alkanes, the same amount of increased absorbance in this band will not correspond to the same amount of *n*-alkane precipitated because the alkane CH_2 content varies, meaning that the linear relationship is not completely accurate.

Filtration and centrifugation provide direct methods to measure the amount of precipitated wax by separating the precipitated wax from the cooled crude oil.[36-38] However, a significant amount of liquid crude oil can be entrapped in the filtered and centrifuged cakes, requiring the use of techniques such as ^1H NMR or HTGC, is also needed to evaluate the solid wax content.

The ^{1}H NMR technique provides the amount of aromatics in crude oil by measuring the amount of hydrogen atoms in the aromatic rings (H_{ar}), and also the amount of hydrogen atoms next to functional groups (H_{α}), methylene hydrogen atoms (H_{β}), and methyl hydrogen atoms (H_{γ}).[39, 46] Because aromatics are highly soluble in crude oil, they are assumed to exist solely in the liquid phase.[39] Using the amount of H_{ar} in crude oil (H_{arC}) and filtered cake (H_{arM}), Martos et al. proposed an equation to calculate the percent of entrapped oil in the cake, as shown in Equation (3.1). Unfortunately, the low ratio of signal to noise of ^{1}H NMR gives a very significant relative error.[39,46]

$$\text{Entrapped oil}(wt\%) = \frac{H_{\mathrm{arM}}}{H_{\mathrm{arC}}} \times 100\% \tag{3.1}$$

The carbon number distribution obtained by high temperature chromatography (HTGC) provides another approach to determine the solid fraction in the filtered and centrifuged cakes. For the filtered cakes, Martos et al. chose a starting carbon number of 15, meaning that components with carbon numbers less than 15 will remain in the liquid phase and components with carbon numbers greater than fifteen will solidify.[39] However, Roehner et al. developed a different method to determine the starting carbon number of precipitated wax as a function of temperature.[36] Assuming that the non *n*-alkane components are present entirely in the liquid, Roehner et al.'s starting carbon number is the carbon number where the ratio of weight percent of *n*-alkane to non *n*-alkane in the cake is higher than that in the crude oil.[36]

The major limitation in these previous studies using HTGC comes from their methods to calculate the solid fraction from the experimental results. Using the *n*-alkanes distribution provided by Nenniger Engineering Company, the Marathon Oil Company accounted for all of the heavy *n*-alkanes (C22+) as solid wax (referred to as Marathon-

Nenniger method in this work).[38] Roehner et al. and Martos et al. account for all the heavy components including both *n*-alkane and non-*n*-alkanes as precipitated wax.[36,39] However, research has shown that those heavy components in the crude oil exist both the solid and liquid phases at a particular temperature because of solid-liquid equilibrium.[43,47-49] If there are significant amounts of heavy components dissolved in the liquid phase, the amount of precipitated wax will be drastically overestimated. Our work overcomes this problem by utilizing a mass balance on the centrifugation process and by using HTGC to appropriately address how each carbon number distributes in the liquid and solid phases. The wax solubility curve of a crude oil was developed using this method and compared with the solubility curves determined by DSC, Marathon-Nenniger method and Roehner et al.'s method.

3.B Analysis of the Centrifugation-HTGC Method

To determine the fraction of precipitated wax in crude oil using centrifugation and HTGC, four major steps are required as shown in Figure 3-1:

1) Cooling a known mass (m_{crude}) of a crude oil sample to a specific temperature

2) Centrifuging the crude oil at the specified temperature. Separating the cake from the supernatant and measuring the mass of the cake (m_{cake})

3) Performing a HTGC analysis on the cake to obtain the fraction of solid wax ($F_{\text{S,cake}}$) in the cake

4) Calculating the fraction of precipitated wax in crude oil ($F_{\text{S,crude}}$) using Equation (3.2).

$$F_{\text{S,crude}} = \frac{m_{\text{cake}} \cdot F_{\text{S,cake}}}{m_{\text{crude}}} \tag{3.2}$$

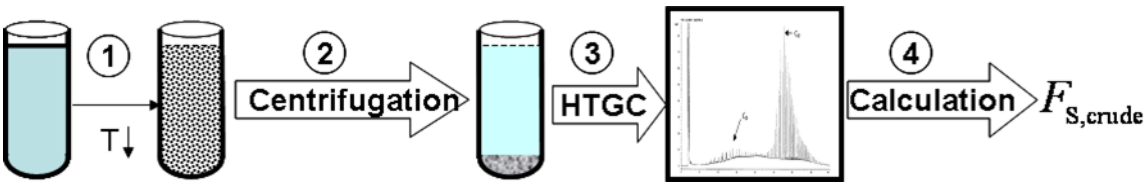

Figure 3-1: Sketch of the experimental procedure for determining the weight percent of precipitated wax in crude oil using centrifugation and HTGC

As discussed earlier, the liquid oil entrapped in the centrifuged cakes creates a problem in determining the solid fraction in the centrifuged cake using HTGC. In this work, an equation was derived from a mass balance on the centrifugation process. As shown in Figure 2, the centrifugation consists of one feed stream and two output streams with four unknown variables: the mass of solid wax particles in the cooled crude ($m_{S,crude}$) and in the cake ($m_{S,cake}$), the mass of liquid oil in the crude, ($m_{L,crude}$) and in the cake ($m_{L,cake}$). Solving for these four unknown variables requires four equations that relate the variables to one another. The mass balance before and after centrifugation yields three equations.

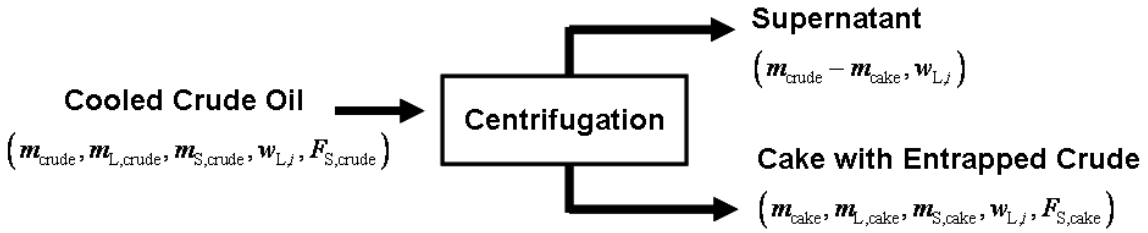

Figure 3-2: System analysis on the centrifugation process

1. The mass of the crude oil sample is the sum of the liquid and solid in the cooled crude oil, as shown in Equation (3.3).

$$m_{crude} = m_{L,crude} + m_{S,crude} \tag{3.3}$$

2. The mass of the centrifuged cake is the sum of the liquid and solid in the cake, as shown in Equation (3.4).

$$m_{\text{cake}} = m_{\text{L,cake}} + m_{\text{S,cake}} \tag{3.4}$$

3. Because the centrifugation is performed isothermally, it is assumed that no further wax precipitation occurs. The solid in the crude oil sample will be entirely in the cake after centrifugation, as given in Equation (3.5).

$$m_{\text{S,crude}} = m_{\text{S,cake}} \tag{3.5}$$

Combining Equations (3.3), (3.4) and (3.5) gives Equation (3.6).

$$m_{\text{cake}} = m_{\text{L,cake}} + m_{\text{S,cake}} \tag{3.6}$$

In this work, the components including both *n*-alkane and non-*n*-alkane with same carbon number are regarded as one group. Taking the weight fraction of all the components with carbon number *i* in the liquid phase as $w_{\text{L},i}$ and the weight fraction in the precipitated solid as $w_{\text{S},i}$, the weight fraction of all the components with carbon number *i* in the crude oil sample($w_i\big|_{crude}$) and in the cake ($w_i\big|_{cake}$) are given in Equations (3.7) and (3.8). The entrapped oil (L) in the cake, the corresponding supernatant and the liquid in the pre-centrifuged crude oil all have the same composition denoted as $w_{\text{L},i}$.

$$w_i\big|_{\text{crude}} = \frac{m_{\text{L,crude}} \cdot w_{\text{L},i} + m_{\text{S,crude}} \cdot w_{\text{S},i}}{m_{\text{crude}}} \tag{3.7}$$

$$w_i\big|_{\text{cake}} = \frac{m_{\text{L,cake}} \cdot w_{\text{L},i} + m_{\text{S,cake}} \cdot w_{\text{S},i}}{m_{\text{cake}}} \tag{3.8}$$

The lowest carbon number present in the precipitated wax is defined as N_C. For all the components with carbon numbers less than N_C, Equations (3.7) and (3.8) can be reduced to Equations (3.10) and (3.11) because $w_{S,i} = 0$.

$$w_i\big|_{\text{crude}(i<N_C)} = \frac{m_{L,\text{crude}} \cdot w_{L,i}}{m_{\text{crude}}} \tag{3.9}$$

$$w_i\big|_{\text{cake}(i<N_C)} = \frac{m_{L,\text{cake}} \cdot w_{L,i}}{m_{\text{cake}}} \tag{3.10}$$

Combining Equations (3.9) and (3.10) yields Equation (3.11).

$$\frac{m_{L,\text{cake}}}{m_{L,\text{crude}}} = \frac{w_i\big|_{\text{cake}(i<N_C)}}{w_i\big|_{\text{crude}(i<N_C)}} \cdot \frac{m_{\text{cake}}}{m_{\text{crude}}} \tag{3.11}$$

As can be observed from Equation (3.11), for all of the components with a carbon number less than N_C, the ratio between its weight percent in the cake and that in the crude oil is the same, defined as *a* in Equation (3.12).

$$a = \frac{w_i\big|_{\text{cake}(i<N_C)}}{w_i\big|_{\text{crude}(i<N_C)}} \tag{3.12}$$

We also define the ratio of the mass of the cake to the mass of the crude oil sample as *b*, shown in Equation (3.13).

$$b = \frac{m_{\text{cake}}}{m_{\text{crude}}} \tag{3.13}$$

By solving Equations (3.3) - (3.5) and (3.11) simultaneously, the solid fraction in the cake, $F_{S,\text{cake}}$ and in the crude oil, $F_{S,\text{crude}}$ can be determined as shown in Equations (3.14) and (3.15).

$$F_{S,\text{cake}} = \frac{m_{S,\text{cake}}}{m_{\text{cake}}} = \frac{1-a}{1-ab} \tag{3.14}$$

$$F_{S,crude} = \frac{m_{S,cake}}{m_{crude}} = \frac{b - ab}{1 - ab} \tag{3.15}$$

3.C Experimental Section

3.C.1 Crude oil:

The crude oil used for this research is a condensate from the North Sea provided by Statoil.

3.C.2 Centrifugation:

A Beckman Instruments centrifuge (model L8-70) with a temperature-controlled chamber was used to centrifuge the crude oil samples. The 50-mL centrifuge tubes used to hold the crude oil are equipped with an O-ring and a cap to prevent the loss of light ends during testing. To ensure that no solid wax is present in the sample, the crude oil was heated to 60°C (30˚C higher than the WAT) and held at that temperature for 2 hours before being transferred into the tubes. The filled centrifuge tubes were weighed before being transferred into the rotor head. The tubes and centrifuge chamber were cooled to the specified temperatures (30˚C, 20˚C, 10˚C, and 5°C). The samples were centrifuged at 25000 rpm for 20 hours. After the centrifugation, the liquid phase was drained and each tube was swabbed to remove any residual liquid. The tubes were re-weighed to obtain the mass of the centrifuged cake.

3.C.3 High Temperature Gas Chromatography (HTGC):

The carbon number distributions of crude oil and centrifuged cake were both measured using gas chromatography. The crude oil is measured using a Hewlett-Packard

6890A GC equipped with capillary column coated with DB-1 (40m x 0.100mm x 0.20μm). The oven temperature was initiated at 30˚C and increased to 80˚C at a rate of 2.8˚C/min, then to 170˚C at a rate of 5.7˚C/min.

To give a higher resolution on heavy alkanes, the centrifuged cakes were analyzed using a high temperature gas chromatograph (HTGC) Hewlett-Packard 6890A equipped with a CP-SimDist Ultimetal column (25m x 0.53mm x 0.09mm). The oven temperature was initiated at 40˚C and increased to 430˚C at a rate of 10˚C/min. The internal standard method was used for the cakes analysis.

3.C.4 Differential Scanning Calorimeter (DSC):

The calorimetric measurements were performed using a TA® Q2000 DSC. The crude oil is first heated to 60˚C, held at this temperature for one hour and then cooled from 60˚C to -50˚C at a rate of 0.5˚C/min.The DSC trials allowed for the determination of the onset of a liquid-solid transition and the amount of heat released in transition from liquid to solid.

3.D Result and Analysis

3.D.1 Determination of the starting carbon number of precipitated wax, N_C

The starting carbon number, N_C is the lowest carbon number present in the precipitated wax and thus any components with carbon number below N_C will be entirely present in the liquid phase. In this work, the method presented by Roehner et al. was used to determine the starting carbon number of precipitated wax.[1] The details of this method are shown in Appendix A. The starting carbon numbers of precipitated wax at 5˚C, 10˚C,

20˚C and 30˚C were determined and listed in Table 3-1. It can be seen the starting carbon number of precipitated wax increased as a function of temperature.

Table 3-1: The starting carbon number of precipitated wax at different temperatures

Temperature, ˚C	Starting carbon number of precipitated wax, N_C
5	21
10	21
20	28
30	34

3.D.2 Comparison of normalized carbon number distribution in the cakes and in the crude oil

To make a proper comparison of the carbon number distribution in the cakes and in the crude oil, the carbon number distribution in the cakes and in the crude oil are optimized using a normalization procedure, discussed in detail as follows:

Because the amount of precipitation for a certain component increases with decreasing temperature, if one component does not precipitate at a certain temperature, it does not precipitate at any higher temperatures. Table 3-1 shows that the lowest starting carbon number was 21 for the cake obtained at 5˚C, indicating that all the components with carbon number less than 21 are solely present in the liquid phase at all temperatures above 5˚C. Additionally, the amount of those components is decreased by discarding the supernatant after centrifugation. Therefore for those components, their weight fractions in the cake are supposed to be lower than their weight fractions in the crude oil i.e. $w_{i,(i<21,\text{cake})} < w_{i,(i<21,\text{crude})}$ at all the temperatures higher than 5˚C. The weight percent of those components in the crude oil are shown in Table 2. However, Figure 3-3 shows that those components have a higher weight fraction in the cake than in the oil. This

inconsistency is mainly because of the experimental limitation introduced by the internal standard method used for GC analysis. The internal standard method requires knowledge of the weight percent of internal standard in the sample. The weight percent of component *i* can then be determined by taking the ratio of peak area of component *i* to the internal standard. However, because the internal standard cannot be properly distributed within the cake samples, the reported weight percent of internal standard in sample will deviate from its true value. As a result of this deviation, it can be seen in Figure 3-4 that the sum of the components with carbon number larger than 15 do not increase with decreasing temperature as expected. However, because the ratios among the weight percents of the components are unaffected by the internal standard concentration in the sample, a normalization procedure can be used to overcome this issue.

Table 3-2: Carbon number distribution of crude oil

Components	Wt%	Mole%	MW(g/mol)	Components	Wt%	Mole%	MW(g/mol)
N2	0.00	0.00	28.01	C17	2.93	2.17	237
CO2	0.00	0.00	44.00	C18	3.17	2.21	251
H2S	0.00	0.00	34.08	C19	2.75	1.83	263
C1	0.00	0.00	16.04	C20	2.24	1.42	275
C2	0.00	0.00	30.07	C21	2.05	1.23	291
C3	0.01	0.03	44.10	C22	1.92	1.12	300
ISO-C4	0.04	0.12	58.12	C23	1.80	1.01	312
N-C4	0.33	0.99	58.12	C24	1.64	0.88	324
ISO-C5	0.56	1.37	72.15	C25	1.59	0.82	337
N-C5	1.14	2.77	72.15	C26	1.56	0.78	349
C6	2.83	5.83	85.1	C27	1.21	0.59	360
C7	6.54	12.58	91.0	C28	1.41	0.66	372
C8	8.91	15.03	103.8	C29	1.29	0.59	382
C9	6.29	9.08	121.3	C30	1.16	0.52	394
C10	4.45	5.81	134	C31	1.01	0.44	404
C11	4.80	5.72	147	C32	0.91	0.38	415
C12	4.31	4.68	161	C33	0.83	0.34	426
C13	4.27	4.27	175	C34	0.70	0.28	437
C14	4.03	3.71	190	C35	0.41	0.16	445
C15	3.74	3.18	206	C36+	14.03	4.92	499
C16	3.14	2.48	222	Total	100.00	100.00	

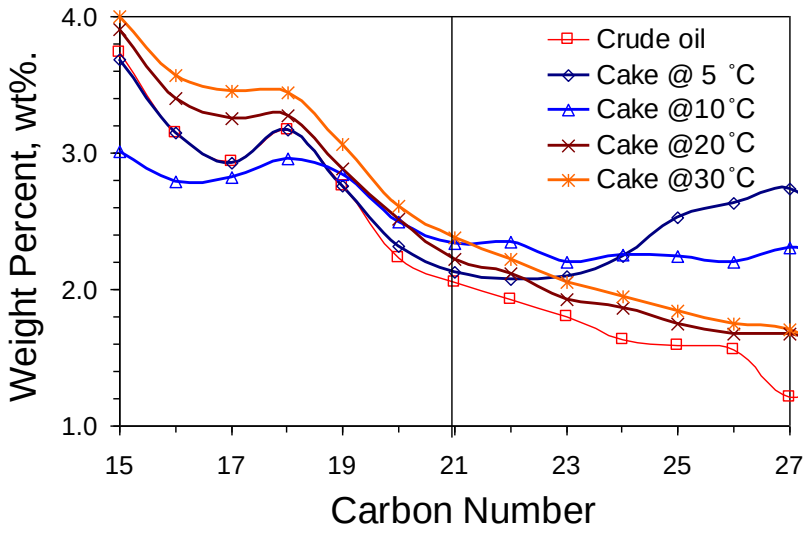

Figure 3-3: Comparison of the measured carbon number distribution in the cake and the crude oil

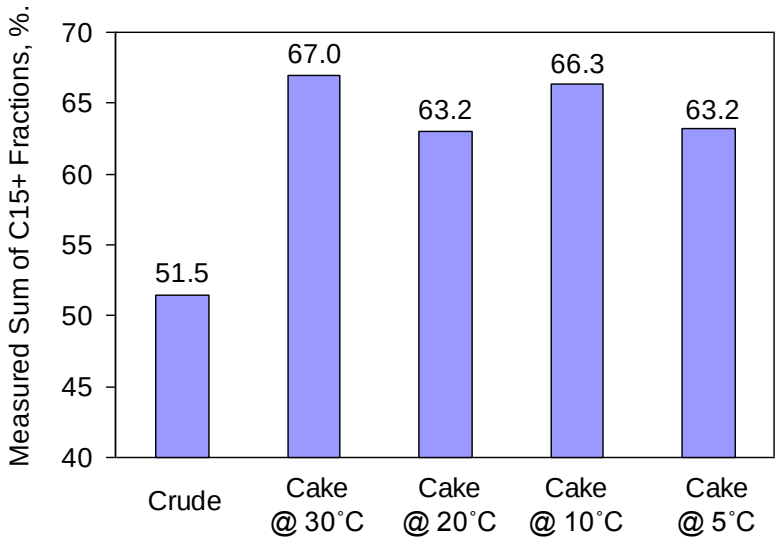

Figure 3-4: Comparison of measured values of sum of C15+ in the cakes and crude oil

The normalization procedure was carried out for the weight percent of components with carbon numbers larger than fifteen. As shown in Equation (3.16), the normalized

weight percent of component i, $w_i\big|_{\text{cake or crude}}^{\text{normalized}}$, was obtained by dividing the measured weight percent, $w_i\big|_{\text{cake or crude}}^{\text{measured}}$ by the sum of measured C15+ fractions, $\sum_{C15+} w_i\big|_{\text{cake or crude}}^{\text{measured}}$.

$$w_i\big|_{\text{cake or crude}}^{\text{normalized}} = \frac{w_i\big|_{\text{cake or crude}}^{\text{measured}}}{\sum_{C15+} w_i\big|_{\text{cake or crude}}^{\text{measured}}} \tag{3.16}$$

Figure 3-5 shows the comparison of the normalized carbon number distributions of the components in the crude oil to the cakes obtained at different temperatures. As expected, the components with carbon numbers less than N_C have a higher weight percent in the crude oil than in the cake and the components with carbon numbers larger than N_C have a higher weight percent in the cake than in the crude oil. It should be noted that there is a peak for the weight percent distribution of the heavy carbon numbers in the cakes. This peak carbon number increased as a function of temperature, indicating more components with lower carbon numbers precipitated out at lower temperatures.

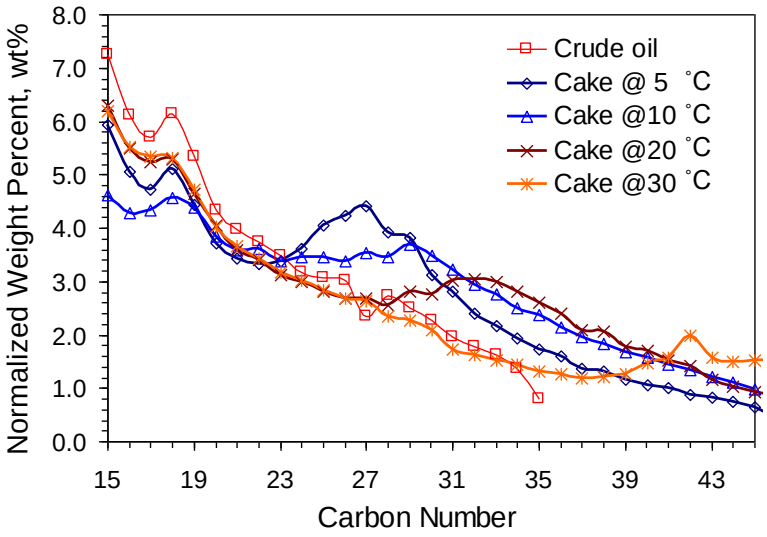

Figure 3-5: Comparison of the normalized carbon number distribution in the cake and the crude oil

3.D.3 Application of new method to calculate the amount of precipitated wax

To apply the new method using normalized carbon number distributions in the cakes and in the crude oil, two more variables, *k* and *r* are necessary to be introduced. For the light components with carbon numbers less than N_C, *k* refers to the ratio of the normalized weight percent of component *i*, in the cake to that in the crude oil, as shown in Equation (3.17).

$$k = \frac{w_i\big|^{\text{normalized}}_{\text{cake}(i<N_C)}}{w_i\big|^{\text{normalized}}_{\text{crude}(i<N_C)}} \tag{3.17}$$

The variable *r* refers to the sum of fractions of components excluded in the normalization. In this case, *r* is the sum of components with carbon numbers less than 15, as shown in Equation (3.18). The value of *r* was obtained from the carbon number distribution of crude oil shown in Table 3-2 as 0.485.

$$r = \sum_{i<15} w_{i,\text{crude}} \tag{3.18}$$

Using *k* and *r*, *a* can be expressed using Equation (3.19), as shown in Appendix B.

$$a = \frac{k}{1-r+kr} \tag{3.19}$$

Equation (3.19) shows that *k* should be constant for all of the components with carbon numbers less than N_C. However, because of experimental deviation, this result was not seen. To obtain the proper value of *k*, the root mean square deviation (RMSD) between the scaled crude oil weight percent distribution and the normalized carbon number distribution of the cake was minimized, as shown in Equation (3.20).

$$\text{RMSD} = \sqrt{\frac{\sum_{15}^{N_C}\left(k\, w_i\big|^{\text{normalized}}_{\text{crude}} - w_i\big|^{\text{normalized}}_{\text{cake}}\right)^2}{N_C - 15 + 1}} = \text{minimum} \tag{3.20}$$

Figure 3-6 shows that the scaled carbon number distribution in crude oil matches the weight percent distribution in the cakes obtained at 30˚C, 20˚C and 5˚C.

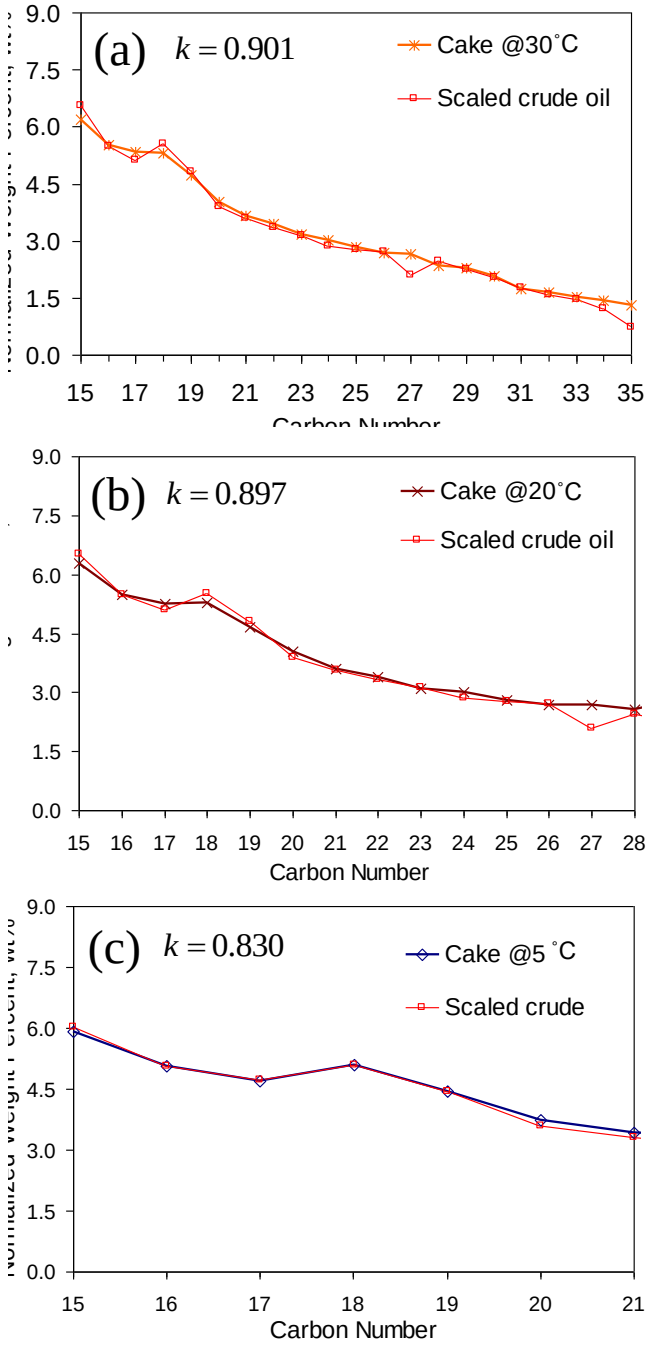

Figure 3-6: Comparison of the normalized carbon number distribution in cakes and scaled carbon number distribution in the crude oil: (a) the cake obtained at 30˚C, (b) the cake obtained at 20˚C and (c) the cake obtained at 5˚C

For the cake obtained at 10˚C, the normalized carbon number distribution based on components greater than C19 instead of C15. This change is because of the experimental limitation of measuring the weight percent of components with carbon numbers less than 19 at this temperature. According to the carbon number distribution in the crude oil, each of the components C15 to C18 has a higher weight percent than C19. Because the components up to C19 will exist entirely in the liquid phase at temperature of 10˚C, this trend should maintain in all the cakes. Contrarily, Figure 3-5 shows a lower weight percent of each of C15 to C18 than C19 in the cake obtained at 10˚C. In order to overcome this experimental limitation, the normalized carbon number distribution of the cake obtained at 10˚C is based on components greater than C19 instead of C15. Figure 3-7(a) shows the comparison of normalized carbon number distribution of the crude oil and the cake obtained at 10˚C. Using a value of 0.781 for *k*, Figure 3-7(b) shows that the scaled carbon number distribution of crude oil matches the cake obtained at 10˚C.

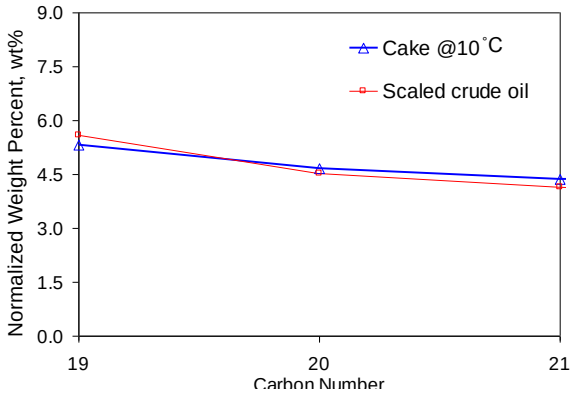

Figure 3-7: (a) Comparison of normalized carbon number distribution in the crude oil and the cake obtained at 10˚C; (b) Comparison of normalized carbon number distribution of the cake and scaled carbon number distribution of the crude oil

Table 3-3 lists the values of the relevant variables. It can be seen the weight percent of solid in the cake is less than 12%, indicating that a large amount of liquid is entrapped

in the centrifuged cakes. Using the weight percent of precipitated wax in crude oil at 5˚C, 10˚C, 20˚C and 30˚C, the wax precipitation curve was obtained, presented in Figure 3-8. As expected, Figure 3-8 shows that the amount of precipitated wax increases with decreasing temperature.

Table 3-3: The solid fraction in centrifuged cakes and crude oil at different temperatures

Temp., ˚C	Trial	*K*	*r*	*a*	*b*	$F_{s,cake}$, wt%	Average $F_{s,cake}$, wt%	$F_{s,crude}$, wt%	Average $F_{s,crude}$, wt%
5	1	0.830	0.485	0.905	0.128	10.78	11.02	1.38	1.41
	2	0.823	0.485	0.901	0.128	11.25		1.44	
10	1	0.781	0.615	0.903	0.086	10.56	8.91	0.91	0.77
	2	0.843	0.615	0.933	0.086	7.26		0.63	
20	1	0.897	0.485	0.944	0.025	5.70	8.44	0.14	0.21
	2	0.808	0.485	0.891	0.025	11.18		0.28	
30	1	0.901	0.485	0.947	0.007	5.37	4.60	0.04	0.03
	2	0.929	0.485	0.962	0.007	3.83		0.03	

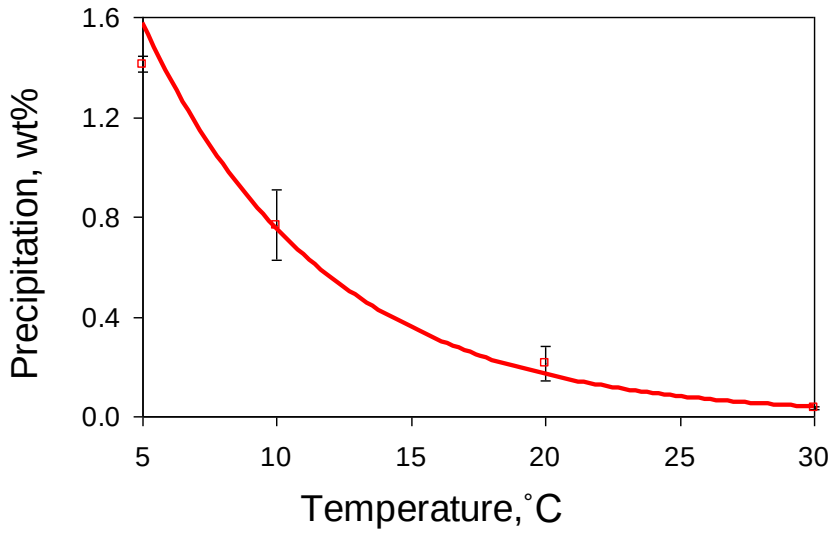

Figure 3-8: Wax precipitation curve determined by the new method

3.D.4 Comparison of the precipitation curve determined using DSC, Roehner et al.'s method, Marathon-Nenniger method and the new method

Figure 3-9 shows the DSC curve of the crude oil. The wax appearance temperature (WAT) is measured to be 27˚C and no further wax precipitation is seen below -24˚C. The heat released by wax precipitation was found to be 4.0 J/g. It must be noted that a centrifuged cake has been obtained at 30˚C, which is higher than the WAT determined by DSC. This discrepancy is most likely seen because of the effect of cooling rate on wax crystallization.

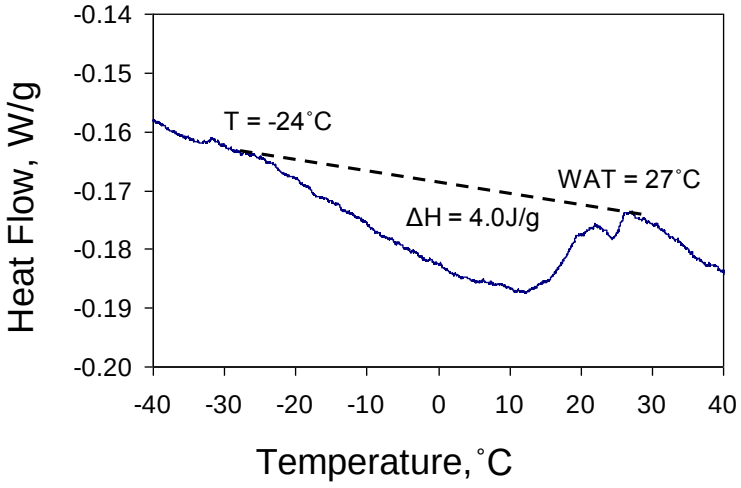

Figure 3-9: DSC curve of the crude oil

Assuming that the heat released is proportional to the mass of precipitated wax, the fraction of crystallized wax in the total wax content is the same as the percent of accumulated heat released in the total heat released. Figure 3-10 shows how the percent of accumulated heat released changes from 0 to 100% as the temperature was decreased from 27˚C to -24˚C. This heat release can be used to determine the amount of precipitated wax at different temperatures.

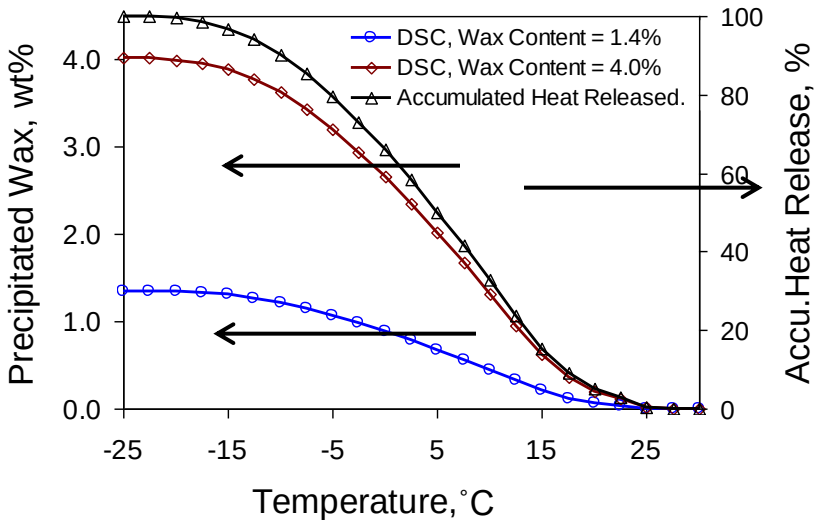

Figure 3-10: Comparison of the wax precipitation curve determined by DSC and the new method

Because of the complex composition of crude oil, no universal value exists for the enthalpy of crystallization of wax for crude oil. According to Hansen and Rønningsen's research on fourteen kinds of crude oil from the North Sea using DSC-NMR, the measured enthalpy of crystallization of wax was found to range between 100 J/g and 297 J/g.[45] For the crude oil used in this research, these two values of enthalpy of crystallization give the lower and upper bound of wax content, 1.3% and 4.0%. Corresponding to these two values, two wax precipitation curves were obtained, as shown in Figure 3-10 and Figure 3-11.

Table 4 lists the amount of precipitated wax determined by the Roehner et al. method, the Marathon-Nenniger method, the DSC method and the new method. The comparison of the wax precipitation curve determined by previous methods and the new method was shown in Figure 11. It can be seen both Roehner et al.'s method and the Marathon-Nenniger method give a significant over-prediction of the amount of precipitated wax.

These values are higher than the upper bound provided by DSC. As discussed earlier, this over-prediction results from the limitation of ignoring all the dissolved heavy components for Roehner et al.'s method and ignoring the dissolved heavy *n*-alkanes for the Marathon-Nenniger method. Meanwhile, it can be seen that the precipitation curve developed using the new method lies between the two DSC-determined precipitation curves.

Table 3-4: The amount of precipitated wax (wt%) determined using different methods

Temperature, ˚C	*Roehner et al.*	*Marathon-Nenniger*	*DSC, with wax content 1.4%*	*DSC, with wax content 4.0%*	This work
5	5.13	2.51	0.68	2.01	1.41
10	3.19	1.47	0.44	1.32	0.77
20	0.71	0.40	0.07	0.20	0.21
30	0.12	0.07	0.00	0.00	0.03

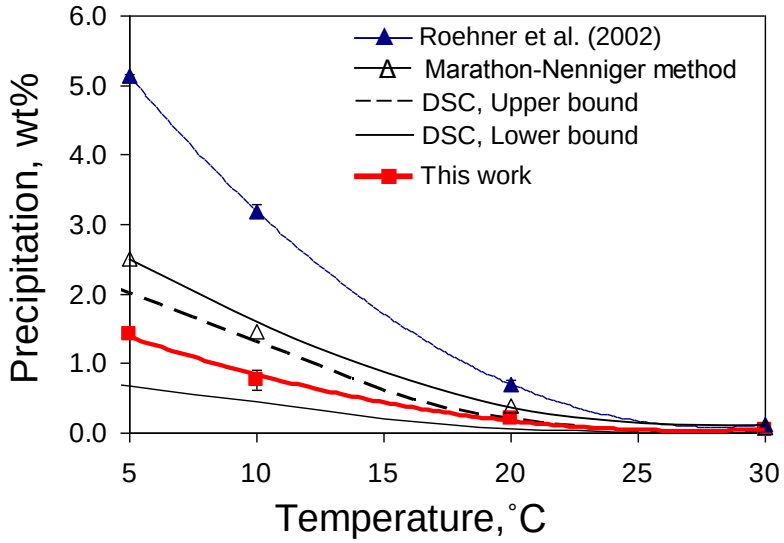

Figure 3-11: Comparison of the wax precipitation curves determined using DSC, Roehner et al.'s method the Marathon-Nenniger method and the method developed in this work

3.D.5 Comparison of the solubility curve determined using DSC, Roehner et al.'s method and the newly developed method

The wax solubility curve can be obtained with known the wax precipitation curve and wax content. Because the sea floor temperature is around 4˚C, the amount of precipitated wax at 5˚C is assumed to be the wax content used to obtain all the solubility curves, shown in Figure 12.

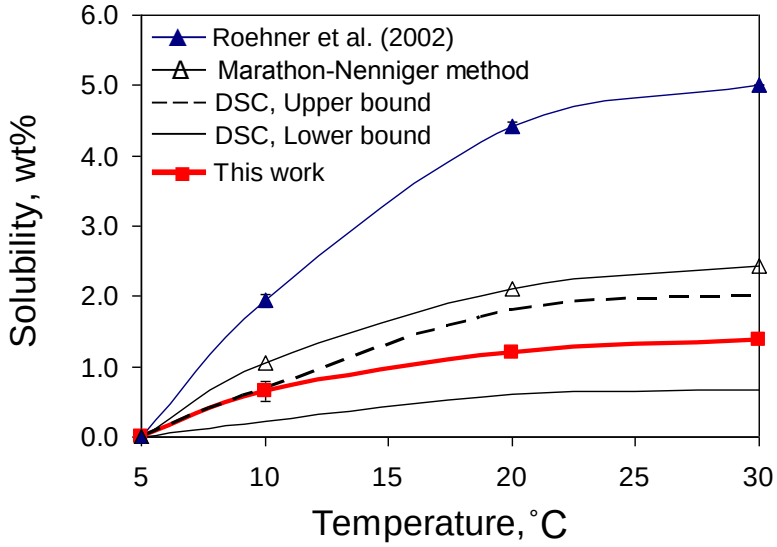

Figure 3-12: Comparison of the wax solubility curves determined using DSC, Roehner et al.'s method, the Marathon-Nenniger method and the new method developed in this work

From Figure 3-12, it can be seen that both Roehner et al.'s method and Marathon-Nenniger method give a higher gradient of wax solubility to temperature then the new method. As discussed previously, the gradient of solubility with respect to temperature greatly affects the thickness of the wax deposit. To show this effect on wax deposition modeling, the solubility curves from Roehner et al.'s method, the Marathon-Nenniger method and this work were used in a wax deposition simulation using the *Michigan Wax Predictor* (MWP) developed in Chapter 2. Simulations were carried out to predict a flow loop wax deposition experiment equipped with a pipeline of a length of 5.5 m and an

inner diameter of 52.5 mm. The crude oil inlet temperature is 20˚C, the coolant temperature is 10˚C, and the crude oil flow rate is 15m^3/h. The experimental deposit thickness was obtained by measuring the pressure drop within the pipe. Figure 3-13 shows the comparison of thickness of deposit seen experimentally and MWP simulated results using the different solubility curves. It can be seen that both solubility curves from Roehner et al.'s method and the Marathon-Nenniger method significantly over-predict the growth of the deposit thickness. After 160 hours, the over-prediction reaches 300% for Roehner et al.'s solubility curve and 200% for the Marathon-Nenniger method. Meanwhile, the solubilitycurve developed by the new method provides a more accurate prediction.

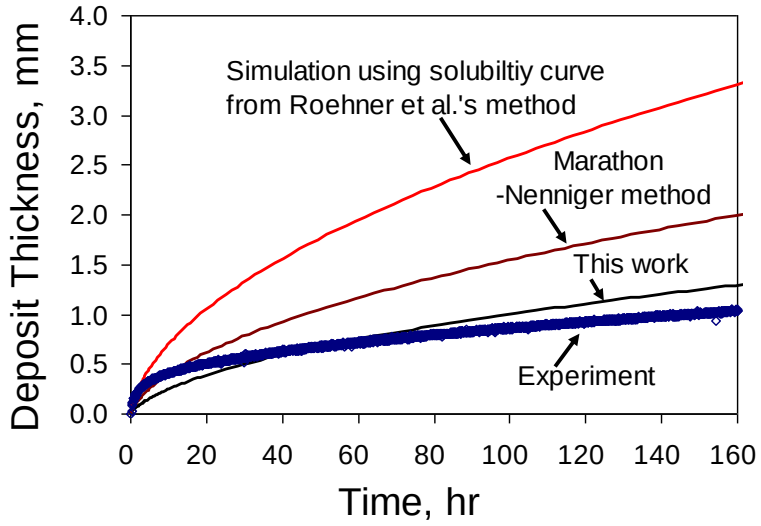

Figure 3-13: Comparison of deposit thickness profile between experimental results from flow loop experiment and simulation results from MWP using the solubility curves determined by Roehner et al.'s method, the Marathon-Nenniger method and the new method developed in this work

3.E Conclusions

The wax solubility/precipitation curve is of primary importance in wax deposition studies and modeling. This work analyzed previously published methods used to

determine the weight percent of precipitated wax in crude oil using centrifugation and HTGC. It has been found that previous methods overestimate the solid fraction in the centrifuged cake because it counts the dissolved heavy components as precipitated wax. In order to overcome this shortcoming, a complete mass balance analysis was carried out on the centrifugation process. The ratios of weight percents for carbon numbers less than the starting carbon number of precipitated wax in the cake to the crude oil were found to be constant. Using this constant, an equation to calculate the solid fraction in the cake and crude oil was developed. Based on a series of centrifugation experiments carried out on a crude oil at different temperatures along with the HTGC analysis on centrifuged cakes, the wax precipitation curves in crude oil were obtained. The newly developed wax precipitation curve falls in the range provided by DSC, while the previous methods are higher than this range.

Chapter 4

The Effect of Operating Temperatures on Wax Deposition

4.A Introduction

As we have illustrated the development of the Michigan Wax Predictor (MWP) in Chapter 2 and introduced a method for accurate solubility measurement as the most important input to the model in Chapter 3. The MWP shall be applied to the study of extensive wax deposition experiments.

Over the past few decades, many lab-scale experimental studies have been carried out for different operating conditions, where the effect of temperature has been extensively studied.[50-53] Cold-finger and flow-loop experiments are the two commonly used apparatii. In cold-finger experiments, a small cylindrical metal heat exchanger (the cold-finger) is maintained at a lower temperature and is submerged in a bulk crude oil of a higher temperature. The temperatures of the cold-finger and the bulk crude oil are controlled by two separate water baths. By changing the bulk oil temperature and the cold-finger temperature, the wax deposition can be studied for different thermal gradients.[50,51] Although the cold-finger experiments provide some insights on wax deposition, it certainly is not a direct representation of wax deposition in field-scale pipelines because of the difference in geometries and flow fields between a cold-finger system and a flow-loop system.[52] Flow-loop apparatus better simulates the conditions for wax deposition in

subsea pipelines compared to cold-finger devices. Most flow-loops are equipped with an annular pipe where the crude oil flows in the inner pipe while the coolant flows through the annulus. By changing the operating temperatures, i.e. the temperatures of the oil and the coolant, the thermal conditions at different axial positions of the subsea pipeline can be simulated.[14,52,53]

In these studies described above, the temperature difference between the bulk oil and the coolant (or the cold finger temperature) is frequently referred to as the "thermal driving force" for wax deposition. A comparison of these studies is discussed to review the wax deposition characteristics for different temperature conditions.

4.A.1 Decreasing Wax Deposition with Decreasing Thermal Driving Force

Jennings et al. used a cold-finger apparatus and a crude oil from the Gulf of Mexico to study wax deposition at different cold-finger temperatures while the bulk temperature of oil was kept constant.[50] It was found that the experiments with higher cold-finger temperatures (smaller thermal driving force) yielded smaller amounts of deposit. Creek et al. found similar results using a flow-loop apparatus to study wax deposition for different coolant temperatures. Their study showed a decrease in the deposit thickness when the coolant temperature increased (decreasing thermal driving force).[52] In the study of Bidmus et al., four different inlet temperatures were examined while the coolant temperature was kept constant. It was found that a decrease in the oil temperature (decreasing thermal driving force) to near ambient or pipe-wall temperatures could substantially decrease wax deposition. In all the above studies, a generalization was made that the deposit thickness decreases when thermal driving force decreases. In the above studies the focus on the thermal driving force for wax deposition is based on the fact that

molecular diffusion was regarded as the most prevalent deposition mechanism.[14] In this mechanism, the mass flux of the wax molecules at the interface (from the oil towards the deposit) $\left(D_{\text{wo, interface}} \left.\frac{dC}{dr}\right|_{\text{at interface}} \right)$ represents the loss of wax from the oil to form a deposit. Among the parameters in the mass flux, the concentration gradient $\left(\left.\frac{dC}{dr}\right|_{\text{at interface}} \right)$ can be approximated by applying the chain rule and using two parameters: the radial temperature gradient, $\left(\left.\frac{\partial T}{\partial r}\right|_{\text{at interface}} \right)$ and the solubility gradient $\frac{dC}{dT}$, as shown in Equation (4.1).

$$D_{\text{wo, interface}} \left.\frac{dC}{dr}\right|_{\text{at interface}} \approx D_{\text{wo, interface}} \cdot \left(\left.\frac{dT}{dr}\right|_{\text{at interface}} \right) \cdot \left(\frac{dC}{dT}_{\text{at interface}} \right) \tag{4.1}$$

The first term of the RHS of Equation (4.1), namely the radial temperature gradient, has been the focus in previous studies where the thermal driving force has been consider as the major parameter to explain the temperature effects on wax deposition.[50,52,53] However, equally important is the solubility gradient at the oil-deposit interface, i.e. the second parameter on the RHS of Equation (4.1) and it is frequently overlooked in theoretical analyses. The solubility gradient reflects the effect of the shape of the solubility curve on wax deposition. For particular types of oil the impact on the solubility curve can overcome the effect of the temperature gradient when the operating conditions change.

4.A.2 Increasing Wax Deposition with Decreasing Thermal Driving Force

Cold-finger studies by Paso and Fogler on other oils at lower temperatures showed an opposite trend to that discussed above, where more wax molecules can precipitate and

form thicker deposits with decreasing temperature gradients.[51] Paso and Fogler explained that this trend was a result of an increase in the wax precipitation at the cold-finger surface, which is not accounted for in any of the previous studies. However, this trend had not been previously observed in flow-loop experiments until this work.

4.B Wax Deposition Experiments

In the study reported here, experiments consist of a series of experiments were carried out using a laboratory flow-loop in the Herøya Research Center of Statoil ASA in Porsgrunn, Norway. An oil from the North Sea identified as North Sea Oil A is provided by Statoil ASA and was used in this study for deposition experiments. In addition, the experimental results in a previous study by Bidmus et al.[53] using a model oil-wax system will be used as a comparison in this study. Because the solubility curve of the model oil used in the study of Bidmus et al was not provided, it was measured in the current study using differential scanning calorimetry (DSC).

4.B.1 Flow-loop Experiments with North Sea Oil A

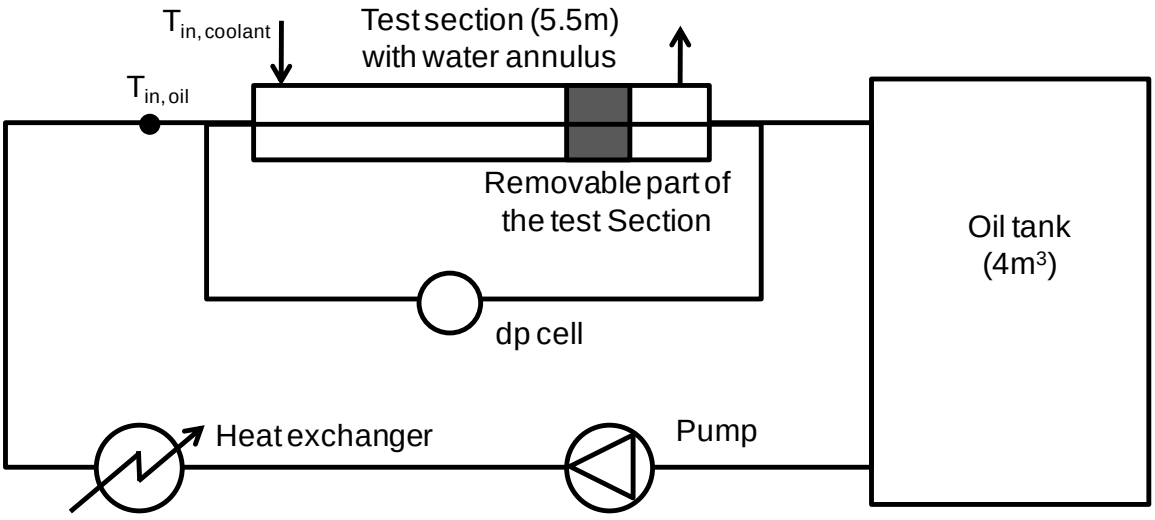

Figure 4-1: Schematic of the flow-loop experiment for wax deposition.[54]

A sketch of the flow-loop from the Herøya Research Centre of Statoil ASA is shown in Figure 4-1. The flow-loop is equipped with a oil tank of 4 m^3 and a test section with a length of 5.5 m and an inner diameter of 5.3 cm. The deposit thickness was calculated from pressure-drop measurements in the test section. The values of the calculated wax thickness were confirmed by laser measurements of the wax in the oil-deposit at the end of an experiment. The detail information of flow-loop along with the characterization techniques to study wax deposition have been reported by Hoffmann and Amundsen.[54]

4.B.2 The Solubility and Viscosity – Temperature Curves for North Sea Oil A

The North Sea Oil A used for this research has a cloud point of approximately 30ºC. The amount of precipitation of wax in the oil at various temperatures was measured using the centrifugation and gas chromatography techniques reported by Han et al. and shown in Figure 4-2.[34] The solubility curve of the North Sea Oil A is an important input parameter for wax deposition modeling. It was obtained by assuming that all the wax in the end has precipitated out of the oil at 5ºC. In this case the total wax content is the same as the precipitation of wax at 5ºC, as shown in Figure 4-2.

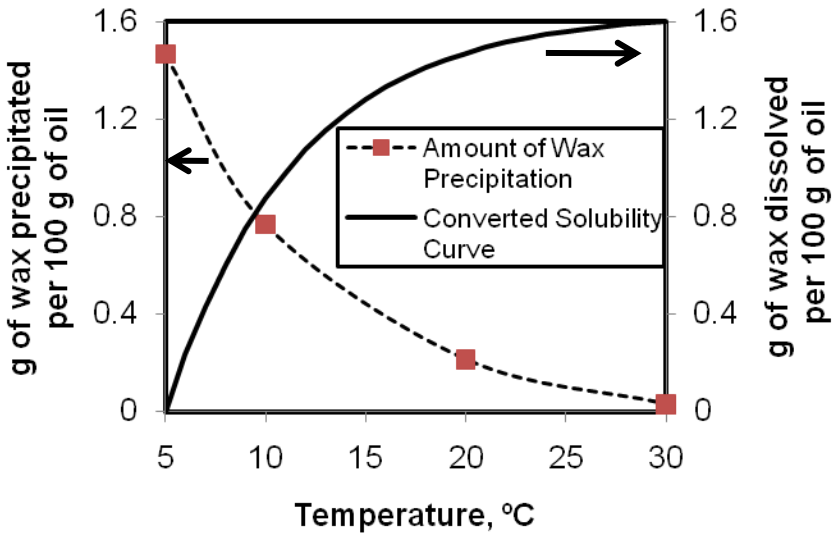

Figure 4-2: The amount of precipitation of wax in oil at various temperatures and the corresponding solubility curve for the North Sea Oil A.

In addition, the viscosity of the North Sea Oil A was measured as a function of temperature using a Physia MCR 301 Rheometer. The viscosity-temperature curve is shown in Figure 4-3.

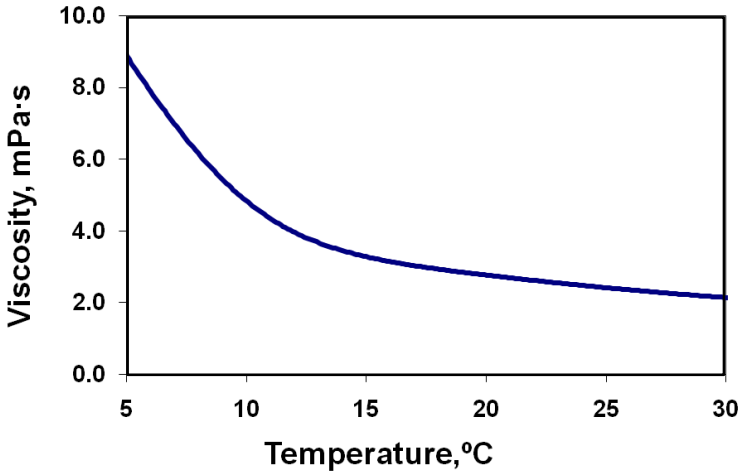

Figure 4-3: The viscosity of North Sea Oil A at different temperatures

4.B.3 The Solubility-Temperature Curve of the Model Oil in the study of Bidmus et al.[53]

A previous study by Bidmus et al. using a model oil with 6% wax content was chosen as the basis of comparison in this research. Most of the properties of this model oil can be found in the work of Bidmus et al.[53] However, the solubility of wax was not reported in their study. In order to measure this parameter, we purchased the same solvent, Norpar13 from Imperial Oil (Ontario, Canada) and the same wax sample, Parowax, from Conros Corp (Ontario, Canada) that were used by Bidmus et al. The solubility was measured with a TA® Q2000 DSC. The oil was first heated to 60 ˚C and held at this temperature for half an hour to remove any thermal history and then cooled from 60˚C to -40˚C at a rate of 1˚C/min. The solubility curve of the model oil was obtained assuming that the heat release is proportional to the amount of precipitated wax, as shown in Figure 4-4.

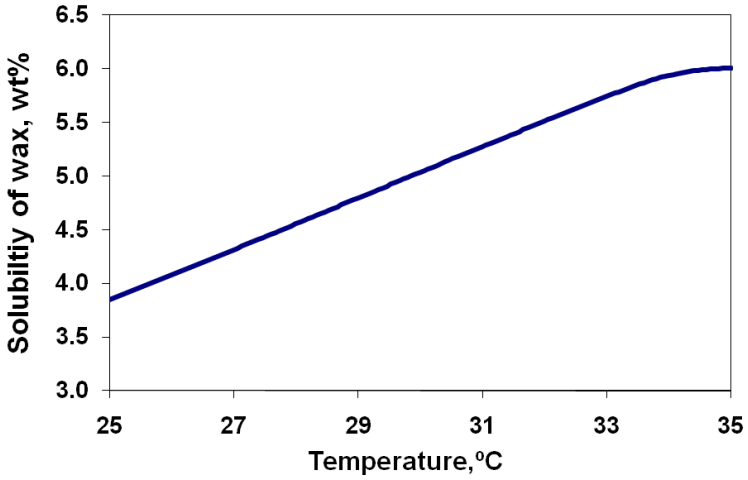

Figure 4-4: The solubility curve of wax for the model oil

Comparing Figures 2 and 4 one notes that as the oil is cooled, the solubility of the model oil is not as temperature-sensitive as the North Sea Oil A.

4.C Theoretical Analysis using The Michigan Wax Predictor (MWP)

4.C.1 Model introduction

As shown previously in Chapter 2, the Michigan Wax Predictor (MWP) was applied to investigate the temperature effects on wax deposition based on earlier studies of Singh, Lee, Huang and Fogler.[55, 16] The MWP assumes a quasi-steady for heat and mass transfer in the pipe and applies the Graetz boundary conditions at the inlet and at the wall. The external heat transfer coefficient for the coolant was calculated using the correlation by Monrad and Pelton to account for the heat loss to the coolant flowing in the annuli of the pipe.[56] The internal heat and mass transfer rates were calculated using a 2D axial symmetry energy equation and the correlation for eddy diffusivity by Van Driest.[25] The model calculates the axial convection and the radial conduction/diffusion for the heat and mass transfer equations to determine the temperature profile as well as the concentration profile of wax molecules, as shown in Figure 4-5.

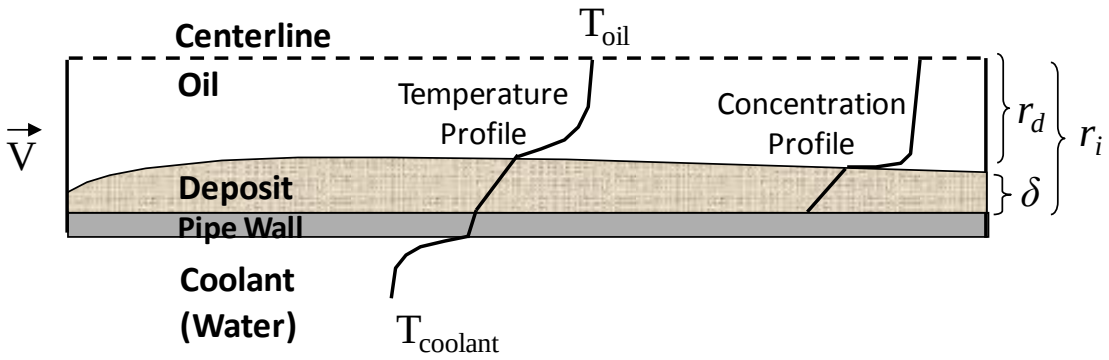

Figure 4-5: Sketch of wax deposition mechanism

With the information of the concentration profile, the concentration gradient at the interface is thereby determined to calculate the growth rate of both the deposit thickness and the wax fraction in the deposit using molecular diffusion as the major mechanism for

wax deposition. The details of this model can be found in Chapter 2 as well as in the work of Huang and Fogler.[55]

It should be noted that the equations in the model were developed from first principles and that no tuning parameters were used. In this analysis of mass transfer it is assumed that wax molecules only precipitate in the deposit and that they do not precipitate in the oil phase. This approach is similar to the one used in the laminar flow model by Singh and Fogler where the heat and mass transfer correlations were decoupled.[14] In addition, the model in the current study does not need to incorporate the so-called "shear removal" effect, i.e. the detachment of the deposited wax material from the pipe wall by the flowing oil in order to predict the observed trends. Because the effect of bulk precipitation and shear removal are highly empirical, they would require the use of tuning parameters and can reduce the reliability for our conclusions. Consequently, the major focus of this model is to examine a number of deposition experiments in general to learn if the model represents the trends shown in the experiments rather than comparing each experiment with their corresponding model predictions.

4.C.2 The determining parameter for wax deposition

To look for a more representative driving force for wax deposition than the thermal driving force, the MWP analyzes the mass balance equation shown in Equation (4.2) along with the boundary conditions shown in Equation (4.3).

$$V\frac{\partial C}{\partial z}=\frac{1}{r}\frac{\partial}{\partial r}\left[\left(\varepsilon_{\text{mass}}+D_{\text{wo}}\right)r\frac{\partial C}{\partial r}\right] \tag{4.2}$$

$$\begin{cases} \text{at z} = 0,\ C = C_{\text{inlet}} \\ \text{at r} = 0,\ \dfrac{\partial C}{\partial r} = 0 \\ \text{at r} = r_{\text{d}},\ C = C_{\text{interface}} \end{cases} \tag{4.3}$$

The following dimensionless ratios given in Equation (4.4) were used to de-dimensionalize the mass balance equation and the boundary conditions shown in Equations (4.2) and (4.3), resulting in Equations (4.5) and (4.6).

$$\left(\theta = \frac{C - C_{\text{interface}}}{C_{\text{inlet}} - C_{\text{interface}}}\right), \left(v = \frac{V}{U}\right), \left(\lambda = \frac{z}{L}\right), \left(\eta = \frac{r}{r_{\text{d}}}\right), \left(\text{Gz}_{\text{t}} = \frac{d_{\text{d}}^2 U}{L\left(\varepsilon_{\text{mass}} + D_{\text{wo}}\right)}\right) \tag{4.4}$$

$$v\frac{\partial \theta}{\partial \lambda} = \frac{1}{\eta}\frac{\partial}{\partial \eta}\left\lfloor \frac{4}{\text{Gz}_{\text{t}}}\eta\frac{\partial \theta}{\partial \eta}\right\rfloor \tag{4.5}$$

$$\begin{cases} \text{at } \lambda = 0,\ \theta = 1 \\ \text{at } \eta = 0,\ \dfrac{\partial \theta}{\partial \eta} = 0 \\ \text{at } \eta = 1,\ \theta = 0 \end{cases} \tag{4.6}$$

One notes that the solution profile of the de-dimensionalized variable θ from Equations (4.5) and (4.6) is independent of the changes in C_{inlet} and $C_{\text{interface}}$. Consequently, the radial mass flux of wax molecules from the bulk towards the interface can be found to be proportional to $\{[D_{\text{wo, interface}}\cdot(C_{\text{inlet}} - C_{\text{interface}})]/r_{\text{d}}\}$, as given by Equation (4.7).

$$D_{\text{wo, interface}}\left.\frac{dC}{dr}\right|_{\text{interface}} = D_{\text{wo, interface}}\frac{\partial C}{\partial \theta}\cdot\left(\left.\frac{\partial \theta}{\partial r}\right|_{\text{interface}}\right) = \frac{D_{\text{wo, interface}}\left(C_{\text{inlet}} - C_{\text{interface}}\right)}{r_{\text{d}}}\left(\left.\frac{\partial \theta}{\partial \eta}\right|_{\text{interface}}\right) \tag{4.7}$$

The impact of temperature on the concentration differences, $(C_{\text{inlet}} - C_{\text{interface}})$ can be seen by assuming thermodynamic equilibrium for the concentrations based on the solubility curve of the oil in a form of a mass flux, as given in Equation (4.8).

$$J_{\text{wax}} = \frac{D_{\text{wo, interface}}\left(C_{\text{inlet}} - C_{\text{interface}}\right)}{r_{\text{d}}} \approx \frac{D_{\text{wo, interface}}\left\lfloor C_{\text{inlet}}\left(\text{eq}\right) - C_{\text{interface}}\left(\text{eq}\right)\right\rfloor}{r_{\text{d}}} \tag{4.8}$$

In addition, the effect of the temperature on the diffusivity can be estimated using the Hayduk-Minhas correlation as shown in Equation (4.9).[31]

$$D_{\text{wo,interface}} = 13.3\times10^{-12}\,\frac{T_{\text{interface}}^{\,1.47}\,\mu^{(10.2/V_{\text{A}}-0.791)}}{V_{\text{A}}^{\,0.71}}\ \text{m}^2/\text{s} \tag{4.9}$$

Difficulties arise when one tries to evaluate $D_{\text{wo, interface}}$ and $C_{\text{interface}}$(eq) because they depend on the interface temperature, $T_{\text{interface}}$ which in turn greatly depends on the predicted value of an existing deposit thickness. Therefore one needs to know the exact thickness of the deposit in order to accurately determine $C_{\text{interface}}$(eq) and $D_{\text{wo, interface}}$. This hurdle can be resolved by evaluating the values of $D_{\text{wo, interface}}$ and $C_{\text{interface}}$(eq) initially (at t=0) when deposition has not yet occurred. In this case $C_{\text{interface}}$(eq) simply reduces to C_{wall}(eq), $D_{\text{wo, interface}}$ reduces to $D_{\text{wo, wall}}$ and r_{d} reduces to r_{i}. Because the wall temperature, T_{wall}, can be accurately determined by solving the heat transfer equation in the MWP using well established correlations for the eddy diffusivities,[25] C_{wall}(eq) can be obtained from T_{wall} knowing the solubility curve of the oil and $D_{\text{wo, wall}}$ can be determined through T_{wall} using the Hayduk-Minhas correlation.[31] It should be noted that in most of the lab-scale flow-loop studies, no significant axial variations in the bulk concentration were observed for the parameters due to the short length of the pipe. Therefore C_{inlet}(eq) is referred to as C_{oil}(eq) for subsequent quantitative analyses.

The significance of the above analysis is that the impact of the oil/coolant temperatures on wax deposition can be found by investigating its effect on a parameter that has the unit of a mass flux, as shown in Equation (4.10).

$$J_{\text{wax}}\left(t=0^{+}\right) = \frac{D_{\text{wo, wall}}\left(C_{\text{inlet}} - C_{\text{wall}}\right)}{r_i} \tag{4.10}$$

Consequently, J_{wax} is referred to as the characteristic mass flux for wax deposition. The difference in the concentrations [C_{oil}(eq) – C_{wall}(eq)] is referred to as the mass driving force in comparison of the thermal driving force (T_{oil} – $T_{coolant}$) among several deposition studies.[50,52,53] We will show that this mass driving force is the most dominant parameter to affect the behavior of the characteristic mass flux for wax deposition, J_{wax} when the oil/coolant temperatures are changed.

4.D Results and Discussions

4.D.1 Flow-loop results and the prediction of the experimental trends by the model

Several experimental studies have found that the amount of deposit decreases with decreasing thermal driving force.[50,52,53] However, Figure 4-6 and Figure 4-7 show the experimental and theoretical trajectories of wax thickness as a function of time for different operating temperature conditions. The experiments carried out in the current study have shown the two following opposing trends:

Trend (1) (Figure 4-6): Reduced deposition with increasing oil temperature, T_{oil}, i.e. *increasing thermal driving force,* (T_{oil} - $T_{coolant}$).

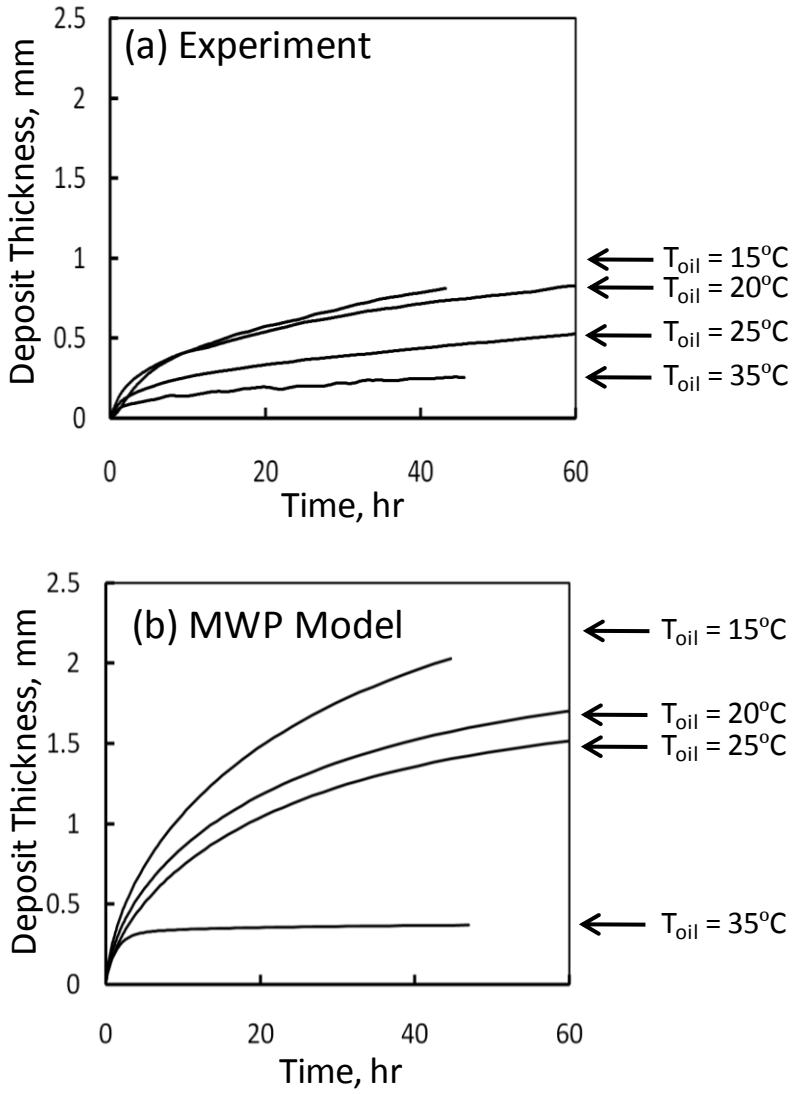

Figure 4-6: Comparison of deposit thickness as a function of oil temperature, T_{oil} between (a) the experimental results and (b) the model prediction by the MWP. The oil flow rate, Q_{oil}, was maintained constant at 20m^3/h and the coolant temperature, $T_{coolant}$, was maintained constant at 5ºC.

Trend (2) (Figure 4-7): Reduced deposition with increasing coolant temperature, $T_{coolant}$, i.e. *decreasing thermal driving force*, (T_{oil} - $T_{coolant}$).

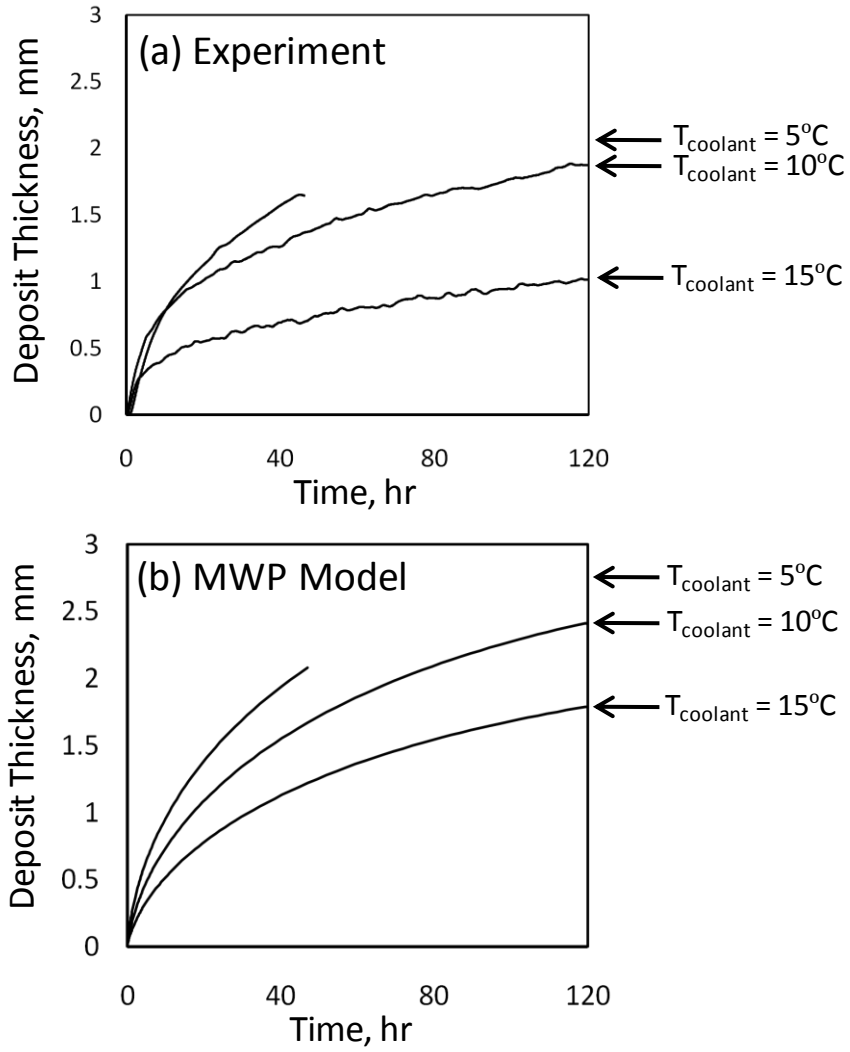

Figure 4-7: Comparison of deposit thickness as a function of coolant temperature, $T_{coolant}$, between (a) the experimental results and (b) the model prediction by the MWP. The oil flow rate, Q_{oil}, was maintained constant at 5m^3/h and the oil temperature, T_{oil}, was maintained constant at 20°C.

These two opposing trends indicate that the thermal driving force is not the best candidate for a theoretical analysis of wax deposition and other factors exists that better explain the change of wax deposition at different oil temperatures. Because of the agreement of the trends between the experiments and the predictions by the MWP Figure 4-6 and Figure 4-7, the MWP will be used to analyze the results shown in this study. In particular, the variations of the parameters in the characteristic mass flux for

wax deposition, J_{wax} for the experiments with different oil/coolant temperatures will be investigated. The parameters consist of the diffusivity, $D_{wo,\ wall}$ and the mass driving force, $[C_{oil}(eq) - C_{wall}(eq)]$.

4.D.2 Analysis for the Reduced Deposition with Increasing Oil Temperature

Table 4-1 summarizes the characteristic mass flux for wax deposition, J_{wax} and its corresponding parameters for the experiments where the oil temperature, T_{oil} was varied and the coolant temperature, $T_{coolant}$ was kept constant. In these experiments, the deposition thickness decreased as the oil temperature increases as shown in Figure 4-6.

Table 4-1: Comparison of the parameters for the characteristic mass flux for wax deposition, J_{wax} among the deposition experiments with different T_{oil} while Q_{oil} and $T_{coolant}$ are maintained constant.

Parameters	**Value**			
T_{oil}, ^{0}C	15.3	20.3	25.3	35.4
$T_{coolant}$, ^{0}C	5.0			
Q_{oil}, m^3/h	20.0			
T_{wall}, ^{0}C	9.5	12.0	14.7	20.5
$D_{wo,wall} \times 10^{10}$, m^2/s	2.11	2.49	2.89	3.64
C_{oil}(eq), wt%	1.09	1.26	1.34	1.44
C_{wall}(eq), wt%	0.65	0.89	1.07	1.26
C_{oil}(eq) - C_{wall}(eq), wt%	0.45	0.36	0.27	0.17
$J_{wax} \times 10^{10}$, m/s·wt%	36.17	34.14	29.73	23.57

One observes that the increase in T_{oil} leads to an increase in T_{wall}, which in turn has several effects on the characteristic mass flux for wax deposition, J_{wax}. First, the diffusivity of wax in oil at the wall, $D_{wo,\ wall}$ increases, which tends to increase the mass flux. Secondly, the changes in T_{oil} and T_{wall} causes the increases in both C_{oil}(eq) and C_{wall}(eq). Although the change in T_{oil} from 15.3ºC up to 35.4ºC (a change of 20.1ºC) exceeded the change in T_{wall} from 9.5ºC up to 20.5ºC (a change of 11ºC), the change in

C_{oil}(eq) from 1.09% to 1.44% (a change of 35%) was less than the change in C_{wall}(eq) from 0.65% up to 1.26% (a change of 190%). Therefore, the mass driving force, [C_{oil} (eq) – C_{wall} (eq)] decreases as the T_{oil} increases and outweighs the increase in $D_{wo,\ wall}$, resulting in a decrease in the characteristic mass flux for wax deposition, J_{wax}, as can be seen in the last row of Table 4-1. This decrease in the mass flux for wax deposition explains the reduced deposit thickness for the experiments with increasing oil temperatures as shown in Figure 4-6. It should be noted that the difference in the amount of change in the equilibrium concentrations at different temperatures (T_{oil} and T_{wall}) reflects the effect of the concave shape of the solubility curve (Figure 4-2) where its gradient decreases as temperature increases.

4.D.3 Analysis for the Reduced Deposition with Increasing Coolant Temperature

Now consider the other parameter variation where $T_{coolant}$ was varied and T_{oil} was kept constant. For these operating conditions it was found that the experimental wax thickness decreased as $T_{coolant}$ increased (Figure 4-7). The characteristic mass flux for wax deposition, J_{wax} and its corresponding parameters are shown in Table 4-2.

Table 4-2: Comparison of the parameters for the characteristic mass flux for wax deposition, J_{wax} among deposition experiments with different coolant temperatures while Q_{oil} and T_{oil} are maintained constant.

Parameters	**Value**		
T_{oil}, ^{0}C	20.2		
$T_{coolant}$, ^{0}C	5.0	10.0	15.0
Q_{oil}, m^3/h	5.0		
T_{wall}, ^{0}C	8.1	12.1	16.1
$D_{wo,\ wall}$ ×10^{10}, m^2/s	1.93	2.44	2.97
C_{oil} (eq), wt%	1.26	1.26	1.26
C_{wall} (eq), wt%	0.48	0.89	1.13
C_{oil} (eq) - C_{wall} (eq), wt%	0.78	0.37	0.13

J_{wax} ×10^{10}, m^2/s·wt%	57.35	34.39	14.71

It can be seen from Table 4-2 that the increase in $T_{coolant}$ leads to the increase in T_{wall}, which increased the values of both D_{wo} and C_{wall} (eq). The increase in D_{wo} tends to increase the characteristic mass flux for wax deposition, J_{wax}. However, the increase in C_{wall} (eq) from 0.48% to 1.13% has caused significant decrease in the mass driving force [C_{oil} (eq) - C_{wall} (eq)] from 0.78% to 0.13%. This decrease in the mass driving force overcomes the increase in the diffusivity, leading to a decrease in the the characteristic mass flux for wax deposition with increasing $T_{coolant}$, as is shown in the last row of Table 4-2. This decrease in the mass flux explains the reduced experimental deposit thickness as shown in Figure 4-7.

4.D.4 Analysis of previous studies

The increase or decrease in the amount of wax deposit with the change in the temperature conditions can be attributed to the shape of the solubility curve, which causes the equilibrium concentration to behave differently in the bulk oil than at the wall. In order to further verify this result, the previous study on wax deposition by Bidmus et al[53] was analyzed. Figure 4-8 shows the experimental trends from the study of Bidmus et al.[53] It can be seen that as T_{oil} increases the amount of deposit increases, which at first appears to be contradictory to the trend in our study as shown in Figure 4-6. However, when we applies the analysis on the characteristic mass flux for wax deposition, the results are entirely consistent.

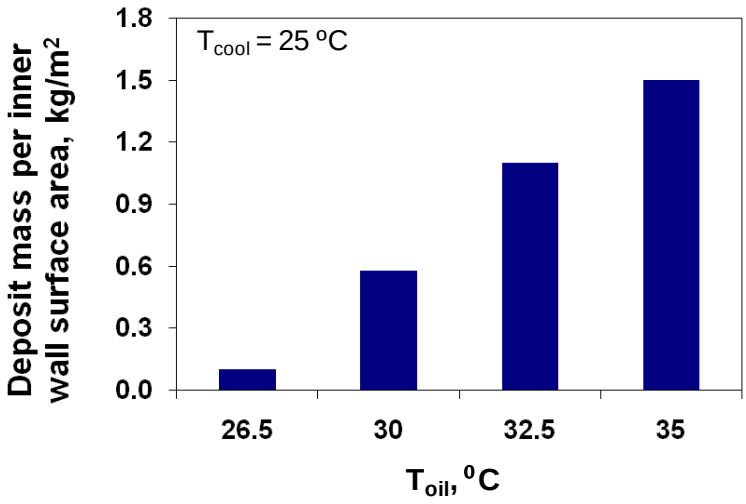

Figure 4-8: Comparison of the amount of deposit between experiments with different oil temperatures for the study of Bidmus et al.[53]

The parameters for the mass flux were calculated and shown in Table 4-3 based on the geometry of the flow-loop and operating conditions reported in their study.

Table 4-3 Comparison of the parameters for the characteristic mass flux for wax deposition, J_{wax} among deposition experiments with different T_{oil} while Q_{oil} and $T_{coolant}$ are maintained constant in the study of Bidmus et al using a model oil.

Parameters	**Value**			
T_{oil}, ^{0}C	26.5	29.0	33.0	35.0
$T_{coolant}$, ^{0}C	25.0			
Q_{oil}, m^3/h	0.4			
T_{wall}, ^{0}C	25.4	25.9	27.1	28.0
$D_{wo,\ wall} \times 10^{10}$, m^2/s	2.81	2.94	3.27	3.53
C_{oil} (eq), wt%	4.19	4.80	5.74	6.00
C_{wall} (eq), wt%	3.94	4.05	4.34	4.55
C_{oil} (eq) - C_{wall} (eq), wt%	0.25	0.75	1.40	1.45
$J_{wax} \times 10^{10}$, m^2/s·wt%	27.66	86.81	180.24	201.5157

It can be seen that the increases of T_{oil} from 26.5ºC to 35ºC had two effects on increasing the mass flux. First, a increase in D_{wo} was observed, which tends to increase the characteristic mass flux for wax deposition, J_{wax}. Secondly, both C_{oil} (eq) and C_{wall} (eq) increased as a result of increased T_{oil} and T_{wall}. More importantly, the increase in C_{oil} from

4.19% to to 6.00% is greater than the increase in C_{wall} from 3.94% to 4.55%, which results in the increase in the mass driving force, [C_{oil} (eq) - C_{wall} (eq)]. The combination of the increases in the diffusivity and in the mass driving force results in the increase in the mass flux with increasing T_{oil}, which explains the experimental trends observed Figure 4-8 where the amount of deposition increases with increasing T_{oil}.

The importance in the solubility curve to affect the driving force for wax deposition can be seen by comparing experiments in this study (Figure 4-6 and Table 4-1) and that in the study of Bidmus et al (Figure 4-8 and Table 4-3).[53] The changes in T_{oil}, T_{wall}, C_{oil} (eq) and C_{wall} (eq) for the two studies when T_{oil} was varied are shown in Table 4-4.

Table 4-4: Comparison of the changes in T_{oil}, T_{wall}, C_{oil}(eq) and C_{wall}(eq) for the experiments with both the North Sea Oil A and the Model oil where T_{oil} was varied. The numbers are calculated from Tables 5 and 7.

	North Sea Oil A	Model Oil
Change in $T_{oil,}$ ºC	15.3 - 35.4	26.5 - 35.0
$\Delta T_{oil,}$ ºC	20.1	8.5
$\Delta T_{wall,}$ ºC	11.0	2.6
$\Delta T_{oil} > \Delta T_{wall}$	Yes	Yes
ΔC_{oil} (eq), wt%	0.35	1.81
ΔC_{wall} (eq), wt%	0.61	0.61
ΔC_{oil} (eq) > ΔC_{wall} (eq)	No	Yes

One finds that for both sets of the experiments the increase in T_{oil} has caused the increase in T_{wall}. The changes in T_{wall} were less significant than that in T_{oil} for both studies. The major difference is that for the model oil, the gradient of its solubility curve (Figure 4-4) is virtually constant (the solubility curve is close to a straight line) so that the changes in C_{oil}(eq) and C_{wall}(eq) simply reflected the changes in T_{oil} and T_{wall}. These changes eventually lead to an increase in the mass driving force, [C_{oil} (eq) - C_{wall} (eq)] and the characteristic mass flux for wax deposition, J_{wax} for the model oil when T_{oil}

increased. However, the gradient of the solubility curve for the North Sea Oil A decreased with increasing temperature (a concave solubility curve as shown in Figure 4-2), resulting in the changes in C_{oil}(eq) and C_{wall}(eq) to deviate from those from in T_{oil} and T_{wall}. Eventually the change in C_{wall}(eq) outweighs that in C_{oil}(eq) thereby resulting in the increase of the driving force for the North Sea oil A. This finding further demonstrates the advantage of using the mass driving force in comparison of the thermal driving force as it includes the impact of the solubility curve on wax deposition.

4.D.5 The guidelines to determine the effect of oil/coolant temperatures

Based on the analysis above, we have summarized the algorithm to indentify the change of the amount of wax deposition with changes in the oil/coolant temperatures as follows:

Step (1): Calculate the wall temperature at the beginning of the experiment where no wax deposit has yet formed on the wall. This can be done by either solving the heat transfer equation numerically or via the correlations that account for the heat transfer coefficients for the oil and the coolant.[56,27]

Step (2): Calculate the diffusivity of the wax in the oil at the wall temperature, $D_{wo,\ wall}$.

Step (3): Based on the solubility curve of the oil, calculate the equilibrium concentrations in the bulk and at the wall C_{oil}(eq) and C_{wall}(eq) and thus the mass driving force [C_{oil}(eq) - C_{wall}(eq)].

Step (4): Calculate $\{D_{wo,\ wall} \cdot [C_{oil}(eq) - C_{wall}(eq)]/r_i\}$ and compare this parameter for experiments where the oil or the coolant temperatures are varied. The experiments with higher mass driving force should have a greater increase rate of deposit thickness.

4.D.6 Comparison between the Carbon Number Distribution of the Model Oil and the North Sea Oil A

The above comparison has highlighted the importance of the shape of the solubility curve on the effects of the oil/coolant temperatures on wax deposition. The solubility of wax represents the multi-component solid-liquid equilibrium of the oil, which strongly depends on its carbon number distribution. Figure 4-9 (a) shows the carbon number distributions of the C20+ components in the model oil used in Bidmus et al.[53] while Figure 4-9 (b) shows the distribution for the North Sea Oil A used in this study. Two major differences can be observed between these two oils. First, a longer tail can be seen in the carbon number distribution of North Sea Oil A, indicating the existence of heavy paraffins (C50-C80), which is not existent in the model oil. In addition, lighter components (C20 to C26) account for 41% of the wax in North Sea Oil A, while they only account for 26% of the wax in the model oil. The small amount of the heavy components and the excess amount of the light components in North Sea Oil A causes a greater precipitation of wax at lower temperatures compared to the model oil. This greater precipitation is consistent with the concave shape of the solubility curve of the North Sea Oil A at low temperatures and eventually explains the contradictory observed trends of growth of deposit thickness between Figures10 and 12.

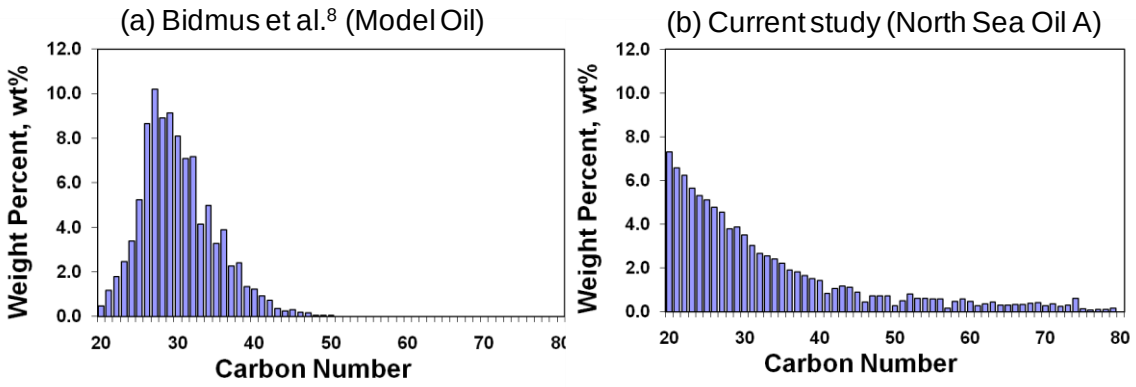

Figure 4-9**:** Carbon number distribution of the heavy components in (a) the model oil and (b) the North Sea Oil A

4.E Conclusions

In this study an analysis was carried out using the Michigan Wax Predictor (MWP) to establish guidelines to determine the effect of the oil and the coolant temperatures on wax deposition thickness. The MWP was first applied to a series of flow loop deposition experiments in which the oil temperature and the coolant temperature were all changed independently. It is found that the MWP successfully has predicted the effects of the operating conditions on wax deposition for North Sea Oil A without using any adjustable parameters. These effects include reduced deposition with increasing oil temperature and with increasing coolant temperature.

The consistency between the MWP predictions and the experimental trends shows that the MWP has captured the most important physics for wax deposition. In the analysis using the MWP, the effect of the oil/coolant temperatures on wax deposition is seen in their impact on the mass flux term, $\{D_{wo,\ wall} \cdot [C_{oil}\,(eq) - C_{wall}\,(eq)]/r_i\}$ (Equation (4.8)), which includes the diffusivity $\underline{D}_{wo,\ wall}$ and the mass driving force, $[C_{oil}\,(eq) - C_{wall}\,(eq)]$. The mass driving force for wax deposition is a more appropriate parameter to quantify

the temperature effects on wax deposition in comparison to the thermal driving force [$\Delta T = (T_{oil} - T_{coolant})$]. [50,52,53]

It is found that the shape of the solubility curve can greatly vary the behavior of the mass driving force by affecting the equilibrium concentrations of wax in the bulk oil and at the wall. The analysis is carried out by investigating the contradictory change in the deposit thickness between experiments using a North Sea Oil A and those using a model oil-wax solution. It was found that for the North Sea Oil A the amount of wax deposit decreases when the oil temperature increases, which is a trend that has not been observed in the study of the model oil-wax solution. By analyzing the parameters involved with the mass flux, $\{D_{wo,\ wall} \cdot [C_{oil}\ (eq) - C_{wall}\ (eq)]/r_i\}$, it is found that the difference in shape of the solubility curves between these two oils can be used to explain the difference in their experimental trends. The concave shape of the solubility curve of the North Sea Oil A results in a more drastic change in $C_{wall}(eq)$ compared to $C_{oil}(eq)$, while the linear shape of the solubility curve for the model oil-wax solution leads to a less significant change in $C_{wall}\ (eq)$ in comparison to $C_{oil}(eq)$. This difference in the changes in the equilibrium concentrations leads to the difference in the behavior of the mass driving force, which eventually explains the opposing trends in the amount of wax deposit observed in the their experiments when the oil temperature is varied. Furthermore, this discrepancy in these two oils' solubility curves is a result of the difference in their carbon number distributions. It should be noted that using model oils in the investigation of wax deposition can lead to misleading conclusions that are significantly different from those seen in the real crude oils.

Chapter 5

Wax Deposition Modeling of Oil/Water Stratified Channel Flow

5.A Introduction

As off shore drilling becomes increasingly important in the petroleum industry, water is commonly seen in the subsea pipelines.[58-59] In wax deposition modeling, knowledge of the hydrodynamics and heat/mass transfer are the major problems in two-phase flow because a variety of flow patterns can exist. Each pattern has its own unique transport phenomena. A typical flow map of a liquid/liquid two-phase flow is shown in Figure 5-1[57].

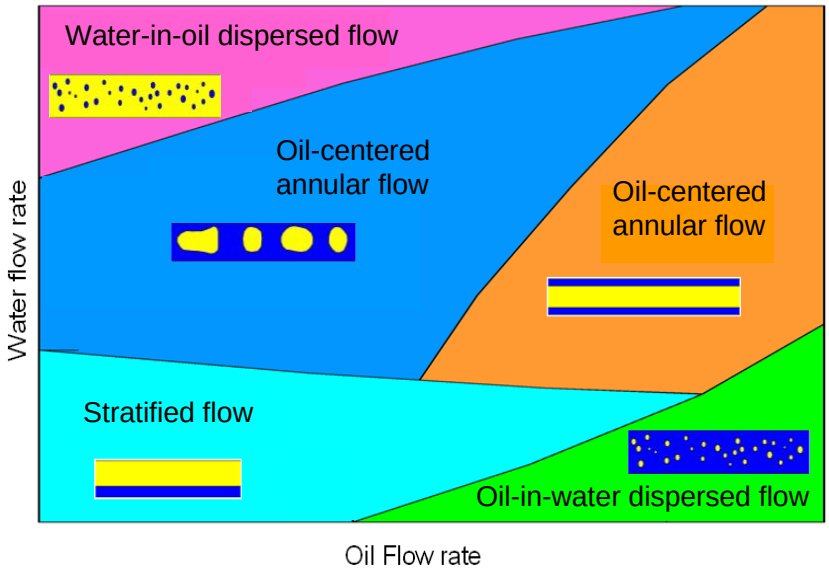

Figure 5-1: A flow map of oil/water two-phase flow by Shi et. al.[57]

Wax deposition in oil-centered annular flow would rarely occur because oil is not in contact with the pipe. Studies of intermittent (slug) flow are highly empirical because of the instability of the slugs and the difficulty to identify an averaged slug length and slug frequency.[58] For dispersed flow, the single-phase wax deposition mechanism may be difficult to modify and apply because of emulsions and phase inversion. Oil/water stratified flow will be included in this research because of its frequent occurrence in pipeline transportation[59] and because of its tractability. Additionally, the oil phase has a relatively large contact area with the pipe wall, allowing deposition to occur.

Although heat and mass transfer correlations are well established for single-phase models, they are not as reliable for multiphase models. The first attempt to study multiphase wax deposition was for gas/oil two-phase flow[60]. The heat transfer correlations were provided by Kim et. al.[61] However, none of the 20 gas/liquid correlations used in this study were able to predict the experimental deposit thickness. To try to remedy this problem, several material properties, such as the thermal conductivity of oil and the diffusivity of wax in oil were "tuned" unrealistically without any convincing physical explanations and without being able to be extended to other experiments or systems.

Recent advances in computational fluid dynamics have made it possible to calculate multiphase transport phenomena without the use of correlations. However, little research on multiphase wax deposition using CFD has been undertaken because of the computational intensity required. In order to model multiphase wax deposition, non-isothermal hydrodynamics and transport phenomena need to be calculated among three phases (oil, water and deposit). As the deposit grows in the pipe wall, the oil/water

interface and oil/deposit interface are two moving boundaries that need to be updated in each time step. For oil/water stratified flow, the complexity in geometry provides great difficulty in 3D modeling. Consequently, to gain a qualitative understanding and insight of wax deposition in multiphase flow, a 2D model is established using a unidirectional flow to study wax deposition in oil/water stratified flow. The decrease in dimensions and the unidirectional flow assumption reduce the computational intensity and provide insight on how water influences wax deposition in oil/water stratified flow.

5.B Mathematical Model Development

5.B.1 Hydrodynamics in non-isothermal conditions

Numerous studies on the hydrodynamics of stratified flow have been carried out, many focusing on calculating the velocity distribution, the stress at the wall/interface and the predicting phase volume fraction.[59,62] Many of these studies are based on simplifying assumptions, most notably that the interface position and velocity profile are independent of axial distance. For the system shown in Figure 5-2, the hydrodynamics is based on the analytical solution of the Navier-Stokes equation for laminar flows of two immiscible fluids between two parallel plates, as given in Equations (5.1) - (5.3).[63]

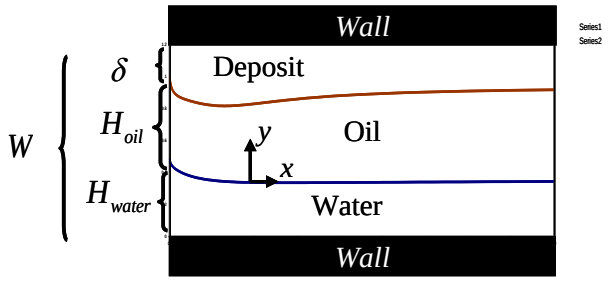

Figure 5-2: A sketch of Hydrodynamics of oil/water stratified flow

$$V_{\text{oil}}(y)=\left\{u_{\text{water}}\left[1-\frac{u_{\text{oil}}}{u_{\text{water}}}\left(\frac{y}{H_{\text{oil}}}\right)^2\right]+\left(\frac{u_{\text{oil}}-u_{\text{water}}}{1+K}\right)\left[1+K\left(\frac{y}{H_{\text{oil}}}\right)\right]\right\}\frac{dP}{dx} \tag{5.1}$$

$$V_{\text{water}}(y)=\left\{u_{\text{water}}\left[1-\left(\frac{y}{H_{\text{water}}}\right)^2\right]+\left(\frac{u_{\text{oil}}-u_{\text{water}}}{1+K}\right)\left[1+\left(\frac{y}{H_{\text{water}}}\right)\right]\right\}\frac{dP}{dx} \tag{5.2}$$

$$H_{\text{oil}}+H_{\text{water}}+\delta=W \tag{5.3}$$

with K, u_{oil} and u_{water} given by Equations (5.4).

$$K=\frac{\mu_{\text{water}}}{\mu_{\text{oil}}}\frac{H_{\text{oil}}}{H_{\text{water}}},u_{\text{oil}}=-\frac{H_{\text{oil}}^2}{2\mu_{\text{oil}}},u_{\text{water}}=-\frac{H_{\text{water}}^2}{2\mu_{\text{water}}} \tag{5.4}$$

From the equations above, it is seen that the velocity profile of water/oil stratified channel flow is dependent on the viscosity of oil and water, μ_{o} and μ_{w}, the height of both phases, H_{o} and H_{w}, as well as the pressure-drop, $\frac{dP}{dx}$. Intuitively, one can simply input the values of those parameters to calculate the velocity profile. However, this procedure is invalid for non-isothermal conditions. As the temperature of the fluids decreases along the channel, the viscosities of both water and oil increase. This increase in the viscosities leads to the increase of the pressure-drop, $\frac{dP}{dx}$ along the channel. More importantly, the viscosity of oil increases more rapidly than water, causing an increase in the viscosity ratio of oil/water. According to Equations (5.1)and (5.2), this increase leads to the decrease in the velocity of oil and the increase of velocity of water. To maintain the flow rates of each phase to be constant, a non-zero velocity in the direction perpendicular to the flow direction occurs, which leads to a change of oil/water interface position. A sketch of this change in hydrodynamics is shown in Figure 5-3. If one directly input the constant value of the pressure-drop and the heights of both phases to calculate the

velocity profile, the flow rate of both oil and water is not conserved and the mass balance is violated.

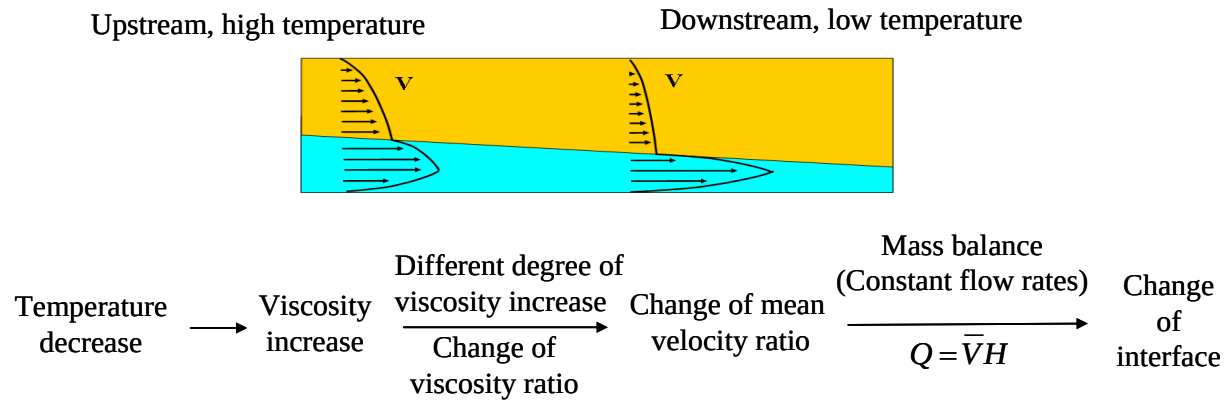

Figure 5-3: Sketch of non-isothermal velocity profile of oil/water stratified flow

To mathematically account for the change in hydrodynamics in non-isothermal flow conditions, the viscosity of oil and water at a particular axial location are assumed to be dependent on the temperature of each phase. Due to the insulation installed onto the subsea pipelines, the effect of the radial difference in the viscosity on the velocity profile caused by the change of temperature in the radial direction is neglected. The bulk temperatures of both phases are used to calculate the viscosities at a particular axial location, as given by Equations (5.5)

$$\mu_{\text{oil}} = \mu_{\text{oil}}(T_{\text{b,oil}}),\ \mu_{\text{water}} = \mu_{\text{water}}(T_{\text{b,water}}) \tag{5.5}$$

In order to account for the conservation of the mass flow rate, the pressure-drop, $\frac{dP}{dx}$ as well as the height of oil and water, H_o and H_w along the channel must be calculated instead of taken as inputs. The calculation consists of three steps:

1) The flow rate of each phase is obtained by integrating the velocity of both oil and water (Equations (5.6) and (5.7)):

$$Q_{\text{oil}} = \left[u_{\text{water}} - \frac{u_{\text{oil}}}{3} + \frac{u_{\text{oil}} - u_{\text{water}}}{1+K}\left(1+\frac{K}{2}\right) \right] H_{\text{oil}} \frac{dP}{dx} \tag{5.6}$$

$$Q_{\text{water}} = \left[\frac{2}{3} u_{\text{water}} + \frac{u_{\text{oil}} - u_{\text{water}}}{2(1+K)} \right] H_{\text{water}} \frac{dP}{dx} \tag{5.7}$$

To determine the height of the interface, the ratio of Equations (5.6) and (5.7) are used to obtain the height ratio as a function of the flow rate ratio and the viscosity ratio of the two phases:

$$\frac{H_{\text{ow}}^4}{\mu_{\text{ow}}^2} + 4\frac{H_{\text{ow}}^3}{\mu_{\text{ow}}} + 3\frac{(1-Q_{\text{ow}})}{\mu_{\text{ow}}} H_{\text{ow}}^2 - 4\frac{Q_{\text{ow}}}{\mu_{\text{ow}}} H_{\text{ow}} - Q_{\text{ow}} = 0 \tag{5.8}$$

where

$$Q_{\text{ow}} = \frac{Q_{\text{oil}}}{Q_{\text{water}}}, H_{\text{ow}} = \frac{H_{\text{oil}}}{H_{\text{water}}}, \mu_{\text{ow}} = \frac{\mu_{\text{oil}}}{\mu_{\text{water}}} \tag{5.9}$$

At a particular axial location for known viscosity and flow rate ratios, the height of each phase, H_{o} and H_{w} can be obtained by solving Equations (5.8) and (5.3) simultaneously.

2) The pressure-drop, $\frac{dP}{dx}$ at that location can be solved from either Equation (5.6) or (5.7), both of which lead to the same values.

3) The velocity profile in Equations (5.1) and (5.2) can be readily determined by the viscosity ratio, the height of each phase and the pressure-drop as previously calculated. The overall algorithm for the calculation is shown in Figure 5-4.

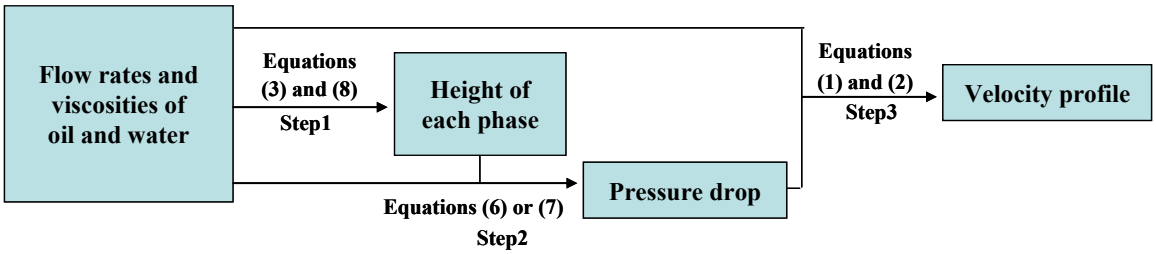

Figure 5-4: The algorithm to calculate the velocity profile under non-isothermal conditions

5.B.2 Heat and Mass transfer

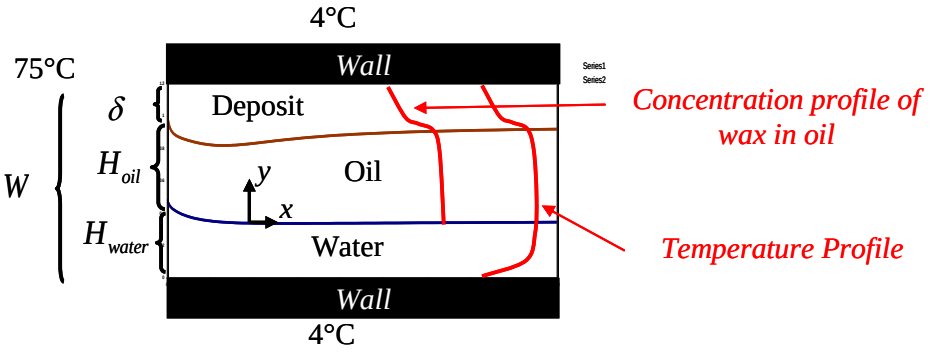

Figure 5-5: A sketch of wax deposition in oil/water laminar stratified channel flow.

The temperature profile, shown as a sketch in Figure 5-5, is calculated by the Equation (5.10) assuming quasi-steady state in which axial conduction is neglected[63]

$$\rho C_p V_x(y)\frac{\partial T}{\partial x}=\frac{\partial}{\partial y}\left(k\frac{\partial T}{\partial y}\right) \tag{5.10}$$

The thermal boundary condition assumes continuous heat fluxes at the walls with a constant external heat transfer coefficient accounting for the thermal resistance of the insulation material and the surrounding sea, as shown in Equations (5.11).

$$\begin{cases} y=-H_{\text{water}}, -k_{\text{water}}\dfrac{\partial T}{\partial y}=h\left(T_{\text{wall}}-T_{\text{amb}}\right) \\ y=H_{\text{oil}}, -k_{\text{dep}}\dfrac{\partial T}{\partial y}=h\left(T_{\text{amb}}-T_{\text{wall}}\right) \end{cases} \tag{5.11}$$

The governing equation for mass transfer in which axial diffusion is neglected[63] is given by Equation (5.12). The precipitation of wax molecules in the bulk oil is neglected, which is valid in laminar flow.[14]

$$V_x(y)\frac{\partial C}{\partial x} = \frac{\partial}{\partial y}\left(D_{wo}\frac{\partial C}{\partial y}\right) \tag{5.12}$$

The impermeable boundary condition at the oil/water interface is imposed, assuming wax molecules do not dissolve in the water phase. For the deposit phase, it is assumed that the wax concentration obeys liquid/solid equilibrium, shown in Equation (5.13). A simple implicit scheme is used to solve the above equations.[27]

$$\begin{cases} y < 0,\ C = 0 \\ y = 0,\ \dfrac{\partial C}{\partial y} = 0 \\ H_{\text{oil}} < y < (H_{\text{oil}} + \delta),\ C = f_{\text{solubility}}(T) \end{cases} \tag{5.13}$$

5.B.3 Deposition Mechanism

Because molecular diffusion is the deposition mechanism, the mass flux from the oil-deposit interface into the gel is responsible for the increase of the wax fraction in the deposit as a function of time as given in Equation (5.14)..[14]

$$\delta\rho_{\text{deposit}}\frac{d\overline{F}_{\text{w}}(t)}{dt} = J_{\text{from interface to deposit}} = -D_{eff}\left.\frac{\partial C}{\partial y}\right|_{\text{from interface to deposit}} \tag{5.14}$$

The difference between the mass flux from the bulk oil to at the oil-deposit interface and the mass flux from the interface into the deposit represents the growth of the deposit thickness as given by Equation (5.15).

$$\overline{F}_{\mathrm{w}}(t)\,\rho_{\mathrm{deposit}}\frac{d\delta}{dt} = J_{\text{from bulk oil to interface}} - J_{\text{from interface to deposit}}$$
$$= \left(-D_{wo}\left.\frac{\partial C}{\partial y}\right|_{\text{from bulk oil to interface}}\right) - \left(-D_{eff}\left.\frac{\partial C}{\partial y}\right|_{\text{from interface to deposit}}\right) \tag{5.15}$$

5.B.4 Simulation Conditions

Taking similar length scales to field scale subsea pipelines, the width between the plates is 0.3m. The overall external coefficient, including the insulation material and the sea, is 1W/(m^2/K). The inlet temperature is 74°C and the surrounding temperature is 4°C, which are typical conditions seen in the field. The properties of the oil are listed in Table 5-1 and Figure 5-6.

Table 5-1: The properties of the oil in this study

Cloud Point, °C	40
Specific Heat, J/K/kg	2500
Density, kg/m^3	840
Thermal conductivity W/m/K	0.14

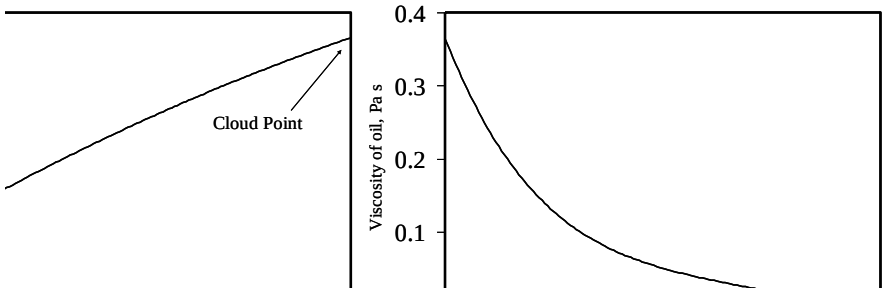

Figure 5-6: Solubility of the wax in the oil and viscosity of the oil in this study.

Six simulations are carried out in this study. The oil and water flow rates for these cases are shown in Table 5-2.

Table 5-2: The flow rates and inlet Reynolds numbers of oil and water in the simulations

Case Number	Flow Rate Ratio Water/Oil	Oil Flow Rate m^2/s	Oil Inlet Re	Water Flow Rate m^2/s	Water Inlet Re	Pressure-drop and Interface

1	8	10^{-4} (Inlet)	82	$8x10^{-4}$	2054	Constant
2	8	10^{-4}	82	$8x10^{-4}$	2054	Varied
3	0	10^{-4}	82	0	0	Varied
4	2	10^{-4}	82	$2x10^{-4}$	513	Varied
5	4	10^{-4}	82	$4x10^{-4}$	1027	Varied
6	6	10^{-4}	82	$6x10^{-4}$	1540	Varied

Cases 1 and 2 are carried out to investigate the change of hydrodynamics in non-isothermal conditions. Incorporating the change of the pressure-drop and the oil/water interface position in the calculations, Case 2-Case 6 are used to study the effect of adding water on wax deposition. To better describe the simulation results in further discussions, the water/oil and the oil/deposit interface positions are de-dimensionalized by dividing by the width of the channel. Additionally, the pressure-drop, velocities and flow rates are de-dimensionalized by dividing by the corresponding value at the inlet.

5.C Results and Discussion

5.C.1 The change of hydrodynamics in non-isothermal flow:

Cases 1 and 2 are carried out to investigate the change of hydrodynamics in non-isothermal conditions on wax deposition. The pressure-drop, flow rates, velocities and temperatures at the inlet are the same in both cases. However, Case 1 uses a velocity profile throughout the channel obtained from constant pressure-drop and interface position (CPIP) same as inlet. Case 2 uses a velocity profile with variable pressure-drop and interface position (VPIP) based on the conservation of mass flow rate. Under non-isothermal flow condition, the bulk temperature of each phase at a certain axial location is calculated by taking a velocity-weighted average of temperature throughout each phase, as shown in Equations (5.16).[63]

$$T_{\mathrm{b,oil}}(x)=\frac{\int_{H_{\mathrm{oil}}} T(x,y)V_{oil}(x,y)\,dy}{\int_{H_{\mathrm{oil}}} V_{oil}(x,y)\,dy},\quad T_{\mathrm{b,water}}(x)=\frac{\int_{H_{\mathrm{water}}} T(x,y)V_{water}(x,y)\,dy}{\int_{H_{\mathrm{water}}} V_{water}(x,y)\,dy} \tag{5.16}$$

The bulk temperatures of oil and water and the corresponding viscosities of both phase at the inlet and outlet at t = 0 (no deposition) are shown in Table 5-3.

Table 5-3: A comparison of bulk temperatures and viscosities of oil and water at the inlet and outlet for CPDIP and VPDIP at t=0

	Inlet oil bulk temperature, ºC	Outlet oil bulk temperature, ºC	Inlet water bulk temperature, ºC	Outlet water bulk temperature, ºC	Inlet viscosity of oil, cp	Outlet viscosity of oil, cp	Inlet viscosity of water, cp	Outlet viscosity of water, cp
CPDIP	74.00	4.00	74.00	4.00	1.03	386.98	0.39	1.58
VPDIP	74.00	5.64	74.00	6.03	1.03	351.18	0.39	1.49

It is seen that despite the difference in the outlet bulk temperatures and viscosities between CPIP and VPIP, both approaches predict a significant decrease in the outlet bulk temperatures and increase in the outlet viscosities of oil and water comparing to the inlet. With the approach of VPIP, this decrease in the viscosities causes an increase in the pressure-drop shown in Figure 5-7. In this case, the pressure-drop increases more than 30 times at the outlet comparing to the inlet, which is not accounted for in the approach of CPIP.

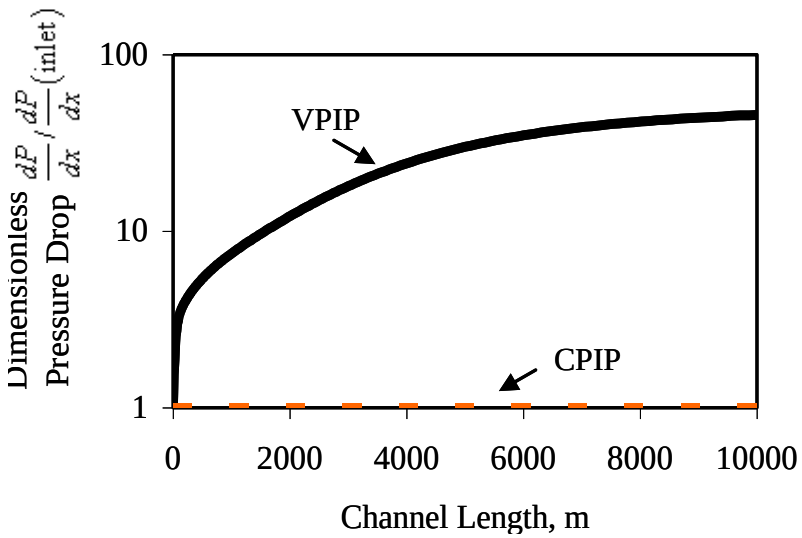

Figure 5-7: The change of pressure-drop throughout the channel in VPIP at t=0. The pressure-drop in CPIP is shown as the comparison in a dash line.

More importantly, it can be seen from Table 5-3 that the viscosity of oil increases more significantly than that of water at the outlet. With VPIP, this increase in the ratio of viscosity of oil/water leads to a decrease in the velocity of oil as well as an increase in the velocity of water, shown in Figure 5-8.

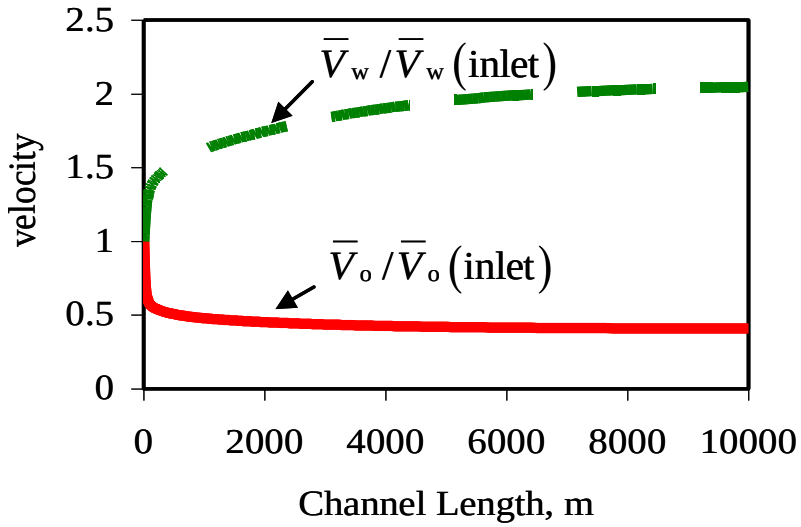

Figure 5-8: The de-dimensionalized average velocity of oil and water throughout the channel for VPIP at t=0

It is seen that the averaged velocity of oil has decreased more than 50% at the outlet while the velocity of water has increased about 100%. To maintain the constant flow rate

of each phase, the oil must flow with an increasing cross-sectional area while the water flows with a decreasing cross-sectional area. The change in the oil/water interface for VPIP is shown in Figure 5-9. It is seen that the cross-sectional area of the oil phase has increased more than 200% at the outlet.

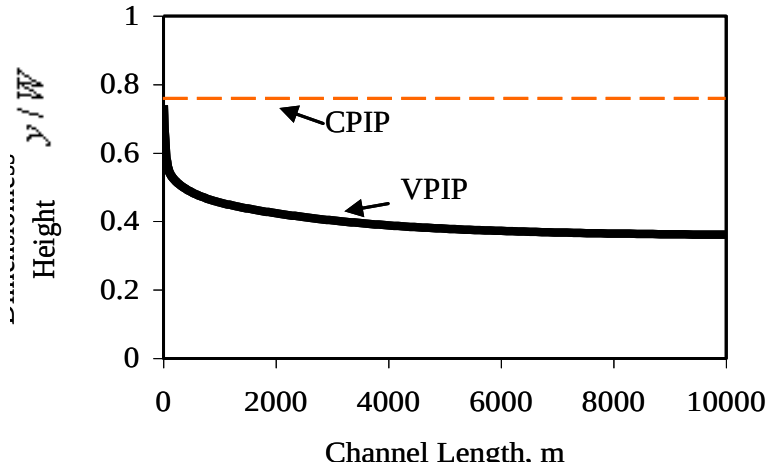

Figure 5-9: The change in oil/water interface position throughout the channel in VPIP at t=0. The interface position for CPIP is shown as comparison in a dash line.

Contrarily, with the approach of the CPIP, both the pressure drop and the position of the oil/water interface remain constant as in Figure 5-7 and Figure 5-9. This leads to a significant decrease of the flow rates of both oil and water, shown in Figure 5-10.

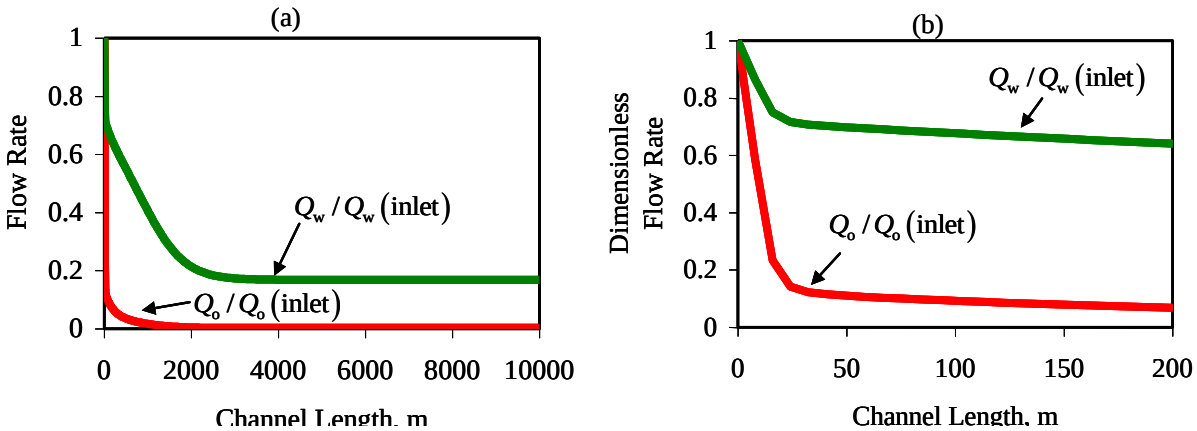

Figure 5-10: The decrease in the flow rates of oil and water throughout the channel in CPIP at t=0.
a: throughout the channel; b: 0-200 m

The decrease in the flow rates of oil and water in CPIP occurs drastically near the inlet and reaches as much as 80% at the outlet comparing to the inlet, which significantly violates the mass balance. Furthermore, this decrease of flow rate has a severe impact on predicting the wax deposition. The bulk concentration of soluble wax is calculated by taking a velocity-weighted average of temperature throughout the oil phase as given by Equation (5.17).[63]

$$C_b(x) = \frac{\int_{H_{oil}} C(x,y) V_{oil}(x,y)\, dy}{\int_{H_{oil}} V_{oil}(x,y)\, dy} \tag{5.17}$$

At t=0, the bulk concentration for CPIP and VPIP is shown in Figure 5-11. It is seen that for VPIP, the bulk concentration of wax slightly decreases along the channel due to the deposition of wax on the upper wall. For CPIP, however, a drastic under-estimate of the soluble wax in the oil phase is seen as result of the decreasing oil flow rate along the channel calculated in this approach. This under-estimate reaches about 60% at the outlet.

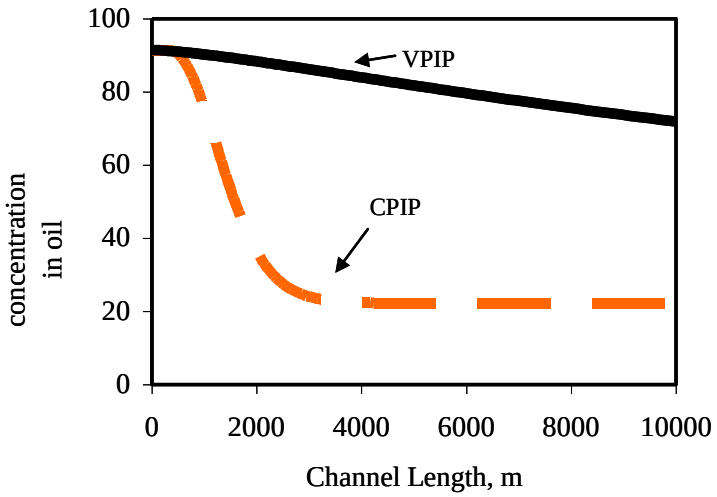

Figure 5-11: Bulk concentration of soluble wax in oil for CPIP and VPIP

The difference in soluble wax in the oil phase at t=0 indicates that the approach of CPIP greatly under-estimates the amount of soluble wax available for deposition. Consequently, the approach with CPIP significantly under-predicts the growth rate of wax deposition. Figure 5-12 shows the oil/deposit interface using both CPIP and VPIP after 700 days. It is seen that the approach of CPIP predicts a deposit maximum that reaches only 6% of the channel is blocked, while for VPIP, the deposit maximum occupies more than half of the channel.

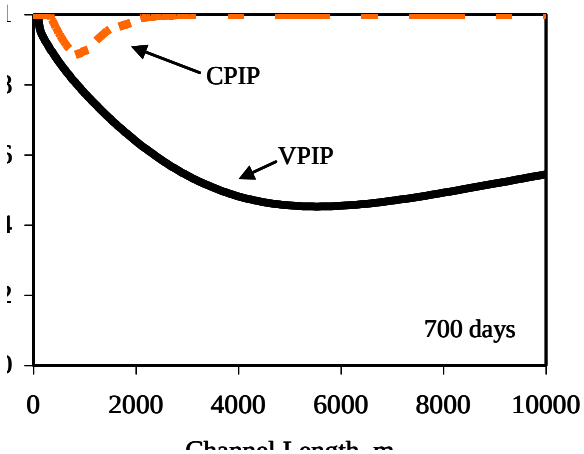

Change
Constar

Figure 5-12: Oil/deposit interface throughout the channel in Cases 1 and 2after 267days

5.C.2 The development of the wax deposit

The development of wax thickness is studied for different water/oil flow rate ratios. As a base case, the development of wax deposit in Case 3 in Table 5-2 (Single-phase flow) is shown in Figure 5-13:

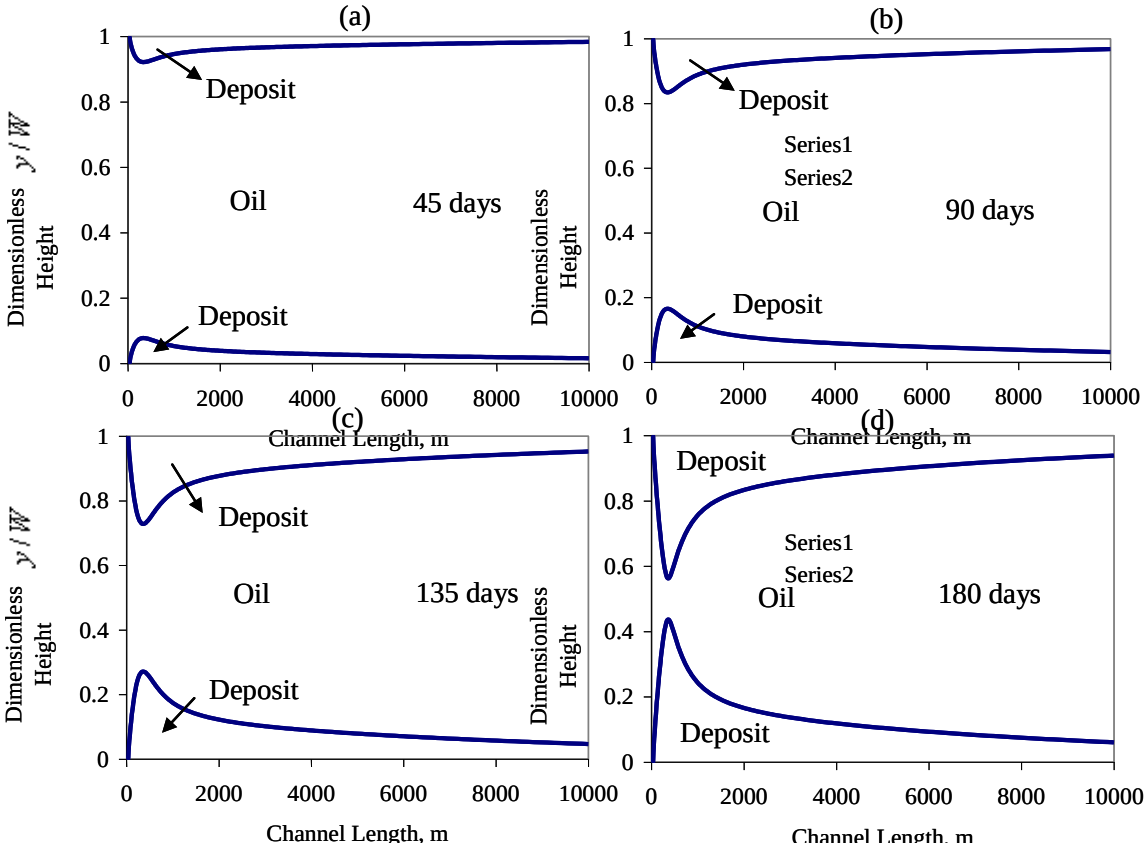

Figure 5-13: The growth of the deposit thickness in Case 3 (single-phase flow).

A maximum in the deposit thickness near the interface is seen in the channel. This maximum can be explained by the difference between the oil bulk temperature the wall temperature, which represents the driving force for wax deposition. Some insights for this maximum can be found in the temperature profiles at t=0 is shown in Figure 5-14.

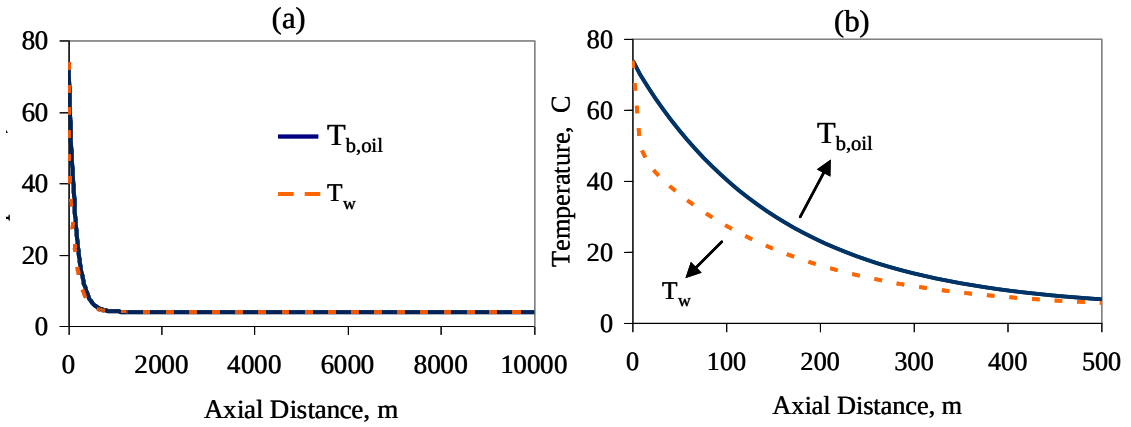

Figure 5-14: The bulk temperature of oil and the upper wall temperature at t=0 for Case 3 (Single-phase flow) . a: throughout the channel; b: 0-500 m

It is seen that the wall temperature decreases drastically near the inlet. Therefore a large amount of wax precipitates onto the upper wall and become deposit, resulting in an increase of the growth rate of the deposit thickness along the channel, which explains the increase of deposit thickness along the channel near the inlet in Figure 5-13. However, as the oil flows further down the channel. The decrease of oil bulk temperature in both cases becomes so significant that the thermal gradient for wax deposition decreases, thereby reducing the growth rate of the deposit. In other words, the maximum of the deposit is the result of a change in the difference between the bulk temperature of oil and the wall temperature along the channel.

5.C.3 The effect of water on wax deposition

Incorporating the change of the pressure-drop and the oil/water interface position in the calculations, the development of wax deposit for Case 2 in Table 5-2 (Q_w/Q_o=8) is shown in Figure 5-15.

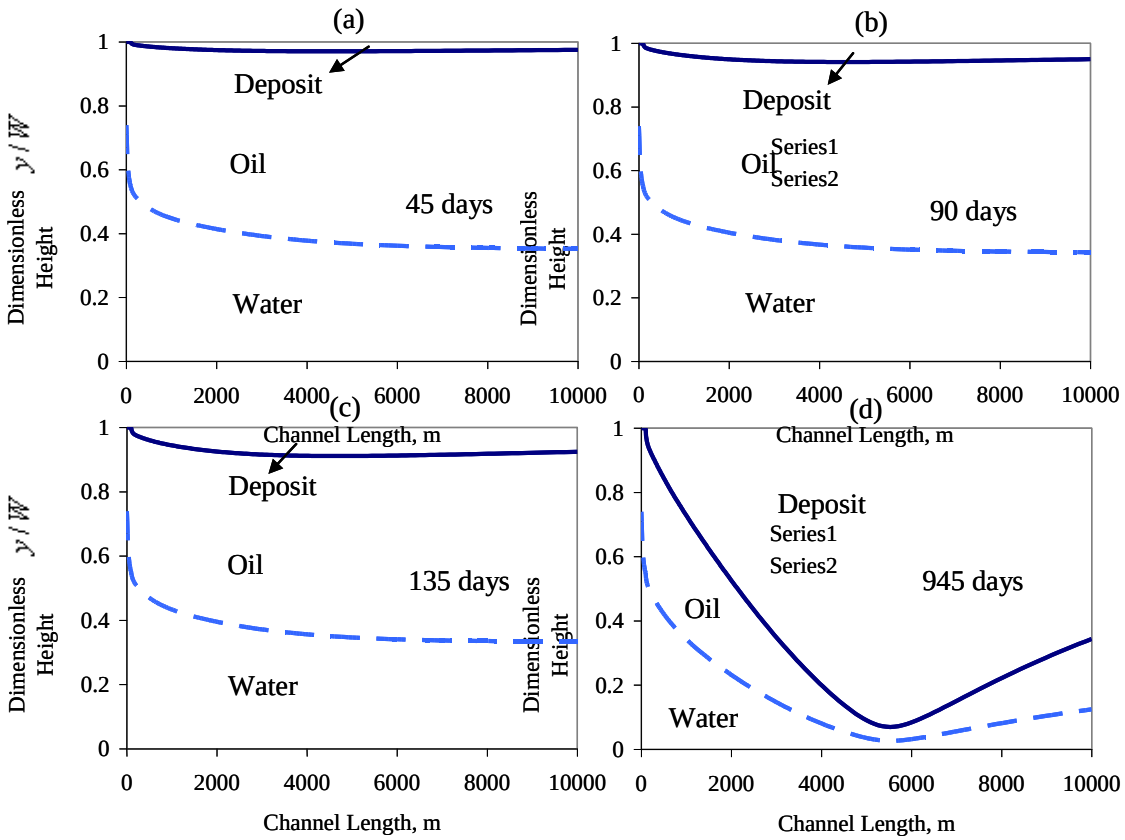

Figure 5-15 The growth of the deposit thickness in Case2 (Q_w/Q_o=8)

It is found that increasing the water flow rate significantly reduces the severity of wax deposition in stratified flow. First, comparing Figure 5-15 and Figure 5-13 a significant shift in the location of the deposit towards the outlet is seen when water is added. Additionally, the difference in the time of Figure 5-15 (d) and Figure 5-13 (d) suggests that the growth rate of deposit is significantly reduced by adding water. Figure 5-16 shows the time for the maximum of the deposit to block 95% of the channel for Cases 2-6 in Table 5-2 where the flow rate of water varies. It is seen that adding water increases the time as much as 300%. These effects of adding water on wax deposition can be explained by how it alters the heat and mass transfer characteristics in stratified flow conditions, as discussed in the next section.

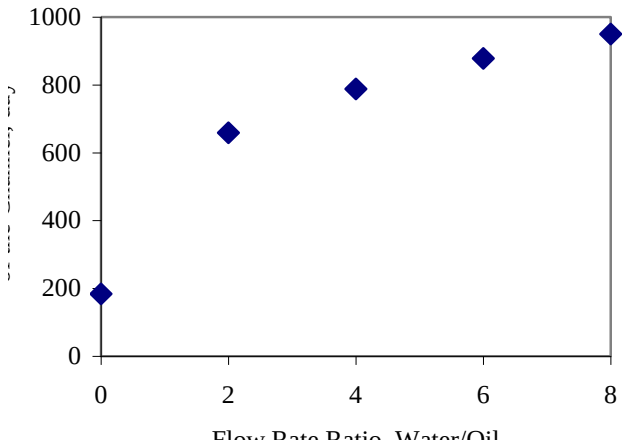

Figure 5-16: Comparison of time for 95% blockage of the channel for different oil/water flow rate ratios.

5.C.3.a Mass Transfer

In oil/water stratified flow oil become a continuous phase and is in contact with only the upper wall. Therefore the water phase serves as an insulation layer for mass transfer by preventing wax deposition on the lower wall. This explains the drastic increase of time needed when oil/water flow rate ratio changes from 0 to 2 in Figure 5-16.

5.C.3.b Heat Transfer

The addition of water has two major effects on the heat transfer that affects wax deposition. Most importantly, the energy input to the system increases with increasing water flow rate. In this case, water serves as an energy source for heat transfer. Since water has a heat capacity that is generally 2 times of that of oil, adding water provides a significant amount of energy to oil. On the other hand, the water phase, similar to an insulating material, provides thermal resistance for heat transfer to the lower wall and reduces the heat loss from the oil phase. Comparing the thermal conductivity of water (0.6 W/m/K) to polypropylene that is frequently used as insulation in offshore pipelines (0.22 W/m/K), the insulation of water is equivalent to polypropylene of about 1/3 of its

height in the stratified flow. These two effects of adding water combined leads to a more graduate decrease of bulk temperature of oil, shown in Figure 5-17 as comparison with Figure 5-14 (a).

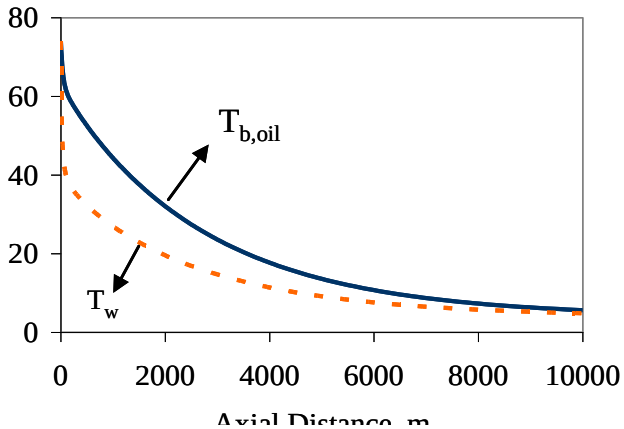

Figure 5-17: The bulk temperature of oil and the upper wall temperature at t=0 for Case 2 (Q_w/Q_o=8)

Consequently, these two thermal effects of adding water decrease the radial thermal gradient for wax deposition along the channel, leading to a smaller growth rate of deposit.

5.D Conclusions

This work provides a method to predict wax deposition in oil/water stratified flow. In order to model wax deposition, pipe-flow hydrodynamics and heat/mass transfer need to be studied. While heat/mass transfer correlations in single phase deposition modeling are well established to solve for the velocity, temperature and concentration profiles, they cannot be used for multiphase flow systems.

In this work a unidirectional flow assumption is used in the solution to non-isothermal hydrodynamics. The approximation is reasonable in subsea pipeline conditions and prevents the need to iterate on the momentum balance equation, making it feasible for the prediction of wax deposition in multiphase flow. A 2D model of oil/water

flow between two parallel plates where deposition occurs at the upper wall has been developed. The results show that under non-isothermal flow conditions, the hydrodynamics along the channel changes significantly because of a change in the viscosities of oil and water as well as the ratio of these two values caused by a change in the bulk temperature of both phases. The approach with a constant pressure-drop and interface position would drastically violate the mass balance of the oil and water and significantly under-predict wax deposition growth rate.

Based on the calculation of non-isothermal hydrodynamics and heat/mass transfer, the wax deposit thickness is predicted to growth as a function of time, where the location of the maximum deposit is seen due to the difference in the rate of the decrease of bulk temperature and interface temperature along the channel.

The addition of water is found to have significantly decreased the severity of wax deposition by changing the heat and mass transfer characteristics. From the point of mass transfer, the water phase introduces an insulation layer, reducing the contact area of oil to the wall for wax deposition. From the point of heat transfer, adding water provides additional energy to the system, which decreases the cooling rate of the oil in the channel. Furthermore, the water phase serves as an additional thermal resistance to the radial heat transfer, which reduces the heat loss to the surroundings and decreases the growth rate of the wax deposit.

Chapter 6

Indications of Gelation as an Alternative Mechanism for Wax Deposit Formation in Stratified Oil/water Flow

6.A Introduction

6.A.1 Wax deposition in oil/water stratified flow

Wax deposition for stratified oil/water flow is of great interest because most fields will produce a significant amount of water in their late life. The wax deposition model for 2D oil/water stratified channel flow developed in the previous chapter have shown that the presence of water can help to decrease the severity of wax deposition by reducing the radial diffusion of wax molecules. However, this finding has not been evaluated in 3D pipe flow conditions.

Because production pipelines field data are difficult to obtain (due to non-constant conditions and insufficient instrumentation[64]), the common method to validate the basic assumptions of a deposition model is to perform experiments in a flow loop. To this end, a state-of-the-art 2 inch flow loop was constructed at the Statoil Research Centre Porsgrunn where real waxy gas condensate from a North Sea field flows through a test section where a surrounding water annulus simulates the conditions sub-sea.[54] This flow-loop was used to study wax deposition for stratified oil/water flow, which is of great interest because most fields will produce a significant amount of water in their late life.

This study investigates how an increasing water cut* will influence wax deposition and the pigging frequency.

6.A.2 Different mechanisms for deposit formation

Previous studies have shown that a wax deposit can be formed by two possible mechanisms: 1) diffusion of wax molecules from the bulk oil to the oil-deposit interface[14] and 2) gelation due to crystallization of wax molecules.[65-74] These two mechanisms will be further discussed in detail.

Diffusion of wax molecule at the oil/deposit interface.[14] Due to the heat loss of the oil to the surroundings, the temperature of the wall decreases and wax molecules start to precipitate at the wall to form an incipient layer of deposit. This precipitation reduces the concentration of wax at the oil-deposit interface and generates a radial diffusion of wax molecules from the bulk towards the oil-deposit interface. The wax molecules that diffuse to the oil-deposit interface can either precipitate at the interface to increase the thickness of the existing deposit or continue to diffuse into the deposit and contribute to the increase of wax fraction in the deposit. This diffusion of the wax molecules (the heavy components) in to the deposit is accompanied by the counter-diffusion (the light components) of the oil molecules from the deposit back to the oil phase. Consequently, the deposit resulted from diffusion is enriched with heavy components. The trend was originally found by study of Singh and Fogler, as shown in Figure 6-1.

* The term "water cut" describes the fraction of the water flow rate based on the total flow rate, $[Q_w/(Q_w + Q_o)]$, as an operating condition for the experiments.

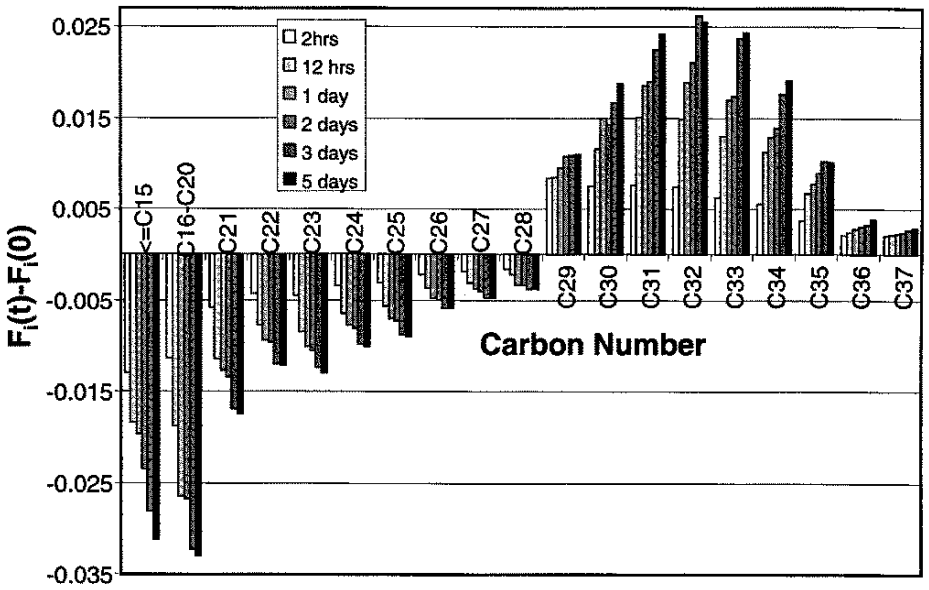

Figure 6-1: Change in carbon number distribution of gel deposits from flow loop with times[14]

Gelation due to the crystallization of wax molecules. The crystallization of wax in oil has been studied since the 1920s[65].The crystal structures observed from optical microscopy for the n-paraffins formed under static conditions are mainly platelet-like crystals with the diameters of 30-100 μm[65-68], although the existence of the branched and cyclic paraffins can significantly alter the structure and the crystallinity of the gel[69,70]. Kane *et a.l* has used cryofixation with transmission electron microscopy (TEM) to reveal the micro-structure of the wax crystals[71], as shown in Figure 6-2.

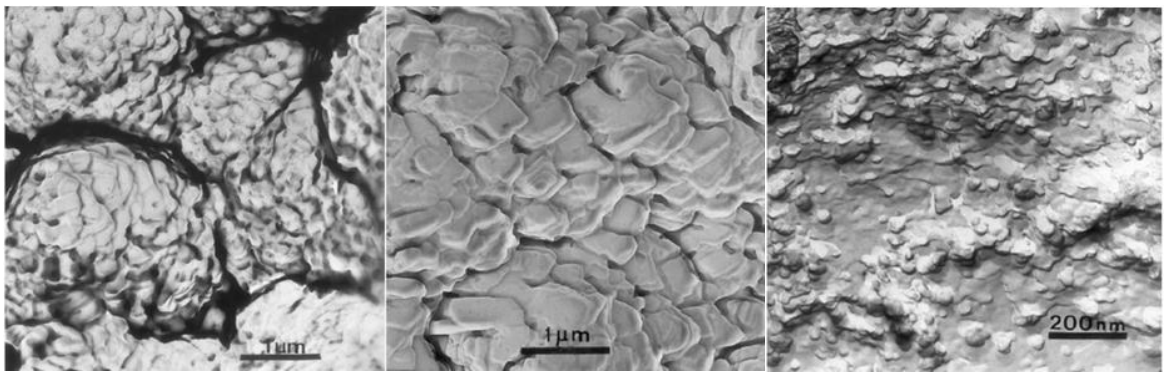

Figure 6-2: The micro-structure of the wax crystals observed by Kane, et al.[71] (a) The "pine cone" structure of paraffin crystallized from in the crude oil. (b) The wax platelet lamellas observed on each "pine cone" structures (c) The disc-like sub-units that form the platelet lamellas.

It was found that the wax crystals consist of smaller "pipe cone" blocks of around 3-5μm. Each block includes the platelet structure with stratified lamellas of area around 0.5-1μm^2. A closer examination at the surface of the lamella reveals that the platelet consist of disc-like sub-unites with diameters of 20-40 nm, which is considered to be the locations of the nucleation as the initial stage of wax crystallization. It is believed that the aggregation of these disc-like sub-units forms the platelet lamellas, while the overlapping of the platelet lamellas forms the "pine cone" structures. It is believe that the aggregation of the "pine cone" structures forms the platelet crystals that one frequently sees in an optical microscope.[65-68]

As temperature further decrease from the cloud point, the degree of wax crystallization becomes sufficient to form a crystal network so that the entrapped oil is no longer able to flow. The mixture of the solid network and its entrained oil forms a gel. A number of studies on the structure of the network of wax crystals reveal that the growth of the wax crystals and the aggregation of the existing crystals occur simultaneously and that the network is connected by the attractive interactions between the wax crystals.[66]

Although wax gelation has been frequently observed in quiescent conditions, recent studies have focused on the investigation on the wax gel formed under shear/flow conditions[68,71-73]. Venkatesan *et al.* has shown that a model wax-oil system was still able to gel when the shear stress is as high as 5 Pa (corresponding to a flow rate of 16,000 barrels per day in a 10-inch pipeline with an oil viscosity of 10 cp)[68]. The imposed shear rate is known to delay or suppress gelation, as reported by several rheological studies[71-74]. Kane *et al.* found that the shear stress can significantly reduce the gelation temperatures. This conclusion was found from the drastic increase of the apparent viscosity from their rheometer measurements as shown in Figure 6-3.

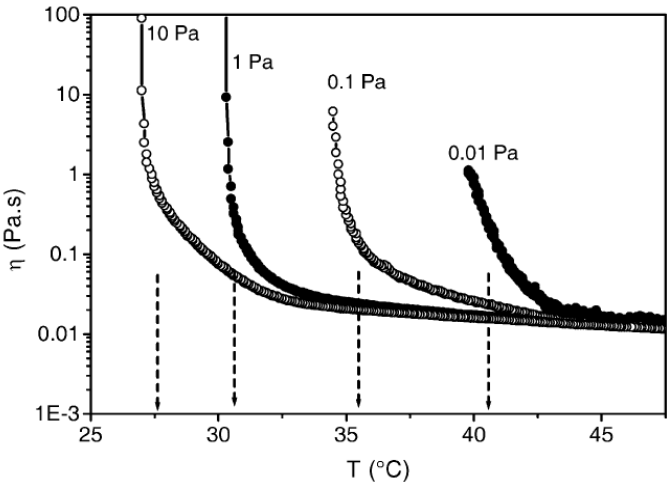

Figure 6-3: The impact of impose shear stress on gelation temperature from the study of Kane et al.[72] The gelation temperatures are highlighted with vertical dash lines where steep increase of the apparent viscosity is observed. The cooling rate is 0.5°C/min.

A summary of the conditions necessary for diffusion-formed deposit and gelation-formed deposition are listed in Table 6-1.

Table 6-1: Summary of conditions for diffusion and gelation as well as the difference in the amount of heavy components formed by these two mechanisms

	Diffusion	Gelation-driven
Prerequisites	Radial temperature gradient T_{wall} <WAT	T << WAT Low shear rate

Heavy component fraction in the deposit	Higher than oil	Low

Not only do diffusion and gelation have different prerequisites, it is expected that these two types of mechanism should yield deposits with different compositions: Because a radial concentration gradient, a prerequisite for diffusion, is not required for gelation-formed deposition, there is no reason for an enrichment of heavy components in a gelation-formed deposit. In other words, if one is to carry out a GC analysis of a deposit that is only formed by gelation, its carbon number distribution should be the same as that of the crude oil. As we have discussed previously that a diffusion-formed deposit consists of a higher fraction of heavy components than the crude oil, it must have a higher fraction of heavy components than a deposit that is gelation-formed, as is sketched in Figure 6-4.

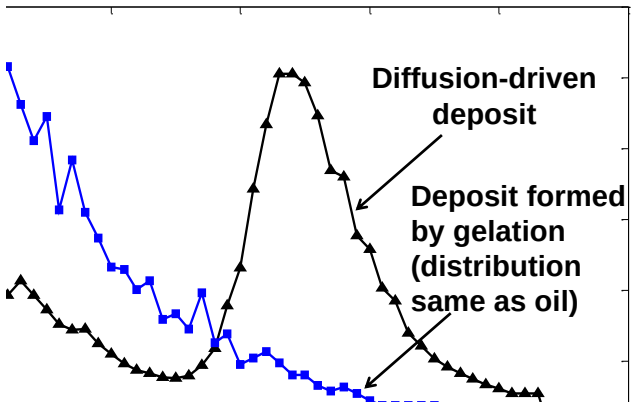

Figure 6-4: Comparison of the carbon number distributions from GC measurements of between a diffusion formed deposit and a gelation formed deposit, which has the same carbon number distribution of the crude oil.

In the two-phase experiments in this study, the conditions for diffusion to occur are satisfied as the radial temperature gradient has been established by the heat loss from the oil and the water to the coolant and the wall temperature is less than WAT(30ºC). The

shear stress at the wall is around 0.5 to 1 Pa for the oil phase, which is well within the reported range of the shear stress where gelation can occur (<5 Pa).[68] Therefore, both the gelation and diffusion mechanisms can contribute to the formation of the wax deposit. It will be subsequently shown which mechanism is prevalent to the formation of the wax deposits at different water cuts.

6.B Experimental setup

6.B.1 Wax deposition flow loop apparatus

The state-of-the-art flow loop apparatus, also called a test rig, used for the experimental program is located in the Multiphase Flow-Loop Laboratory at Statoil's Research Centre Porsgrunn, Norway. It is used to study wax deposition mechanisms and to develop technologies for wax removal, wax prevention and wax thickness measurements. A schematic layout of the flow loop apparatus is shown in Figure 6-5.

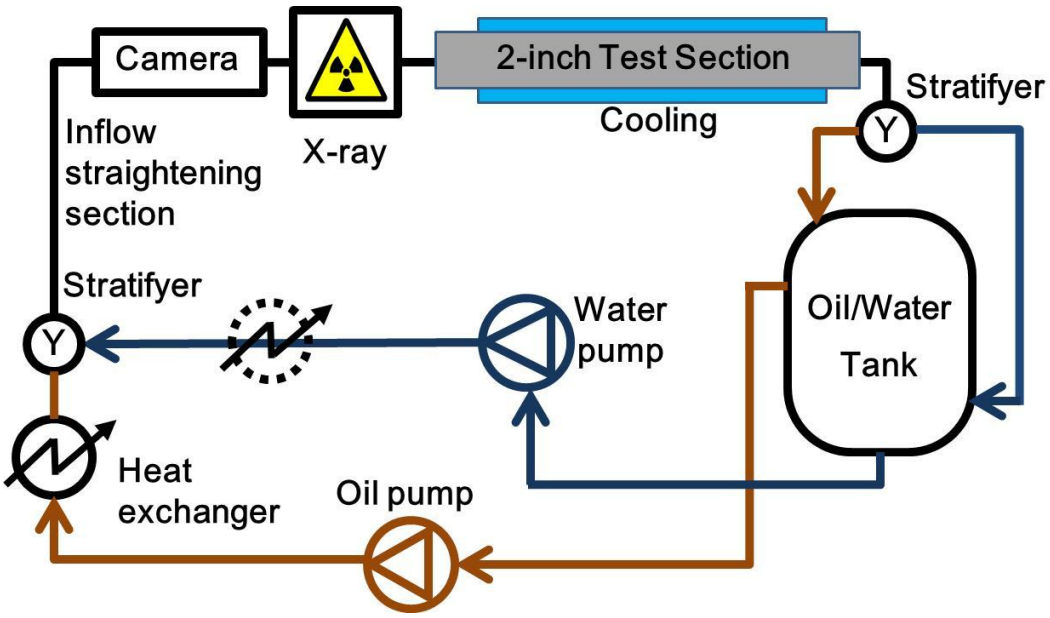

Figure 6-5: Overview of the wax deposition flow-loop

Before an experiment begins, the water and oil phases are pre-heated separately using an oil heat exchanger. Pre-heated oil and water are continuously circulated in the flow loop using the water and oil pumps. The oil phase is circulated through the heat exchanger during the experiment to keep the oil temperature constant. Because there is no separate heat exchanger to keep the water temperature constant, the water temperature drops slightly during the course of an experiment to a lower level. In a future modification, an additional heat exchanger for the water flow shall be implemented to avoid this drawback. The oil and water are unified in a Y-shaped stratifier which initializes stratified flow by avoiding excessive mixing of the phases. Oil and water then flow through a 17 m long pipe section to ensure fully developed flow before entering the test section. After the inflow section, the flow enters first a window section for visual observations of the flow structure followed by an X-ray tomograph for measuring the phase distribution. Next, the fluids enter the 2-inch test section where they are cooled by water that is circulating in an annulus surrounding the oil pipe, simulating the conditions subsea. The coolant water is provided from the communal network and is heat exchanged with steam to achieve the specified temperature before entering the test section annulus.

Two test sections (one 2-inch and one 3-inch inner diameter) are available to investigate the scale-up behavior of wax deposition. However for this study only the 2-inch section was used. Before the oil and water return to the main separator, the phases are pre-separated in a splitter. The two streams from the splitter enter the main separator in two different locations. Having both a pre-separation and a main separator improves the separation and hence lowers the total separation time. The large main separator with a maximum volume of 4.2 m^3 was been designed to give a long retention time (up to 1 hour

for the lowest flow rates) and to prevent wax depletion of the circulating oil. Density measurements in front of each pump are used to monitor the separation quality of the phases. Some key data for the rig may be found in Table 6-2

Table 6-2: Dimensions and the range of the operating conditions for the flow loop

Pipe material	Stainless steel	X2CRNi17-13-2	Parameter	Range
Oil pipe	Inner diameter	$52.5mm$	Oil temperature	$10°C - 60°C$
Oil pipe	Outer diameter	$60.6mm$	Water temperature	$10°C - 60°C$
Water annulus	Inner diameter	$131.3mm$	Oil flow rate	$2\frac{m^3}{h} - 20\frac{m^3}{h}$
Whole test section	Length	$5.31m$	Water flow rate	$2\frac{m^3}{h} - 20\frac{m^3}{h}$
Removable test section	Length	$0.63m$	Cooling flow rate	$3\frac{m^3}{h} - 16\frac{m^3}{h}$
Tank	Max. volume	$4200l$	Pressure	$1bar$

6.B.2 X-ray tomography

An X-ray tomograph was used to measure the vertical phase distribution in the pipe before the flow enters the test section. The tomograph was built by Innospexion AS and consists of two pairs of X-ray sources and detectors, so that both the horizontal and the vertical phase distribution can be measured. The X-ray source is a water-cooled MB70 MCA 450 monoblock X-ray source with a maximum energy of 60 kVp. The detectors consist of CdTe CMOS detector arrays with 1500 pixel resolution.

The water volume fraction was calculated from X-ray measurements which were performed over 30 seconds to average over all transient flow phenomena. A sketch of the X-ray measurement is shown in Figure 6-6. The water volume fraction for a two-phase flow f(x) as a function of the vertical position x is obtained by comparing the measured x-ray intensities for oil-water flow $I_{ow}(x)$ with the intensities for single-phase oil flow $I_o(x)$ and single-phase water flow $I_w(x)$, as shown in Equation (6.1)

$$\phi(x) = \frac{\ln \frac{I_{ow}(x)}{I_o(x)}}{\ln \frac{I_w(x)}{I_o(x)}} \tag{6.1}$$

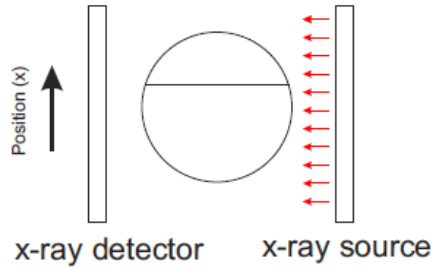

Figure 6-6: Layout of vertical X-ray measurement

The logarithm in Equation (6.1) stems from the attenuation of the X-ray beam passing through the fluid. A more in-depth description of the theory can be found in the research by Hoffmann and Johnson[75].

6.B.3 Gas Chromotography

Gas chromatography was used to measure the carbon number distributions of the deposit were measured using. The crude oil is measured using high temperature gas chromatograph (HTGC) Hewlett-Packard 6890A equipped with a CP-SimDist Ultimetal column (25m x 0.53mm x 0.09mm). The oven temperature was initiated at 40˚C and increased to 430˚C at a rate of 10˚C/min.

6.B.4 Fluid Characteristics

6.B.4.a Oil and water composition

The North Sea gas condensate utilized in this research is the same as in the previously reported single-phase study (4.7 wt% wax content, 30°C WAT, η = 3cP @ 20°C).[54] The salt concentration of the water phase was chosen to be equal to the formation water from that field. The ion concentrations are listed in Table 6-3.

Table 6-3: Water composition

Ion	Concentration [mg/l]
Sodium, Na	158
Calcium, Ca	16
Potassium, K	204
Chloride, Cl	735
Sulphate, SO4-	33

6.B.4.b Emulsion breaker to encourage water/oil flow

Short-time deposition tests have shown that gravity separation in the tank is not sufficient to encourage oil/water phase separation to occur at lower temperatures and higher flow rates. It was therefore decided to add a commercially available emulsion breaker (DMO 86538, 500 ppm) to improve separation.

6.C Results and Discussions

6.C.1 Hydrodynamics

The most interesting parameter in two-phase oil/water flow is of course the water cut. To investigate its influence and to define the matrix of most relevant wax deposition experiments a pre-study was performed where the influence of the water cut on the flow regime was investigated.

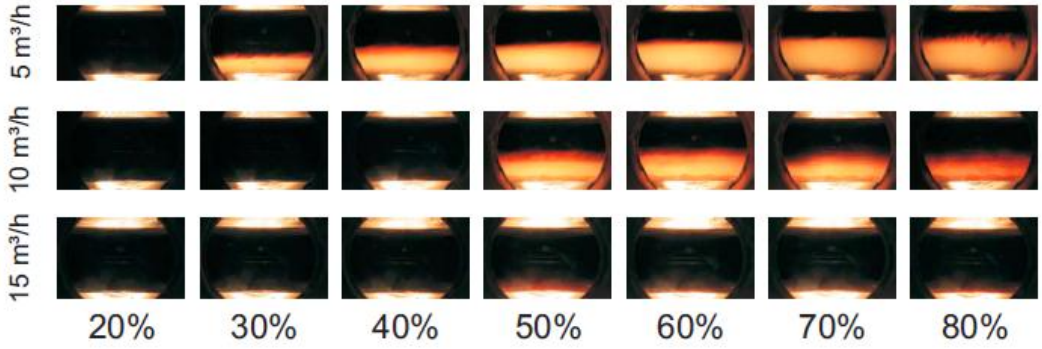

Figure 6-7: Camera picture at different water cuts

Experiments were carried out for three different total volumetric flow rates. These two-phase flow rates were $Q_{total} = Q_o + Q_w = 5m^3/h$, $Q_{total} = 10\ m^3/h$, and $Q_{total} = 15\ m^3/h$, corresponding to mixture velocities of $V_{total} = 0.64m/s$, $V_{total} = 1.28m/s$, and $V_{total} = 1.92m/s$. Experiments were carried out with water cuts ranging from 10% to 90%. Figure 6-7 shows the photographic pictures for these flow regimes. It is observed that completely stratified flows occur for the case of water cut from 30% to 70% when the total flow rate is $5m^3/h$, while completely stratified flows occur in a smaller range of water cut (50%-60%) as the total flow rate increases to $10m^3/h$. This observation indicates that the degree of dispersion increases with increasing total flow rate.

Visual impression however can be misleading because relatively small amounts of dispersed oil in water make the mixture appear dark. It is therefore important to measure the water volume fraction using the X-ray instrument. Figure 6-8 shows the water fraction distribution for the three flow rates.

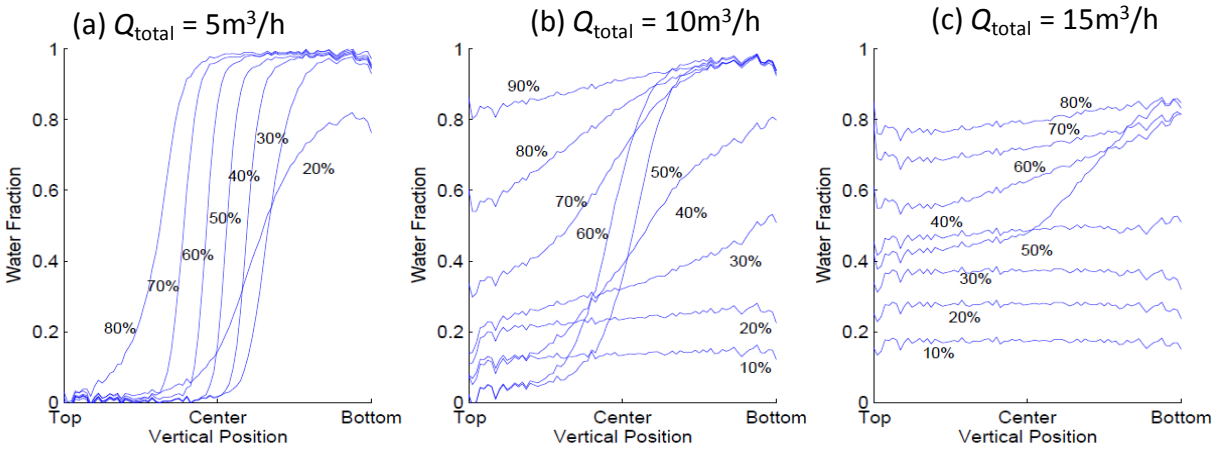

Figure 6-8: Water fraction at different water cuts - X-ray measurements

Correspondingly to the reflex camera pictures, the lowest flow rate, 5 m^3/h, gave fine stratified flow regimes except water cuts = 20% and 80%, where some dispersion was

observed. For the flow rate of $10m^3/h$ there is a clear transition from fully dispersed flow at 10% and 20% water cut to stratified flow (around 40% to 70% water cut) and further on to water continuous flow. The highest flow rate of 15 m^3/h shows almost always fully dispersed flow with the exception of 50% water cut which appears to be stratified flow of a water continuous and an oil continuous phase (albeit with a high amount of dispersion in each of the phases).

Because the scope of this study focuses on stratified flow it was decided to perform one series of experiments with varying water cut at a total flow rate of $5m^3/h$ and one series at a total flow rate of $10m^3/h$. In the later study we hope to extend this investigation also to higher flow rates and dispersed flow. Dispersed phase flow will however require modifications of the rig since it proved to be impossible to maintain a sufficiently high separation quality for the duration of a whole wax deposition experiment (typically several days). This drawback lead to the build-up of a significant amount of emulsion as the experiments are running at highest flow rates.

6.C.2 Deposit Characterization

Two lists of deposition experiments are shown in Table 6-4 and Table 6-5 for different total flow rates. It can be seen that the inlet temperatures for the oil and the coolant are not the same, which is due to the limited number of heat-exchanger available in the flow-loop.

Table 6-4 List of operating conditions for the deposition experiments with different water cuts for the total flow rate of 5m^3/h

Total Flow Rate (m^3/h)	5.0					
Water Cut (%)	0.0†	25.0	50.0	65.0	75.0	80.0
Oil Flow Rate(m^3/h)	5.0	3.7	2.5	1.7	1.2	1.0
Water Flow Rate (m^3/h)	0.0	1.3	2.5	3.3	3.8	4.0
Duration (days)	2.0	2.6	2.7	2.7	2.7	2.7
Oil Inlet Temperature	24.0	24.0	24.0	24.7	25.0	24.4
Water Inlet Temperature	-	23.1	21.6	22.0	21.3	20.5
Coolant Temperature (^{o}C)	15.0					

Table 6-5 List of operating conditions for the deposition experiments with different water cuts for the total flow rate of 10m^3/h

Total Flow Rate (m^3/h)	10.0				
Water Cut (%)	0.0†	10.0	50.0	75.0	85.0
Oil Flow Rate(m^3/h)	10.0	9.0	5.0	2.5	1.5
Water Flow Rate (m^3/h)	0.0	1.0	5.0	7.5	8.5
Duration (days)	1.8	2.8	1.8	1.7	1.8
Oil Inlet Temperature	25.0	25.0	25.0	24.9	24.8
Water Inlet Temperature	-	24.6	23.5	22.9	22.5
Coolant Temperature (^{o}C)	15.0				

† The GC measurement is not available for these experiments

6.C.2.a Comparison of formation mechanisms by the comparison of carbon number distributions

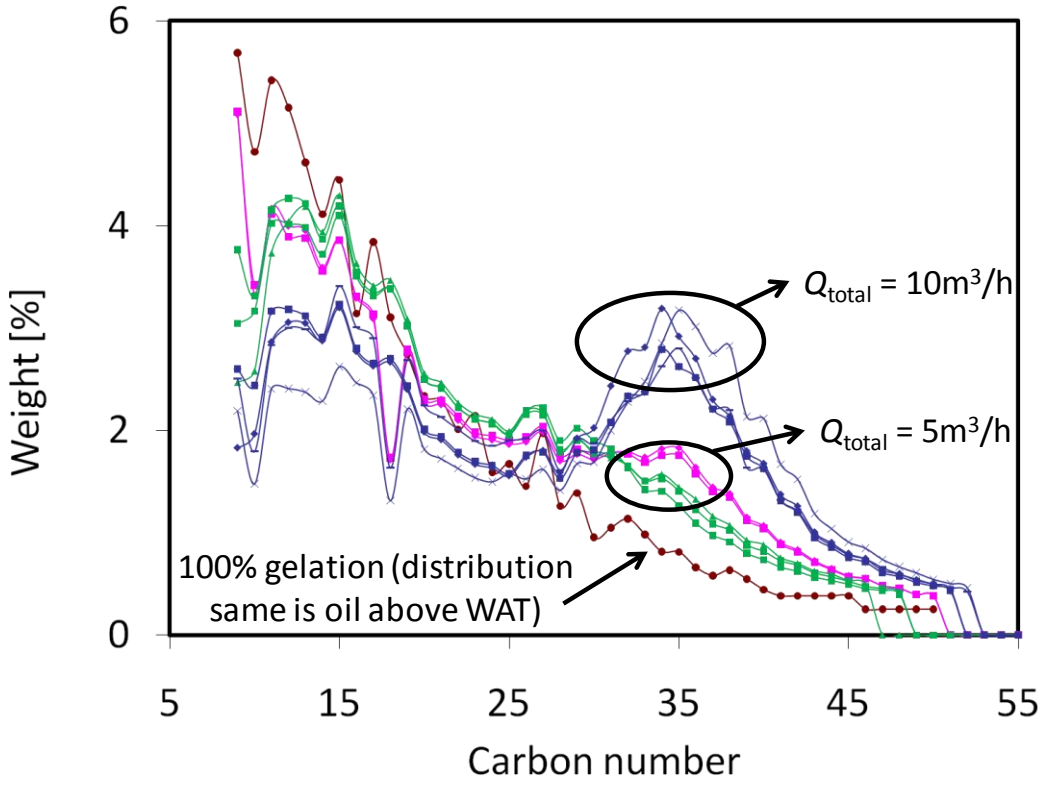

Figure 6-9 Carbon number distribution for the deposit for the experiments of different total flow rates

Figure 6-9 shows the carbon number distribution from the GC measurements of the deposits for all the experiments. Drastic difference can be seen between the carbon number distributions in the deposits for the experiments with different total flow rates. Comparing to this difference, the variation in the carbon number distribution for the deposits with the same total flow rate but different water cut is much less significant. For the total flow rate of $5m^3/h$ (shear stress at the wall at around 1 Pa ~ 1.5 Pa), the carbon number distributions of the deposits become very close to that of the oil. As discussed previously a deposit completely formed by gelation has the same carbon number distribution of the oil above WAT, it is expected that the deposit formation in these two groups are highly gelation-driven. However, as the total flow rate increases to $10m^3/h$

(shear stress at the wall around 3.4 Pa ~ 4.8 Pa), significant amount of heavy components (C28+) are seen in the deposits, indicating that diffusion is the major mechanism in the formation of the deposits.

A close examination of the carbon number distributions of the deposits for the experiments with total flow rate of 5m^3/h reveals the variation as the water cut changes, which is shown in Figure 6-10.

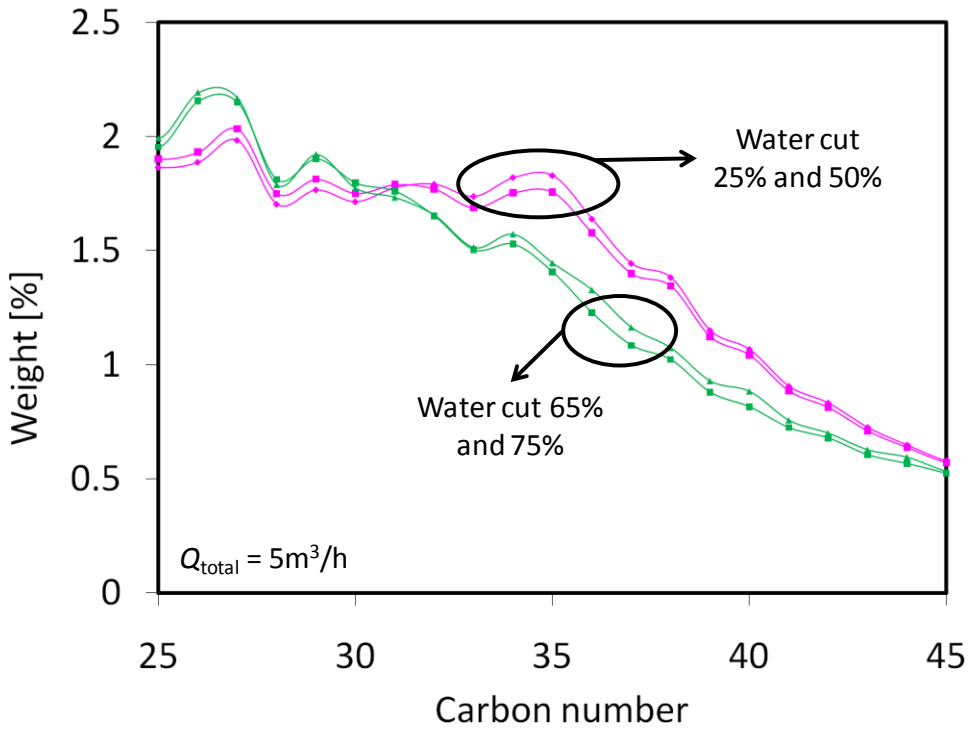

Figure 6-10 Carbon number distribution for the deposit with the experiments of different water cuts while the total flow rate is maintained at 5m^3/h

The deposits from the experiments with the water cut of 65% and 75% have smaller fractions of the heavy components. Their carbon number distributions are more similar to that of the oil compared the deposits from the experiments with water cut of 25% and 50%, which indicates that gelation is more dominant in high water cuts. A possible explanation for this difference in the degree of gelation among the experiments with different water cuts can be found from the difference in the shear stress in the oil phase,

which is known to defer gelation.[68,72] Because the oil and the water used in this study are mainly Newtonian fluids, the shear stress is directly proportional to the viscosity of the fluid. The viscosity of the oil is approximately twice of that of the water for the temperature within the operating range in this study. The distribution of the water volume fraction for the flows with these water cuts (Figure 6-8 (a)) shows an increasing amount of water in the oil as the water cut increases from 50% to 80%. Therefore this increasing amount of water in the oil phase can help to reduce the shear stress of the oil phase, thereby encouraging gelation to occur.

6.C.2.b The comparison of weight the deposit and the area that is covered by the deposit

Figure 6-11 (a) shows the weights of the wax deposit measured at the end of the experiments. It should be noted that the surface areas of the pipe covered by the wax deposit are different between experiments with different total flow rates and different water cuts, as shown Figure 6-12 and Figure 6-13[‡]. Consequently, a more reasonable comparison would be the weights of the deposit divided by the arc areas covered by the deposit, which are shown in Figure 6-11 (b).

[‡] The weight of the deposit for water cut of 10% and total flow rate of $10 m^3/h$ is not listed because the duration of the experiment is different from the rest of the experiments of the same flow rate and different water cut.

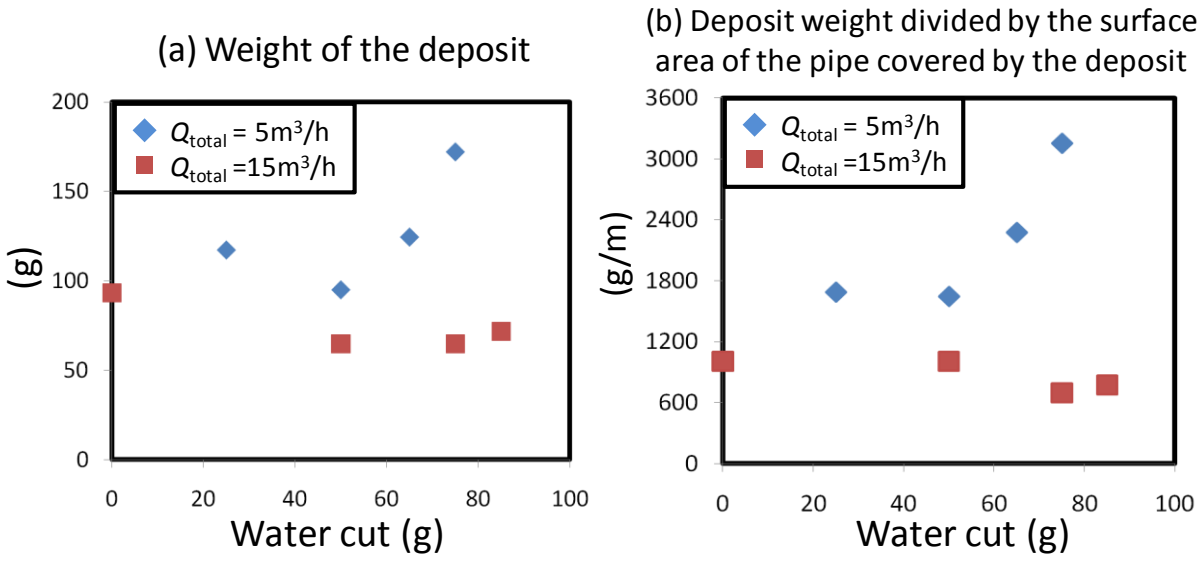

Figure 6-11 The Weights of the deposit and the weights of the deposit per unit surface area of the pipe covered by the deposit

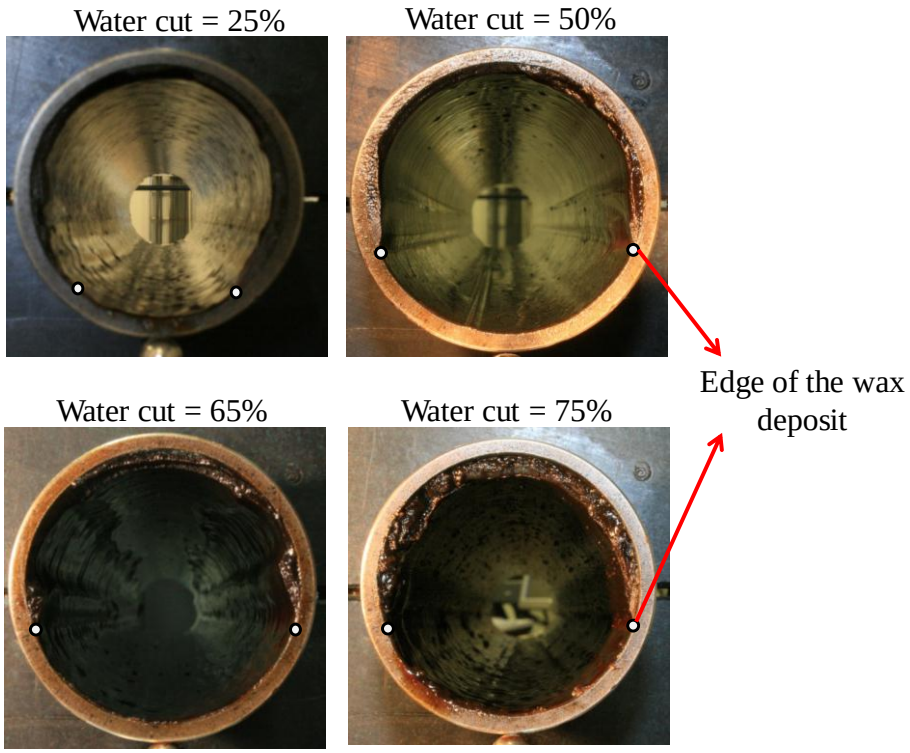

Figure 6-12 Camera pictures of the wax deposit for the experiments with total flow rate of 5m^3/h

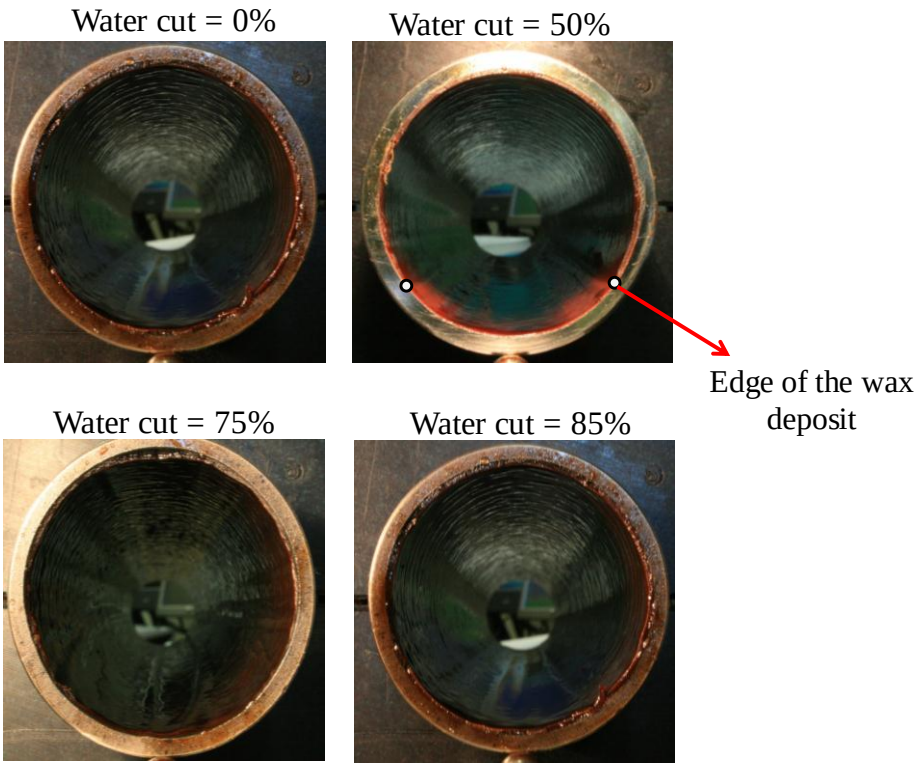

Figure 6-13 Camera pictures of the wax deposit for the experiments with total flow rate of 10m^3/h

It can be seen that the weights of the deposit for the deposition experiments with total flow rate of 5m^3/h are higher than those with the total flow rate of 10m^3/h. For the experiments with total flow rate of 5m^3/h, the thicknesses of deposits at the water cut of 65% and 75% are higher than those at the water cut of 25% and 50%. The degree of gelation and the thickness of the deposit for all of the experiments are listed in Table 6-6.

Table 6-6: The degree of gelation and the thickness of the deposit for the experiments with different shear stress

	Q_{total} = 10m^3/h	Q_{total} = 5m^3/h	
		Water cut 25% ~ 50%	Water cut 65% ~ 75%
Shear stress of the oil phase	Highest	Low	
Degree of gelation	Lowest	High	Highest
Deposit thickness	Lowest	High	Highest

It can be seen that a decrease in the shear stress in the oil phase corresponds to an increase in the degree of gelation as well as the thickness of the deposit. This finding is consistent with the existing conclusions for single-phase flow that a decrease in the oil flow rate can lead to an increase in the thickness of the deposit and a decrease in the wax fraction in the deposit.[54]

6.D Conclusions

In this research, wax deposition experiments in oil/water two-phase stratified flow were carried out in order to investigate the effect of the presence of water on wax deposition. First, a flow map study is performed to identify the flow regimes for oil/water stratified flow. The X-ray measurement shows that completely stratified flow was achieved in the cases of water cut ranging from 30% to 60% at low total flow rate (Q = 5m^3/h). As the total flow rate further increases, the formation of the oil/water droplets reduces the degree of stratification and even prevents stratified flow to occur.

Wax deposition experiments were carried out at various water cuts for the total flow rate of 5m^3/h and 10m^3/h. The GC analysis for the composition of the wax deposit further confirmed the co-existence of the two mechanisms in deposit formation: diffusion and gelation. For the experiments with total flow rate of 5m^3/h, it is seen from the GC analysis that deposit share very similar compositions with the oil, indicating that the formation of the wax deposit is highly gelation-driven. The fractions of the heavy components in the deposits increase as the total flow rate increases from 5m^3/h to 10m^3/h, indicating that the degree of wax gelation is reduced. This finding is consistent with the conclusion from the recent rheology studies which show that increasing shear stress defers gelation. The weight measurements further reveal that the experiments with lower

total flow rates (lower shear stress) yield greater amount of wax deposit. This finding provides an alternative explanation for the existing wax deposition studies in single-phase flow that the deposit thickness greatly increases as the oil flow rate increases.

As the degree of gelation is determined by a variety of elements including the shear stress, the cooling rate, the temperature and the wax content of the oil, future work should be dedicated to extending the existing knowledge of these effects on gelation at quiescent conditions to flow conditions.

Chapter 7

Future Work

7.A Further investigation gelation as an alternative formation of wax deposits in single-phase oil flow

As discussed in the previous chapter, gelation can be a dominant mechanism for the formation of wax deposit at low oil flow rates, which corresponds to low shear stress at the wall. The carbon number distribution for the deposit is a significant indicator of the degree of gelation in the formation of the deposit. If a deposit that is completely formed by gelation, it must have the same carbon number distribution as the crude oil. Consequently, by comparing the carbon number distribution of the deposit one can qualitatively identify the degree of gelation (compared to diffusion) for the mechanism for the formation of the wax deposit. As the deposition-driven formation represents the continuous radial transport of wax molecules depositing on the interface, its resulting deposit is expected to contain more solids than a gelation-driven deposit. Consequently, the deposit formed mainly by deposition is expected to have higher mass fractions of heavy alkanes than that formed by gelation. The GC analyses of most of the experiments have been carried out and shown in Figure 7-1. The corresponding wall temperatures and flow rates and for these experiments are shown in Figure 7-2

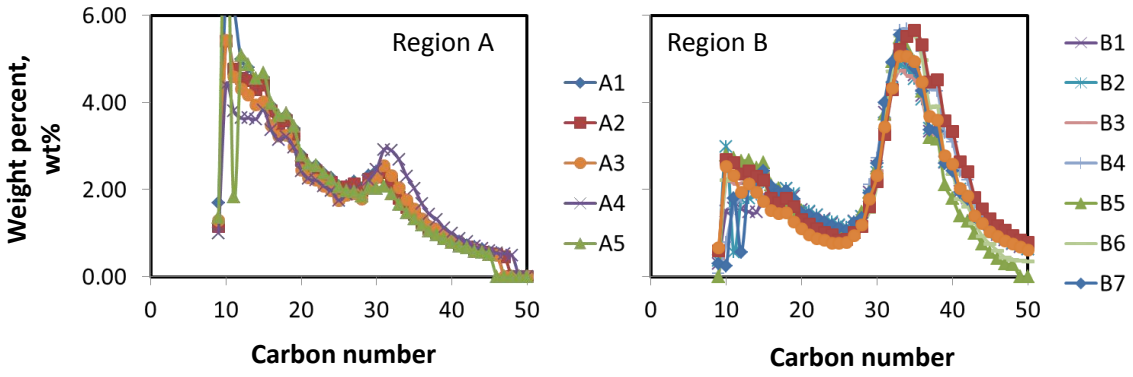

Figure 7-1 GC analyses of experiments

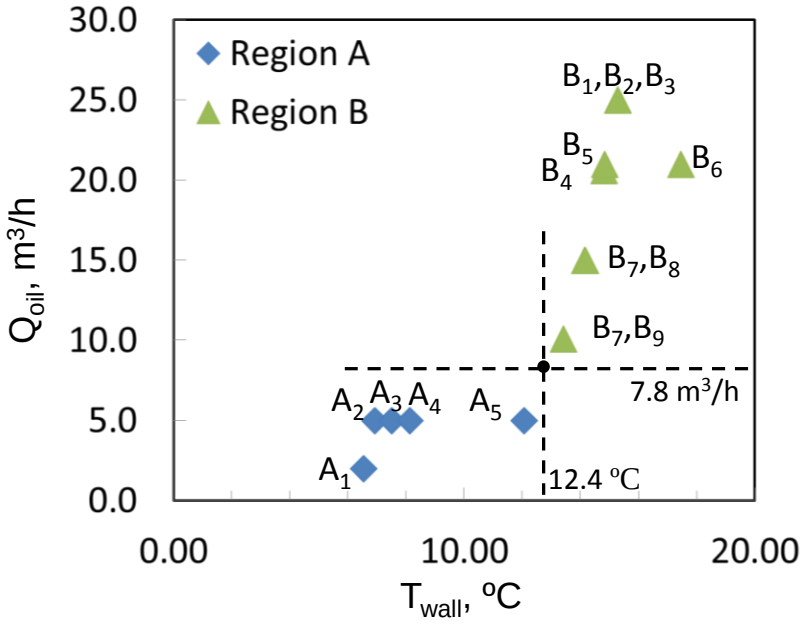

Figure 7-2 Experimental conditions

. It is clearly seen that the carbon number distribution of the experiments can be divided by two categories, despite the significant differences of the wall temperatures and oil flow rates within each group.

Region A ($7^{o}C < T_{wall} < 12.5^{o}C$, $2m^3/h < Q_{oil} < 5m^3/h$):

It is seen that in this region a very small fraction of heavy components are present in the deposits. A decreasing fraction of the heavy components indicates an increasing degree of gelation in the formation of the deposits. Consequently, it is believed that the wax deposits in Region 1 are mainly gelation-driven.

Region B (14ºC < T_{wall} < 18ºC, 10m^3/h <Qoil < 25m^3/h):

It is seen that the deposits in this region have a much higher fraction of heavy components, indicating that the deposit is mainly formed by diffusion and the degree of gelation is insignificant compared to that in Region A.

The drastic similarity of the carbon number distributions within each region indicates that there appears to be a cut-off point (in this study it would be T_{wall} ~ 13ºC and Q_{oil} ~ 7.5m^3/h) where the degree of gelation is significantly altered. The immediate future investigation should be focused on measuring the gelation temperatures of the oil at various shear rates and cooling rates to learn if the results are consistent with this cut-off point. In addition, the carbon number distributions of deposits for the experiments with the oil flow rate and the wall temperature located adjacent to the two regions discussed above should be investigated to determine if there is a gradual transition of the carbon number distribution from those in Region 1 to Region 2.

Gelation has been studied extensively in quiescent conditions. The degree of gelatin is reported to be affected by a number of factors in quiescent conditions, including the cooling rate, the shear stress, the temperature as well as the oil composition. An increasing cooling rate has been shown to encourage the formation of larger crystals and lead to the formation of stronger waxy gel[76,68,74] An increasing shear rate/shear stress is known to defer the formation of a waxy gel by decreasing the gelation temperature.[71,76] However, the gel formed a higher shear rate can have higher storage modulus and an loss modulus, indicating a greater strength of the gel in this condition.[72] The paraffin distribution is perhaps the most complicated variable for gelation due to its poly-dispersity. It is known that an increase in the fraction of the same paraffin leads to an

increase in the gelation temperature.[76] However, an increase in the fraction of the lighter paraffins when the total paraffin fraction is maintained constant can greatly reduce the gelation temperature.[70] Furthermore, the existence of the branched and cyclic paraffins can significantly alter the structure and the crystallinity of the gel.[73,74] Consequently, a long-term practical future approach would be to develop a gelation model at quiescent conditions that can account for the effects of these parameters before one can extend the model of this phenomenon to flow conditions that include the complications from heat and mass transfer characteristics of a pipeline.

7.B Three dimensional CFD simulation of wax deposition in oil/water stratified flow

The correlations for heat and mass transfer that are well established in single-phase turn out to be unreliable for oil/water stratified flow.[60] Computational Fluid Dynamics (CFD) techniques, on the other hand, have been one of the most promising tools for multiphase flow modeling where the transport phenomena can be more fundamentally studied. The volume of fluid (VOF) method used in the CFD simulations has been proved to be an accurate and efficient approach to simulate flows of continuous immiscible phases.[77,78] However for oil/water stratified flow, significant computational intensity is required because a 3D simulation is needed in order to account for the vertical asymmetry of the flow. In addition, one needs to apply dynamic mesh techniques in order to account for the reduction in the effective pipe diameter due to wax build-up as time progresses. The connectivity of the dynamic mesh in 3D simulations has brought significant computational difficulties for mesh configurations, which further demands a higher computational intensity to overcome. As a preliminary investigation, a CFD model has

been applied to investigate the heat/mass transfer characteristics at t = 0 for oil/water stratified flow in order to determine the incipient mass flux from the oil to the wall

7.B.1 Geometry

The geometry for the CFD simulation is based on the the flow-loop apparatus used for the wax deposition experiments for stratified flow, as described in Chapter 6. It consists of two sections: the flow development section and the test section, as shown in Figure 7-3.

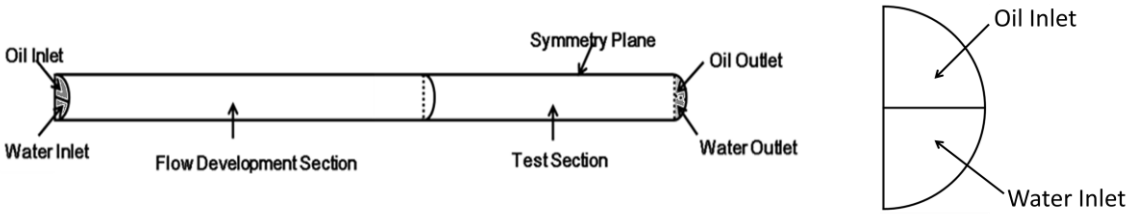

Figure 7-3: Schematic of the geometry for the CFD model

The inlet of the pipe was divided into two sections: the oil inlet (top) and the water inlet (bottom). The flow development section after inlet was used to insure a steady oil/water two-phase flow before the fluids enter the test section where cooling was applied. Because of the horizontal symmetry of the oil/water stratified flow, only half of the pipe is included in the CFD simulation in order to reduce computational intensity. The dimensions of the CFD model are the same as experiment configuration listed in Chapter 6 (Table 6-2).

7.B.2 Hydrodynamics

For the hydrodynamics analysis, the Volume of Fluid (VOF) method is applied for the multiphase flow. Because the minimum Reynolds numbers of the oil in the experiments is around 4500, the flows in the experiments are considered as turbulent flow

and thus the k-ε turbulent model is used. The model assumes that oil and water enter the inlet with the flow rate based on experimental conditions and no-slip conditions are applied at the wall.

7.B.3 Heat and Mass transfer

In this CFD model, wax is considered as a species only soluble in the oil phase. The inlet concentration of wax is assumed to be in thermodynamic equilibrium with the crude oil at the inlet temperature. In the flow developing section no cooling is applied to the oil and water. The heat loss from the oil and water to the surrounding room temperature in this section is negligible because the inlet temperatures of the fluids (20ºC) are close to room temperature and the external heat transfer coefficient of the air is sufficiently low to further prevent significant heat exchange. In the test section, the fluids are subject to convective cooling by the coolant water flowing through the annulus of the pipe. The coolant temperature was measured using the thermal couples installed in the flow loop The external heat transfer coefficient was calculated by the empirical correlation from Perry's Chemical Engineer's Handbook[79] based on the flow rate and the properties of the coolant. The concentrations of wax in oil at the wall are assumed to be in thermodynamic equilibrium with the oil at the temperature of the wall.

The solution process used a First-Order Upwind Discretization scheme[80] and the solver implemented the Least Square Cell Based algorithm for gradient calculations. The convergence criterion for steady simulation was set to 10^{-5}.

7.B.4 Mesh Optimization

Generally, a mesh that is too coarse decreases the accuracy of the solution profiles while a mesh is too fine with many cells greatly increases computational intensity and potentially leads to divergence in the calculations. Therefore, the mesh grid was gradually refined until the solution profile based on a model case was grid-independent. The mesh is refined in both radial and axial directions. The optimized mesh grid contains 80000 numerical cells in total.

7.B.5 Preliminary results and discussions

7.B.5.a Hydrodynamics: Comparison between model predictions and x-ray measurements

The water volume fraction profile predicted by the CFD simulation is compared with that measured by the X-ray at different vertical locations from bottom to the top of the pipe, as illustrated in Figure 7-4.

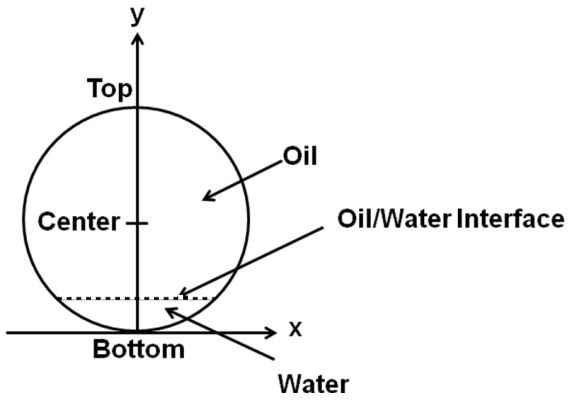

Figure 7-4: Labels for different vertical locations in the pipe

Figure 7-5 and 7-6 show the comparison between simulation results and experimental measurements. In Figure 7-5, the water cut was varied while the total flow rate, (Q_{oil} + Q_{water}), was held constant at 5 m^3/h.

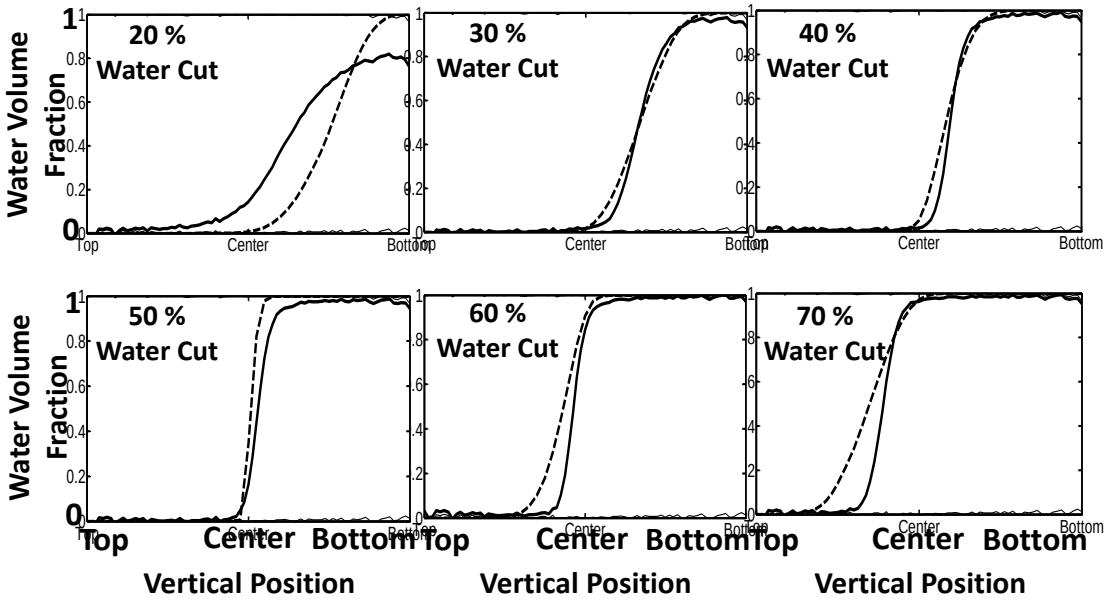

Figure 7-5: Comparison between simulation results and X-ray measurements for the water volume fraction for different water cuts with a total flow rate of 5m^3/h

Tthe X-ray measurements in shows that a completely stratified regime was observed for the case of total flow rate = 5 m^3/h and water cuts ranging from 30% to 60%, as can be seen by the fact that:

1) The water volume fraction is virtually 0% at the top part of the pipe.
2) The water volume fraction is virtually 100% at the bottom part of the pipe.
3) The transition in water volume fraction from 0% to 100% occurs in a thin layer, indicating there are very few oil/water droplets at the oil/water interface.

It is seen that for these complete stratified flows, the CFD model predicts the water volume fraction profile accurately for completely stratified flow regimes, because the VOF method is used primarily to characterize the hydrodynamics of two continuous phases.

Figure 7-6 shows the same type of profiles as Figure 7-5 but for a higher total volumetric flow rate (10 m^3/h).

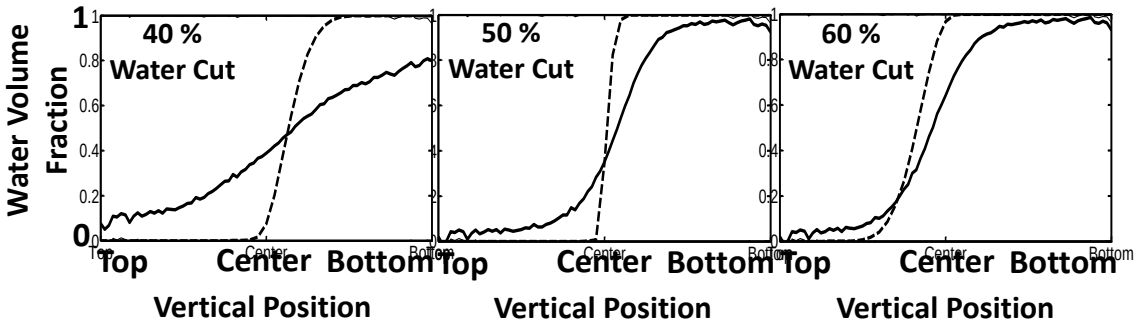

Figure 7-6: Comparison between simulation results and X-ray measurements for the water volume fraction for different water cuts with a total flow rate of 5m^3/h

It can be seen from the X-ray measurements that the oil and water droplets start to form for these flows as the water volume fraction is not exactly 0% at the top of the pipe and not 100% at the bottom, More importantly, the transition from the oil phase to the water phase occurs over a much wider vertical range in comparison to the stratified flows shown in Figure 7-5. These two findings indicates the formation of significant oil and water droplets for the total flow rate of 10m^3/h such that as least part of the water/oil flow is in the dispersed flow regime as previously shown in Figure 5-1. As expected, slight deviations can be observed between the CFD calculations and the X-ray measurements for these flows as the VOF method is most accurate when two fluids form completely stratified flows.

Consequently, the CFD model is used to investigate the heat and mass transfer characteristics for the deposition experiments with total flow rate of 5m^3/hr and water cuts with 0%, 25% and 50%, as listed in Table 6-4. The deposition experiment with single-phase oil flow at 5m^3/hr will be also included as a reference.

7.B.5.b Heat transfer calculations

Accurate heat transfer calculations are necessary in order to produce satisfactory calculations for mass transfer and deposition because mass transfer is dependent on the

solubility of wax, which is a function of the temperature. Therefore, it is necessary to verify the accuracy of the heat transfer calculations before the mass transfer calculations are performed.

Single-phase heat transfer

Before we investigate the accuracy of the heat transfer calculations in oil/water flow, an analysis was first performed on the single-phase oil flow in order to validate the CFD calculations. This validation was carried out by comparing the two sets of parameters:

Parameter 1): The outlet bulk temperature of the oil predicted by the CFD model $T_{\text{out, CFD}}$ and that measured by the experiment, $T_{\text{out, exp}}$.

Parameter 2): The heat loss of the fluid and the heat loss to the coolant obtained from the temperature difference between the inlet and the outlet as measured from the experiment, $(q_{\text{out, single}} - q_{\text{in, single}})_{\text{exp}}$, and heat loss to the coolant based on the wall temperature calculated from the CFD calculations, $q_{\text{single, coolant, CFD}}$. The value of $(q_{\text{out, single}} - q_{\text{in, single}})_{\text{exp}}$ is calculated from Equation (7.1) while $q_{\text{single, coolant, CFD}}$ is given by Equation(7.2).

$$(q_{\text{out,single}} - q_{\text{in,single}})_{\text{exp}} = \rho_{\text{o}} \cdot Q_{\text{o}} \cdot C_{\text{p,o}} \cdot (T_{\text{out,exp}} - T_{\text{in,exp}}) \tag{7.1}$$

$$q_{\text{single, coolant,CFD}} = \int_{\text{wall}} h \cdot (T_{\text{wall}} - T_{\text{coolant}}) \cdot dA_{\text{wall}} \tag{7.2}$$

Table 7-1 lists the comparisons of these two sets of parameters. One observes the excellent agreements of the outlet temperatures and the heat loss for the oil and water

between the experimental measurements and the CFD calculations, indicating that the CFD model has achieved great accuracy in modeling single-phase oil flow.

Table 7-1: Comparison of outlet temperature and heat loss of the oil between the experimental measurements and the CFD calculations.

$T_{out,\ exp}$, °C	$T_{out,\ CFD}$, °C	$(q_{out,sinlge} - q_{in,sinlge})_{exp}$, kJ/s	$q_{single,\ coolant,\ CFD}$, kJ/s
23.74	23.75	0.659	0.654

Multiphase heat transfer

For oil/water flow, the outlet in the experimental configuration was equally divided into two sections: the upper half outlet and the lower half outlet as shown in Figure 7-3. Table 7-2 shows the comparison of outlet temperatures between simulation results and experimental data.

Table 7-2: Comparison of outlet temperatures

Water cut, %	$T_{in,\ upper,\ exp}$ (oil inlet), °C	$T_{in,\ lower,\ exp}$ (water inlet), °C	$T_{out,\ upper,\ exp}$, °C	$T_{out,\ lower,\ exp}$, °C	$T_{out,\ upper,\ CFD}$, °C	$T_{out,\ lower,\ CFD}$, °C
25	24.0	23.1	23.44	23.23	23.26	23.25
50	24.0	21.6	23.04	21.70	22.03	22.03

It is seen that for the water cut of 25% both the upper half outlet temperature and the lower half outlet temperature can be accurately predicted. A slight deviation is observed for the case of 50% water cut where the temperature is slightly under-predicted for the upper half outlet and over-predicted at the lower half outlet. Because the inlet temperature for the oil is higher than that for the water, this slight deviation in the outlet temperatures indicates that the heat transfer from the oil phase to the water phase is slightly over-estimated. This over-estimation can be due to the formation of the water and oil droplets near the middle of the pipe that could decrease the degree of interfacial heat

transfer from the oil to the water in the experiments, while this factor is not accounted for in the CFD model.

7.B.5.c Mass transfer calculation

Because of the enormous computational intensity required for 3D simulations, the focus of the current CFD analysis is not to simulate a complete duration of a deposition experiment. However, significant insights can be still obtained by investigating the mass transfer characteristics of wax molecules at t = 0. The first parameter of interest is the radial mass flux at a particular position of the wall, $J_{wax,\ t=0,\ CFD}$, represents the rate of wax molecules that are transported from the oil towards the pipe wall to form a deposit, as shown in Equation (7.3).

$$J_{wax,\ t=0,\ CFD} = -D \cdot \frac{dC}{dr} \tag{7.3}$$

Because the wax thickness varies on the pipe circumference, one should integrate the local mass flux, $J_{wax,\ t=0,\ CFD}$ (kg/m^2/s) over the arc area that are covered by the wax deposit in order to find the total max flux towards the wall, $\dot{m}_{wax,\ t=0,\ CFD}$ (kg/s). The arc area that is covered by the deposit, $A_{deposit,\ exp}$ is obtained from the camera pictures of the deposit shown Figure 6-12 and is listed in Table 7-3

Table 7-3 Comparison of $A_{deposit,\ exp}$

Water Cut ,% (Q_{total} = 5m^3/h)	$A_{deposit,\ exp}$, m^2
25	0.66
50	0.55

Consequently the integration is given by Equation (7.4) where A is the surface area at the wall.

$$\dot{m}_{\text{wax, t=0, CFD}} = \int_{A_{\text{deposit, exp}}} J_{\text{wax}} \cdot dA \tag{7.4}$$

Given the calculated area of deposition, $A_{\text{deposit CFD}}$, the total mass flux, $\dot{m}_{\text{wax, t=0, CFD}}$ can be calculated from Equation (7.4). Furthermore, the final weight of the deposit, $W_{\text{deposit, CFD}}$ can be obtained based on the initial increase rate of the deposit mass, $\dot{m}_{\text{wax, t=0, CFD}}$ as well as the duration of the experiment, $t_{\text{experiment}}$, as shown in Equation (7.5)

$$W_{\text{deposit, CFD}} = \dot{m}_{\text{wax, t=0, CFD}} t_{\text{experiment}} \tag{7.5}$$

The values of $W_{\text{deposit, CFD}}$ is compared with the weight of the deposit measured after the experiments, $W_{\text{deposit, exp}}$, as shown in Table 7-4

Table 7-4: Comparison of, $W_{\text{deposit, CFD}}$ with $W_{\text{deposit, exp}}$ for different water cuts when the total flow rate is maintained at $5\text{m}^3/\text{h}$

Water Cut ,% (Q_{total} = $5\text{m}^3/\text{h}$)	$\int_{\text{area of deposition, exp}} dA$	Experiment, $t_{\text{experiment}}$ = 2.71 days (2.341×10^5seconds)	Simulation	
		$W_{\text{deposit, exp}}$, kg	$\dot{m}_{\text{wax, t=0, CFD}}$, 10^{-6} kg/s	$W_{\text{deposit, CFD}}$,kg
25	0.66	1.11	6.02	1.41
50	0.65	0.90	5.59	1.30

It is seen that $W_{\text{deposit, CFD}}$ and $\frac{W_{\text{deposit, CFD}}}{A_{\text{deposit, exp}}}$, are greater than $W_{\text{deposit, exp}}$ and $\frac{W_{\text{deposit, exp}}}{A_{\text{deposit, exp}}}$ respectively. However, from the thickness-time trajectory curves shown in common deposition studies[14,55,54] it is expected that the growth of the deposit will be significantly weakened rather quickly because of the reduction in the radial mass flux, which is caused by the increase in the interface temperature as the deposit builds-up. Consequently, in order to appropriately compare the weight of the deposit between the CFD predictions and the experimental results, future work should be to account for the reduction in the radial diffusion during the build-up of the deposit and to predict the increase rate of the weight of the deposit as a function of time. Furthermore, from the existing sing-phase experiments it is known that the deposition model based on diffusion can under-predict the deposit thickness if the formation of the wax deposit includes both gelation and diffusion. This finding can hopefully be validated for stratified oil/water flow after the CFD model based on diffusion becomes capable of predicting the build-up of the deposit.

In order to account for the insulation effect by the deposit that significantly decreases growth rate of the wax deposit as a time progresses, the CFD model needs to include the build-up of the wax deposit and thus the geometry of the simulation needs to change with time. Many CFD techniques apply dynamic mesh to achieve this goal. However, significant computational intensity is involved as the significant iterations needs to be carried out whenever the mesh is updated based on a newly formed geometry. The significant aspect ratio of the deposit is expected to greatly increase the computational intensity of the model. It is expected as the advancement in the parallel computing and

the availability of the high performance computing centers, this hurdle can be eventually overcome.

Bibliography

[1] Bern PA, Withers VR, Cairns JR. Wax deposition in crude oil pipelines. In: *Proceedings of European Offshore Petroleum Conference and Exhibition* October 21-24 London, 1980:571–578.

[2] Burger ED, Perkins TK, Striegler JH. Studies of wax deposition in the trans-Alaska pipeline. *J Petrol Technol*. 1981;33:1075–1086.

[3] Majeed A, Bringedal B, Overa S. Model calculates wax deposition for N. Sea Oils. *Oil Gas J*. 1990;88:63–69.

[4] Hamouda, AA, Davidsen S. An approach for simulation of paraffin deposition in pipelines as a function of flow characteristics with a reference to Teesside oil pipeline. In: *Proceedings of International Symposium on Oilfield Chemistry* Houston, 1995:459–470.

[5] Brown, TS, Niesen VG, Erickson DD. Measurement and prediction of the kinetics of paraffin deposition. In: *Proceedings of SPE Technical Conference and Exhibition* Houston, 1993:353–368.

[6] Ribeiro FS, Souza M, Paulo R, Braga SL. Obstruction of pipelines due to paraffin deposition during the flow of crude oils. *Int. J. Heat Mass Transfer.* 1997;40:4319–4328.

[7] Asperger A, Engewald W, Fabian G. Analytical characterization of natural waxes employing pyrolysis-gas chromatography-mass spectrometry. *J. Anal. Appl. Pyrolysis.* 1999;52:103–115.

[8] Gluyas JG, Underhill JR. United Kingdom oil and gas fields. *Geol. Soc.* 2003;20:327–333.

[9] Niesen VG. The real cost of subsea pigging. *E&P Magazine* 2002, April 9. p97 http://www.epmag.com/archives/features/3332.htm.

[10] Nguyen AD, Fogler HS, Sumaeth C. Fused chemical reactions. II. Encapsulation: application to remediation of paraffin plugged pipelines. *Ind. Eng. Chem. Res.* 2001;40:5058–5065.

[11] Matzain A, Apte MS, Zhang HQ, Volk M, Brill JP, Creek JL. Investigation of paraffin deposition during multiphase flow in pipelines and wellbores—part 1: experiments. *J. Energy Resour Technol Trans. ASME.* 2002;124:180–186.

[12] Hausen H., Darstellung W.¨Armeuberganges in Rohren durch verallgemeinerte Potenzbeziehungen, *VDI Z.*, **4**, 91 _1943.

[13] Seider EN, Tate CE. Heat Transfer and Pressure Drop of Liquids in Tubes, *Ind. Eng. Chem.*, **28**, 1429 _1936.

[14] Singh P, Venkatesan R, Fogler HS, Nagarajan NR. Formation and aging of incipient thin film wax-oil gels. *AIChE J.* 2000;46:1059–1074.

[15] Singh P., Fogler HS, Nagarajan N. Prediction of the wax content of the incipient wax-oil gel in a flowloop: an application of the controlled-stress rheometer, *J. Rheol.*, **43**, 1437 _1999..

[16] Lee HS. Computational and rheological study of wax deposition and gelation in subsea pipelines [Ph. D Thesis]. Dept. of Chemical Engineering, University of Michigan; 2008

[17] Venkatesan R, Fogler HS. Comments on analogies for correlated heat and mass transfer in turbulent flow. *AIChE J*. 2004;50:1623–1626.

[18] Venkatesan R. The deposition and rheology of organic gels [PhD Thesis]. Dept. of Chemical Engineering, University of Michigan, 2004.

[19] Lee HS, Singh P, Thomason WH, Fogler HS. Waxy oil gel breaking mechanisms: adhesive versus cohesive failure. *Energy and Fuels*. 2008;22:480-487.

[20] Fung G, Backhaus WP, McDaniel S, Erdogmus M. To pig or not to pig: the marlin experience with stuck pig. In: *Proceedings of Offshore Technology Conference*, Houston, USA, 2006

[21] Singh P, Fogler HS. Fused chemical reactions: the use of dispersion to delay reaction time in tubular reactors. *Ind Eng Chem Res*. 1998;37:2203-2207

[22] Nguyen AD, Fogler HS, Sumaeth C. Fused chemical reactions. 2. encapsulation: application to remediation of paraffin plugged pipelines. *Ind Eng Chem Res*. 2001;40:5058-5065

[23] Dittus FW, Boelter LMK., Heat transfer in automobile radiators of the tubular type. *Publications in Engineering*, 1930;2:443-461

[24] Geankoplis CJ. *Transport Process and Separation Process Principles*. 4th Edition, Prentice Hall, 2003

[25] Van Driest ER. On turbulent flow near a wall, *J. Aero. Sci*. 1956;23:1007-1011

[26] Wilkes JO. *Fluid Mechanics for chemical Engineers*. Prentice Hall 2006

[27] Tanehill JC, Anderson DA, and Pletcher RH. *Computational Fluid Mechanics and Heat Transfer*. Taylor and Francis, 1997

[28] Marchisio DL, Barresi AA, Garbero M. Nucleation, growth and agglomeration in barium sulfate turbulent precipitation. *AIChE J*. 2002;48:2039-2050

[29] Fogler HS. *Elements of chemical Reaction Engineering*, 4th Edition, Prentice Hall, 2006

[30] Armenante PM, Kirwan DJ, Mass transfer to microparticles in agítated systems. *Chem Eng Sci.* 1989;44:2781-2796

[31] Hayduk W, Minhas BS. Correlations for prediction of molecular diffusivities in liquids. *Can. J. Chem. Eng.* 1982;60:295-299

[32] Cussler EL, Hughes SE, Ward WJ, Aris R. Barrier membranes. *J. Memb. Sci.* 1988;38:161-174

[33] Hernandez OC. Investigation of single-phase paraffin deposition characteristics [Master Thesis] University of Tulsa, 2002

[34] Han S, Huang Z, Senra M, Hoffmann R, Fogler HS. Method to determine the wax solubility curve from centrifugation and high temperature gas chromatography measurements, *Energy & Fuels*. 2010;24:1753-1761

[35] Lund HJ. Investigation of paraffin deposition during single-phase liquid flow in pipelines [Master Thesis], University of Tulsa, 1998

[36] Roehner RM, Fletcher JV, Hanson FV, Comparative compositional study of crude oil solids from the trans-Alaska pipeline system using high-temperature gas chromatography. *Energy & Fuels*. 2002;16:211-217

[37] Coto B, Martos C, Pena JL, Espada JJ, Robustillo MD. A new method for the determination of wax precipitation from non-diluted crude oils by fractional precipitation. *Fuel.* 2008;87:2090-2094

[38] The university of tulsa paraffin deposition prediction in multiphase flow lines and wellbores joint industry project.: fluid characterization and property evaluation final report (February 1999)

[39] Martos C, Coto B, Espada JJ, Robustillo MD, Gomez S, Pena JL. Experimental determination and characterization of wax fractions precipitated as a function of temperature. *Energy & Fuels* 2008;22:708-714

[40] Chen J, Zhang J, Li H. Determining the wax content of crude oils by usingdifferential scanning calorimetry. *Thermochimica Acta.* 2004;410:23-26

[41] Kok M, Letoffe J, Claudy P, Martin D, Garcin M, Volle J. Comparison of wax appearance temperatures of crude oils by differential scanning calorimetry, thermomicroscopy and viscometry *Fuel* 1996:75:787-790

[42] Elsharkawy AM, As-Sahhaf TA, Fahim MA, Wax deposition from Middle East crudes *Fuel*. 2000;79:1047-55

[43] Coutinho JAP. Predictive UNIQUAC: A new model for the description of multiphase solid−liquid equilibria in complex hydrocarbon mixtures. *Ind. Eng. Chem. Res*. 1998;37:4870–4875

[44] Pedersen KS, Skovborg P. Wax precipitation from North Sea crude oils. 4. Thermodynamic modeling *Energy & Fuels*. 1991;5:924-932

[45] Roehner RM, Hanson FV. Determination of wax precipitation temperature and amount of precipitated slid wax versus temperature for crude oils using FT-IR spectroscopy. *Energy & Fuels.* 2001;15:756-763

[46] Hansen AB, Larsen E, Pedersen WB, Nielsen AB, Ronnigsen HP. Wax precipitation from North Sea crude oils. 3. Precipitation and dissolution of wax studied by differential scanning calorimetry. *Energy & Fuels.* 1991;5:914-923

[47] Dauphin C, Daridon JL, Coutinho JAP, Baylere P, Potin-Gautier M. Wax content measurements in partially frozen paraffinic systems *Fluid Phase Equilibria*. 1999;161:135–151

[48] Zuo JY, Zhang D. Wax formation from synthetic oil systems and reservoir fluids. *Energy & Fuels.* 2008;22:2390–2395

[49] Pauly J, Dauphin C, Daridon JL. Liquid-solid equilibria in a decane + multi-paraffins system. *Fluid Phase Equilibria.* 1998;149:191–207

[50] Jennings DW, Weispfennig K. Effects of shear and temperature on wax deposition: Coldfinger investigation with a Gulf of Mexico crude oil. *Energy & Fuels* 2005;19:1376-1386

[51] Paso K, Fogler HS. Bulk stabilization in wax deposition systems. *Energy & Fuels* 2004;18:1005-1013

[52] Creek JL, Lund HJ, Brill JP, Volk M. Wax deposition in single phase flow. *Fluid Phase Equilibria,* 1999;158:801-811

[53] Bidmus HO, Mehrotra, AK. Solids deposition during "cold flow" of wax-solvent mixtures in a flow-loop apparatus with heat transfer. *Energy & Fuels* 2009;23:3184-3194

[54] Hoffmann R, Amundsen L. Single-phase wax deposition experiments. *Energy & Fuels* 2010;24:1069–1080

[55] Huang Z, Lee, HS, Senra M, Fogler, HS. A fundamental model of wax deposition in subsea oil pipelines. *AIChE J.* 2011, early view available online http://onlinelibrary.wiley.com/doi/10.1002/aic.12517/abstract

[56] Monrad CC, Pelton JG. Heat transfer by convection in annular spaces. *AIChE J.-Transactions*. 1942;38:593-611

[57] Shi H, Cai J, Jepson WP, Oil-water two-phase flows in large diameter pipelines. *J. Energy Resour. Technol.* 2001;123:270-276

[58] Barnea D, Brauner N. Holdup of the liquid slug in two phase intermittent flow, *Int. J. Multiphase Flow*. 1985;11:43-49

[59] Ng TS, Lawrence CJ, Hewitt GF. Laminar stratified pipe flow, *Int. J. Multiphase Flow*. 2002;28:963-996

[60] Matzain A, Apte MS, Zhang HQ, Volk M, Brill JP, Creek JL. Investigation of paraffin deposition during multiphase flow in pipelines and wellbores - part 1: experiments, journal of energy resources technology, *ASME- Transactions*. 2002;124:180-186

[61] Kim D, Ghajar AJ, Dougherty RL, Ryali VK. Comparison of 20 two-phase heat transfer correlations with seven sets of experiment data, including flow pattern and tube inclination effects, *Heat Transfer Engineering* 1999;20:15-40

[62] Yu HS, Sparrow EM, Stratified Laminar Flow in Ducts of Arbitrary Shape, *AIChE J.* 1967;13:10-16

[63] Deen WM. *Analysis of Transport Phenomena*, Oxford University Press, New York, Oxford, 1998

[64] Labes-Carrier C, Rønningsen HP, Kolnes J, Leporcher E. Wax deposition in North Sea gas condensate and oil systems: Comparison between operational experience and model prediction. In: *Proceedings - SPE Annual Technical Conference and Exhibition*. Setember 29-October 2. San Antonio, TX 2002:2083-2094

[65] Padgett FW, Hefley DG, Henriksen A. Wax crystallization-a preliminary report *Ind. Eng. Chem.*1926;*18*:832-835

[66] Visintin RFG, Lapasin R, Vignati E, D'Antona P, Lockhart TP. Rheological behavior and structural interpretation of waxy crude oil gels. *Langmuir* 2005;21:6240–6249

[67] Abdallah DJ, Weiss RG. n-Alkanes gel n-alkanes (and many other organic liquids). *Langmuir* 2000;16:352-355

[68] Venkatesan R, Nagarajan NR, Paso K, Yi Y, Sastry AM, Fogler HS. The strength of paraffin gels formed under static and flow conditions. *Chemical Engineering Science* 2005;60:3587–3598

[69] Rønningsen HP, Bjorndal B. Wax precipitation from North Sea crude oils. 1. Crystallization and dissolution temperatures, and Newtonian and non-Newtonian flow properties. *Energy & Fuels* 1991;5:895-908

[70] Senra M, Scholand T, Maxey C, Fogler HS. Role of polydispersity and cocrystallization on the gelation of long-chained n-alkanes in solution *Energy & Fuels*, 2009;23:5947–5957

[71] Kane M, Djabourov M, Volle JL, Lechaire J, Frebourg PG. Morphology of paraffin crystals in waxy crude oils cooled in quiescent conditions and under flow *Fuels*, 2003;82:127-135

[72] Kane M, Djabourov M, Voile JL. Rheology and structure of waxy crude oils in quiescent and under shearing conditions. *Fuel*. 2004;83:1591-1605

[73] Wardhaugh TL, Boger VD. Flow characteristics of waxy crude oils. Application to pipeline design. *AIChE J.* 1991;37:871–885

[74] Rønningsen HP. Rheological behaviour of gelled, waxy North Sea crude oils. *J. of Petrol. Sci. and Eng.* 1992;7:177–213.

[75] Hoffmann R, Johnson GW. *Flow Measurement and Instrumentation* 2011 Article in Press

[76] Singh P, Fogler HS, Nagarajan N. Prediction of the wax content of the incipient wax-oil gel in a pipeline: An application of the controlled-stress rheometer. *J. Rheology*. 1999;43:1437-1459

[77] Elseth G, Kvandal HK, Melaaen MC. Measurement of velocity and phase fraction in stratified oil/water flow. In: *International Symposium on Multiphase Flow and Transport Phenomena, Antalya*, Turkey, 2000;206–210.

[78] Gao H, Gu H, Guo L. Numerical study on stratified oil–water two-phase turbulent flow in a horizontal tube. *Int J. Heat and Mass Transfer* 2003;46:749-754

[79] Green DW, Perry RH. *Perry's Chemical Engineers' Handbook*, McGraw-Hill, 2008, Section 5-9

[80] Versteeg HK, Malalasekera W. *An introduction to computational fluid dynamics: the finite volume method*. Prentice Hall 1995